

A FINAL REPORT:
GEOHERMAL RESOURCE ASSESSMENT OF
THE BASIN AND RANGE PROVINCE
IN WESTERN UTAH

by

Mason C. Edwards & David S. Chapman

University of Utah
Department of Geology & Geophysics
June 2013

Utah Geological Survey Award 120000

July 2011-June 2013

ABSTRACT

A geothermal resource assessment of the Basin and Range Province in western Utah was carried out to identify resource potential for future exploration and exploitation. This assessment includes the following: (1) a new map of background heat flow, generated from approximately 500 new and existing heat flow determinations, (2) surface ground temperature established continuously across the state, and (3) a comprehensive thermal conductivity database compiled with more than 2300 measurements on Utah rock. Finally, a two-dimensional finite difference code was written to integrate determined heat flow, surface temperature, and thermal conductivity to model temperatures at depth.

Two cross-sections of the resulting temperature fields are presented from different regions of the Basin and Range. The first, in Utah's Blackrock Desert, was located to assess the highest recorded background heat flow ($>130 \text{ mWm}^{-2}$) in the state. The second, along the axis of the Great Salt Lake, was placed in a broad swath of elevated heat flow ($>105 \text{ mWm}^{-2}$). Temperatures and heat content of the rock at depths commonly accessed by current drilling technology (3-5 km) were evaluated for each section. In Blackrock Desert, 150°C was encountered at depths generally greater than 3 km and the thermal potential of rock between 3 km and 4 km for exploitation ranged between 0.14 EJkm^{-3} and 0.49 EJkm^{-3} , with a mean value 0.31 EJkm^{-3} . In the Great Salt Lake Region, the depth to 150°C is less than 3 km across the basin and the calculated thermal potential, in

the 3 km to 4 km depth interval, is between 0.33 EJkm^{-3} and 0.40 EJkm^{-3} with a mean 0.37 EJkm^{-3} .

High heat flows reported in the Blackrock Desert are encouraging indicators of the region's geothermal potential; however, more complicated geology and the presence of young cooling volcanics and intrusives appears to be inflating heat flow determinations, ultimately exaggerating modeled estimates of regional scale temperatures through basin sediments. In the Great Salt Lake Region, the combination of elevated heat flow, low conductivity sediments, and depth to basement result in temperatures and thermal potential that flag the region as prospective and a priority for geothermal exploration.

TABLE OF CONTENTS

1.	ABSTRACT.....	ii
2.	LIST OF FIGURES.....	v
3.	LIST OF TABLES.....	vi
4.	ACKNOWLEDGMENTS.....	vii
5.	INTRODUCTION.....	1
6.	SURFACE TEMPERATURE.....	8
7.	THERMAL CONDUCTIVITY.....	19
8.	HEAT FLOW.....	28
9.	TEMPERATURE FIELDS.....	46
10.	SYNTHESIS.....	64
11.	CONCLUSIONS AND RECOMMENDATIONS.....	73
	Conclusions.....	73
	Recommendations.....	75
12.	APPENDIX A.....	78
13.	APPENDIX B.....	84
14.	APPENDIX C.....	105
15.	APPENDIX D.....	108
16.	REFERENCES.....	110

LIST OF FIGURES

Figure	Page
1. Project base map.....	3
2. Ground and air temperatures for central Utah.....	10
3. Distribution of weather stations used for surface temperature control.....	12
4. Differences between the observed and predicted SAT for weather stations in Utah.....	14
5. Distribution of differences between observed and predicted SAT.....	15
6. Spatial distribution of differences between observed and predicted SAT.....	16
7. Surface ground temperatures for the state of Utah.....	18
8. Typical thermal conductivity values of rocks.....	20
9. The divided bar configuration.....	22
10. Locations of wells with new thermal conductivity measurements.....	26
11. Thermal equilibration of the P-2A well.....	31
12. Comparison of three BHT correction methods.....	36
13. Distribution of heat flow data on the Colorado Plateau and Basin and Range....	38
14. Spatial correlability of heat flow sites across Utah.....	39
15. Heat flow for the state of Utah from convergent interpolation scheme.....	42
16. Heat flow for the state of Utah from ordinary kriging scheme.....	43
17. Normalized kriging variance for Utah heat flow.....	44

Figure	Page
18. Heat flow measurements in the state of Utah.....	45
19. Hydrogeologic unit groupings.....	48
20. Porosity trends in the GSL and BRD regions.....	51
21. Porosity trends in the GSL and BRD regions for encountered HGUs.....	53
22. Temperature cross-section in the GSL region.....	56
23. Temperature cross-section in the BRD region.....	58
24. Extent of geothermal resource identified in GSL and BRD regions.....	67
25. Model sensitivities.....	70
26. Differences between modeled and observed temperature.....	72
B1. Thermal conductivities from PA-1.....	85
B2. Thermal conductivities from P2-A.....	87
B3. Thermal conductivities from PA-3.....	89
B4. Thermal conductivities from PA-5A.....	91
B5. Thermal conductivities from PA-6.....	93
B6. Thermal conductivities from Gronning 1.....	95
B7. Thermal conductivities from Pavant Butte 1.....	97
B8. Thermal conductivities from Hole-in-Rock 1.....	99
B9. Thermal conductivities from State of Utah “E” 1.....	101
B10. Thermal conductivities from State of Utah “N” 1.....	103

LIST OF TABLES

Table	Page
1. New thermal conductivity measurements.....	27
2. Hydrogeologic unit descriptions.....	49
3. Stratigraphic control mismatch.....	61
A1. Existing thermal conductivity measurements of Utah rock.....	79
B1. Thermal conductivity measurements for PA-1.....	86
B2. Thermal conductivity measurements for P2-A.....	88
B3. Thermal conductivity measurements for PA-3.....	90
B4. Thermal conductivity measurements for PA-5A.....	92
B5. Thermal conductivity measurements for PA-6.....	94
B6. Thermal conductivity measurements for Gronning 1.....	96
B7. Thermal conductivity measurements for Pavant Butte 1.....	98
B8. Thermal conductivity measurements for Hole-in-Rock 1.....	100
B9. Thermal conductivity measurements for State of Utah “E” 1.....	102
B10. Thermal conductivity measurements for State of Utah “N” 1.....	104
C1. Heat flow values generated in this study.....	106

INTRODUCTION

Increased interest in the development of sustainable energy sources to augment or replace current US energy supply has led to renewed investment in geothermal investigations. A 2005 international panel and associated 2006 report [Tester et al., 2006] estimates that recoverable geothermal resource throughout the United States is between 1.2 TW and 12 TW, assuming 2% and 20% recovery efficiencies, respectively. The majority of this resource located at commercially drillable depths (3 km to 5 km) is found in the Basin and Range Province of the western US between the Southern Rocky Mountains and the Sierra Nevadas and has no visible surface expression. Favorable conditions exist where an area is tectonically active supplying a high basal heat flow, and where young sedimentary basins are filled with low conductivity sediments [Tester et al., 2006].

Utah's Great Basin is noted for its high surface heat flow coupled with low thermal-conductivity sedimentary basins. Because of these conditions, it is possible that geothermal grade temperatures exist at commercially drillable depths. Identifying these blind systems could provide great benefit to the State of Utah where currently most resources being exploited are surface expressed. Notable examples are Blundell Geothermal Plant near Milford, Utah, which generates 26 MW_e [Chiasson, 2004], and the Milgro greenhouses, which directly utilize blind geothermal resource to heat and cool 26

acres of productive greenhouses near Newcastle, in Utah's Escalante Desert [Allred, 2004].

Blind geothermal systems are those without surface expression. They exist where subsurface temperature is sufficiently high for commercial development at economic depth. Estimating subsurface temperature, to identify these systems, in turn requires knowledge of surface temperature, surface heat flow, and the thermal-conductivity of the geologic section. Surface temperature can be estimated from elevation and latitude. Thermal conductivity can be measured directly by sampling the stratigraphic section or estimated based on common values for dominant lithology in the stratigraphic column. Conductive heat flow in the Basin and Range varies locally between 60 mW/m^2 and 150 mW/m^2 , with a mean value 90 mW/m^2 and standard deviation of 10 mW/m^2 [Chapman et al., 1979]. While not yet widely exploited, blind resources have been described. For example, Clement [1981] delineates a 13 MW system confined to 10 km^2 .

The study area encompasses the Great Basin Province in western Utah. Specific examples of temperature at depth are presented for the Black Rock Desert, in Millard County—approximately 200 km south-southwest of Salt Lake City—as well as the Great Salt Lake region, which trends northwest-southeast primarily through Box Elder and Davis Counties and is immediately adjacent to Salt Lake City (Figure 1).

Previous heat flow research includes a number of localized studies and one regional assessment. Heat flow measurements in Utah were first carried out by Costain [1973]. Near surface thermal gradients were calculated from shallow wellbores and then combined with measured thermal-conductivities of the encountered formations.

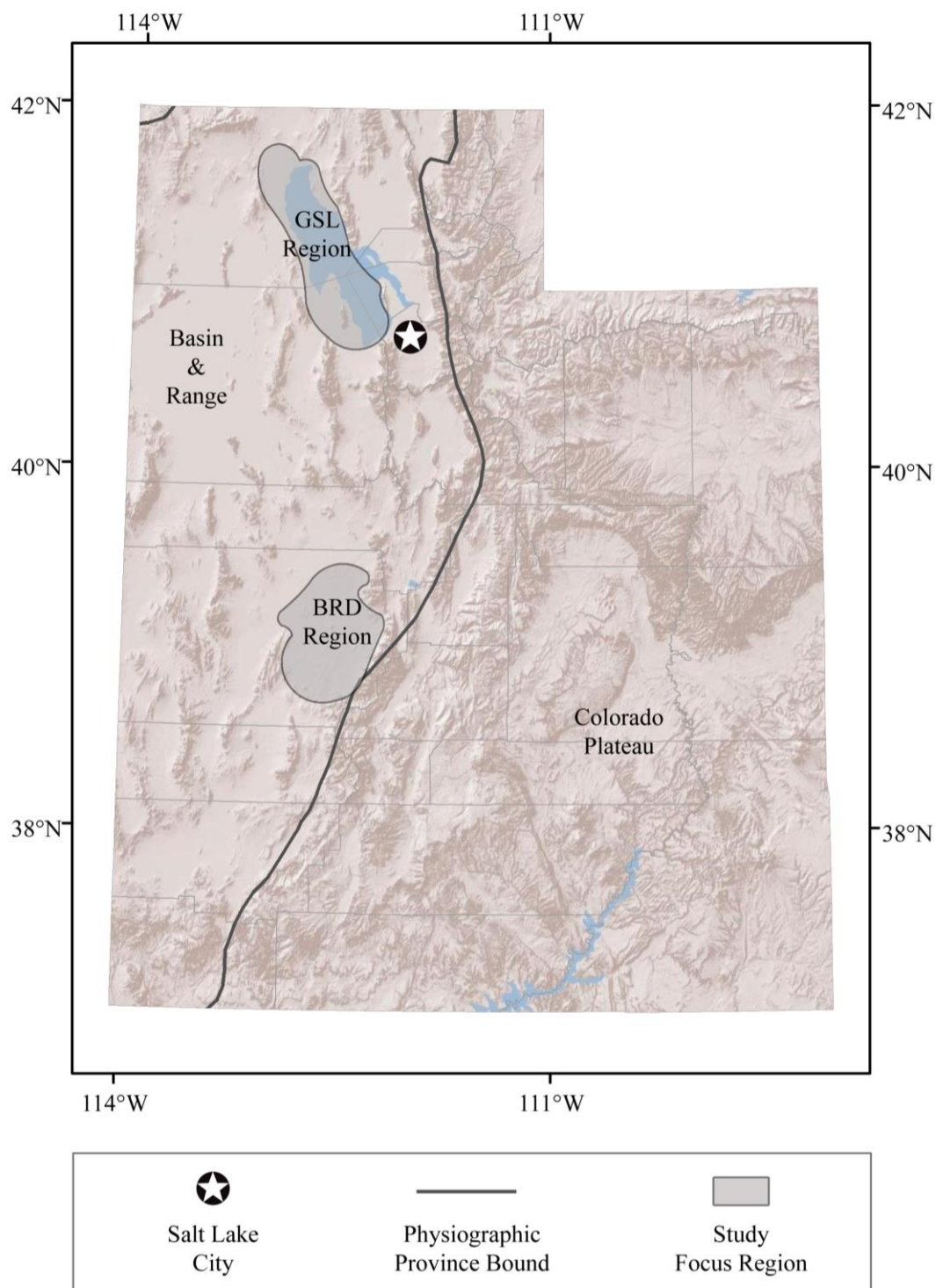


Figure 1. Project base map. Physiographic provinces, Basin and Range and Colorado Plateau, are separated by a thick line. Regions of particular interest, the Great Salt Lake (GSL) and Black Rock Desert (BRD), are in grey polygons. The location of Salt Lake City is included for context.

Subsequent studies of surface heat flow for select regions in western Utah's Great Basin have either utilized this "classic" method, being highly constrained but with limited vertical extents, or have made very broad regional characterizations. Other classic heat flow assessments throughout the state [Bauer, 1985; Bauer and Chapman, 1986; Bodell, 1981; Bodell and Chapman, 1982; Carrier, 1979; Carrier and Chapman, 1981; Chapman et al., 1981; Clement, 1981; Mase, 1979; Moran, 1991; Powell, 1997; Powell et al., 1988; Wilson, 1980] retain similar methodology. This classic heat flow approach well establishes thermal regimes for the near surface, but maintains inherent complications: First, classically derived heat flow generally evaluates only the upper 500 meters, a depth region susceptible to thermal disturbance from topography and groundwater flow. Second, while heat flow may be mapped locally and in considerable detail, the data are not laterally extensive. Choosing an appropriate interpolation method between these data rich, yet isolated regions is challenging.

In 2001, an extensive regional scale study of heat flow of the Colorado Plateau as well as the eastern Basin and Range in Utah was completed [Henrickson et al., 2001]. He supplemented classic heat flow work by determining surface heat flow from bottom-hole temperature (BHT) data in oil and gas wells. This work utilized the thermal resistance method first described by Bullard [1939] but later employed in Utah by Keho [1987]. Thermal gradients are estimated by correcting well log transient BHTs and thermal-conductivity is assigned where known or estimated from end member lithology of the stratigraphic section. Heat flow data based in this method are affected by BHT measurement or recording error. Heat flow determinations by this technique have the

advantage that many of these wells are drilled deep into sedimentary basins, thus minimizing shallow groundwater effects and all seasonal or climatic temperature signatures from the thermal gradient.

The major drawback to using BHT records is that temperature is not usually priority data collected during the drilling and well logging operations that provide this information. Extensive circulation of drilling muds in the wellbore annulus can significantly cool the formation. Due to safety concerns and the expense associated with maintaining an uncased or open hole, it is uncommon for re-equilibrated boreholes and hence undisturbed formation temperatures to be logged and measured. Previous studies exist that estimate undisturbed formation temperature [Lachenbruch and Brewer, 1959; Deming and Chapman, 1988; Cao et al., 1988] and generally require a minimum of two transient BHTs and the time since circulation ceased. Because log header data can be questionable, significant care must be taken when selecting BHT data to generate thermal gradients from these methods.

This study's primary objective is to produce subsurface temperature maps on a regional scale with the motivation of guiding future resource assessment in Utah's sedimentary basins. In analog to the oil and gas industry, where a resource characterization would not be performed in the absence of a petroleum system, this study deems the temperature field to be the most significant factor in a geothermal resource assessment. While other parameters commonly characterized for basin reservoir studies—porosity, permeability, and fluid content—are necessary to make up a productive reservoir, they are subordinate to resource in place. To arrive at subsurface temperature the study builds on previous works, including compiling all preceding

investigations, and then augments the resulting dataset with more recent gradient holes and additional BHT records. A more robust database of thermal conductivities specific to the Basin and Range has been generated, again compiling all previous measurements and including some 468 new values. In a broad sense, the main pursuit is to synthesize previous works, with generally limited extents, into a single cohesive dataset. From this dataset, a platform can be constructed to model a background conductive thermal regime aiding in the assessment of Utah's geothermal potential in this and future studies.

For a conductive regime, heat transfer is governed by Fourier's Law. In order to solve this numerically, boundary conditions—heat flow and surface temperature—must be determined and the thermal resistance through the domain must be provided. The greater study is broken into four tasks, three required to calculate the temperature field, and the calculation itself. The first is a determination of ground surface temperature which can be done analytically—provided the coefficients of the analytic expression, latitude and elevation, are calibrated to the study area. Inversion techniques are utilized on a dataset of 149 mean annual temperatures throughout the state of Utah and an expression for surface temperature is achieved. The second task is to establish the thermal resistance of units in the stratigraphic section. Previous work [Bauer, 1985; Bauer and Chapman, 1986; Bodell, 1981; Bodell and Chapman, 1982; Carrier, 1979; Carrier and Chapman, 1981; Chapman et al. 1981; Chapman et al., 1984; Clement, 1981; Moran, 1991; Powell, 1997; Powell et al., 1988; Wilson, 1980] provides some of the thermal conductivity data required, however additional sampling is carried out on cuttings and core from key wells to help characterize the Great Salt Lake and Blackrock Desert regions. The third task is constructing a surface heat flow map which integrates well

resolved, yet spatially isolated work from previous studies. Geostatistical techniques are employed to interpolate between heat flow measurements as well as quantify the uncertainty associated with interpolation in areas with little or no data for constraint. Finally, the temperature field is calculated analytically for a one dimensional case by rearranging Fourier's Law and incrementally calculating to depth through intervals with unique thermal resistances. This one dimensional case is then supplied as a seed for a two dimensional relaxation model, as described in Beardsmore [2001], and visualized in cross-section.

SURFACE TEMPERATURE

Our task is to map the mean annual ground temperature over the study area as the upper boundary condition for the subsurface temperature calculation. A robust dataset of surface air temperature (SAT) records exists from a variety of reliable sources that date back more than a century. Weather stations at municipal buildings, schools, and airports provide much of the data available for use in this study. However plentiful, this dataset is predominately measured at these discrete sites along major infrastructure. As a result, when surface temperature is required at remote locations or over a continuous domain, it is necessary either to extrapolate temperature from the nearest site or to estimate it based on physical and geographic controls.

Mean annual SAT within Utah is primarily dependent on two key factors: (1) solar radiation received annually, which is a function of latitude and (2) elevation through the adiabatic lapse. A lapse model, which considers temperature as a function of elevation and is well known from meteorology, was developed and described for central Utah in Moran [1991] as well as in Powell et al. [1988]. This lapse model demonstrated in Powell et al. relates temperature to elevation where temperature decreases with elevation at approximately $7^{\circ}\text{C}/\text{km}$. The Moran work employs this model to relate surface temperatures in a localized region with a high degree of topographic relief, demonstrating its reliability with respect to changes in elevation. The lateral extent of these studies is relatively small, less than 90 km and 2 km, as described in Powell and

Moran respectively. Because of their limited extents, neither study explored temperature change due to the effect of decreasing solar radiation with increasing latitude.

Additionally, two observations come out of the Powell and Moran work that allow us to make the transformation from SAT to surface ground temperature (SGT). The first is a systematic shift of approximately 3 °C between air and ground temperature. Ground temperatures are generally warmer than air temperatures for two reasons: (1) the ground can be thermally insulated by snow cover during the winter, holding the soil at a constant 0 °C while air temperatures fall below zero; (2) ground is heated directly by absorbing solar radiation, whereas the air is free to convect and mix, maintaining a lower temperature. Masbruch [2012] and Bartlett et al. [2004, 2005] demonstrate this decoupling between instantaneous ground and air temperatures in central Utah. Figure 2 illustrates the negative correlation between elevation and temperature as well as the static shift between SATs and surface ground temperatures (SGT) based on boreholes near weather stations on the Colorado Plateau in Central Utah. The second of the Powell and Moran observations that helps transform SAT to SGT is the influence on temperature due to the presence of vegetation. Vegetation affects SGT by as much as 2.5 °C depending on abundance and type [Moran, 1991] which provides a useful error threshold against which estimated SGTs can be assessed.

This study augments a typical SAT lapse equation—which conforms to the controls discussed above—and augments the equation to include an additional term for Universal Transverse Mercator (UTM) grid northing. The following analytic expression for SAT is produced:

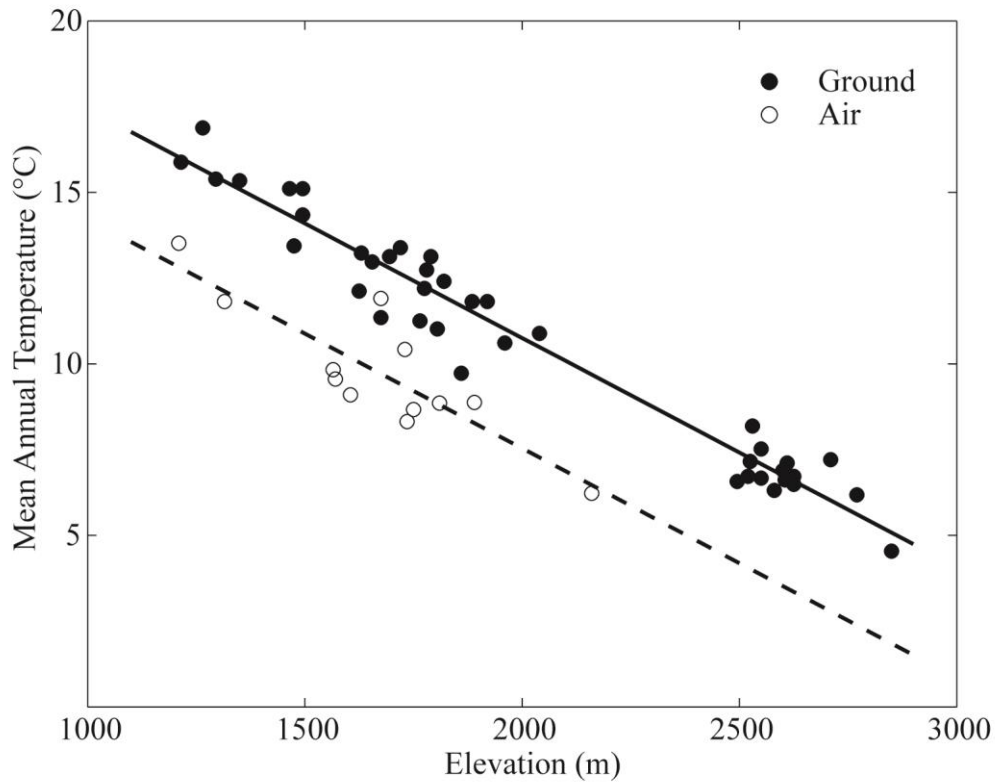


Figure 2. Ground and air temperatures for central Utah. Cross plotting mean annual ground temperatures from borehole temperature extrapolations (closed circles) and mean annual air temperatures from weather stations (open circles) against elevation reveals inversely correlated parallel trends between elevation and temperature with a 3 °C static offset between mean annual ground and mean annual air temperatures. Figure modified from Powell et al. [1988].

$$SAT(h, n) = C_1 h + C_2 n + C_3, \quad (1)$$

where h is the elevation in km, n is the UTM northing in km, and C_1 , C_2 , and C_3 are the calibrated coefficients. A shift of 3 °C to account for the difference between SAT and SGT can be applied after the coefficients are determined and residuals are assessed. Also, because there is no convenient method to predict the presence and type of vegetation, an error threshold of 2.5 °C is considered satisfactory for any results. Calibration of these model coefficients to the study area was achieved performing a linear least squares inversion on the forward problem of the generic form:

$$A(m) = d. \quad (2)$$

where m , are the coefficients C_1 , C_2 , and C_3 , A is the operator of the analytic expression, and d is the temperature associated with each elevation-northing pair.

The linear least squares method attempts to minimize the misfit between predicted data and observed data given a set of model parameters using variational calculus, which obeys the conditions of functionals in misfit space. A thorough derivation of the linear least squares method is provided in Zhdanov [2002], but the final solution to the linear least squares method takes the form:

$$m = (A^T A)^{-1} A^T d. \quad (3)$$

The inversion was supplied with temperature, elevation, and northing data from 149 weather stations throughout the state of Utah from the Western Regional Climate Center database (<http://www.wrcc.dri.edu>). Station locations are mapped in Figure 3. Mean annual temperatures were averaged for each site's history, including only data that

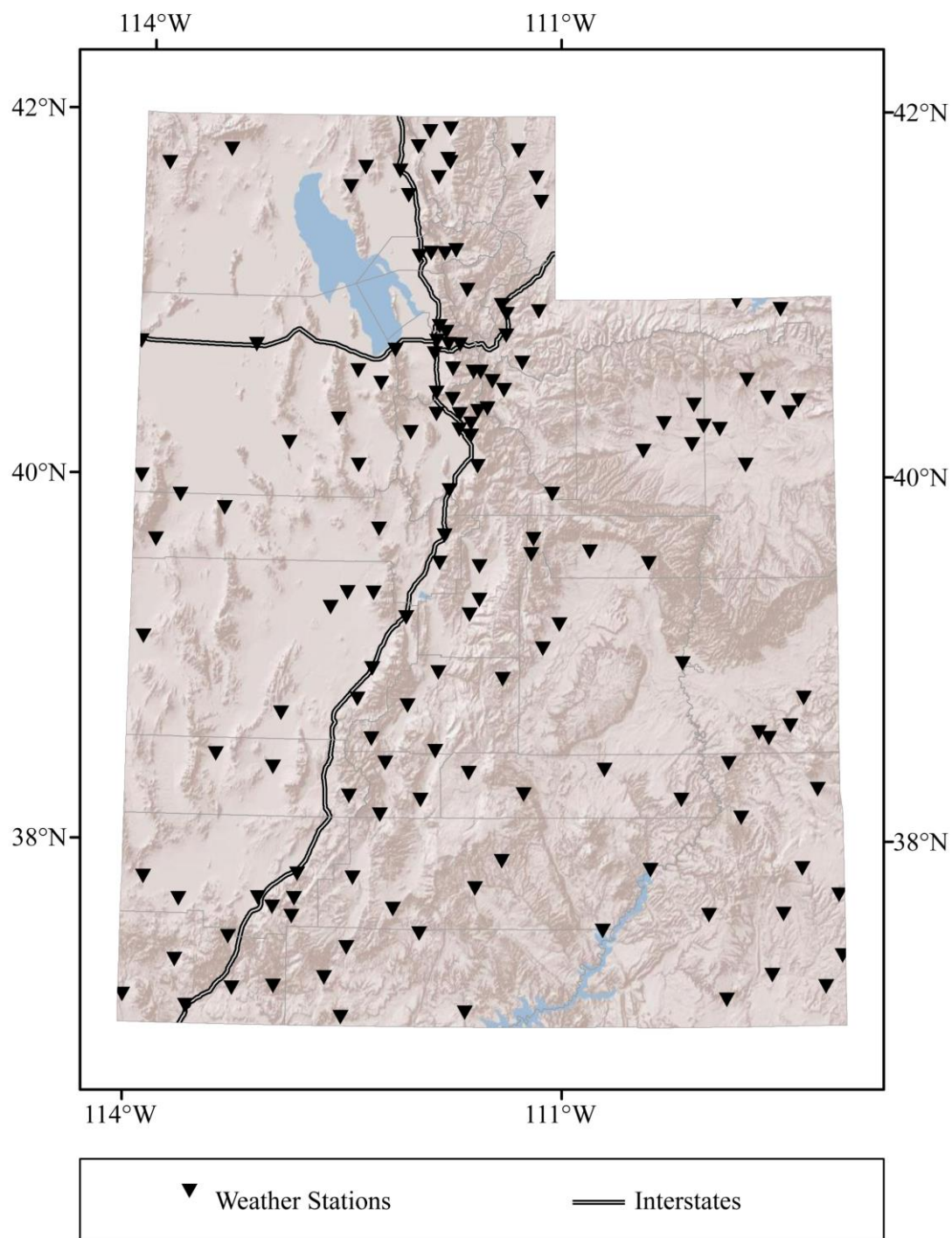


Figure 3. Distribution of weather stations used for surface temperature control.

were recorded during the previous two decades and contained at least ten years of records. Older sites with sporadic or incomplete records were removed. Coverage is well distributed with slightly higher density around population centers.

The inversion results produced values of $-6.42\text{ }^{\circ}\text{C}/\text{km}$ for the change with elevation (C_1), $-.0084\text{ }^{\circ}\text{C}/\text{km}$ for the change with latitude (C_2), and $56\text{ }^{\circ}\text{C}$ for the free parameter (C_3) that serves as a baseline from which variations are added or subtracted. The elevation lapse rate is close to the value reported in Powell et al. [1988] of $-6.7\text{ }^{\circ}\text{C}/\text{km}$. The temperature change with northing corresponds to a total difference of about $4\text{ }^{\circ}\text{C}$ between the north and south of Utah.

The inversion results were checked by calculating residuals between observed temperatures and predicted temperatures, and assessing the residuals in three ways. First, calculated residuals were plotted against station numbers to look for any major discrepancies as shown in Figure 4. Four residuals narrowly fall outside the $2.5\text{ }^{\circ}\text{C}$ margin attributed to vegetation and microclimate, and none outside $3\text{ }^{\circ}\text{C}$. Second, the univariate statistics show that the residuals were normally distributed with a mean at $0\text{ }^{\circ}\text{C}$ and standard deviation $1.2\text{ }^{\circ}\text{C}$. The distribution of differences is shown in Figure 5. Third, residuals for each station were mapped to highlight any location bias as shown in Figure 6. The Uinta Basin in northeast Utah has predicted temperatures warmer than those observed. Conversely the populated Wasatch Front southeast of the Great Salt Lake has predicted temperatures cooler than those observed. The absolute value of these residuals is less than the possible impact of vegetation and microclimates, the clustering around Salt Lake City and in the Uinta Basin has been attributed to microclimates. Beyond these regions, there are no apparent spatial trends observed in the residuals that warrant further

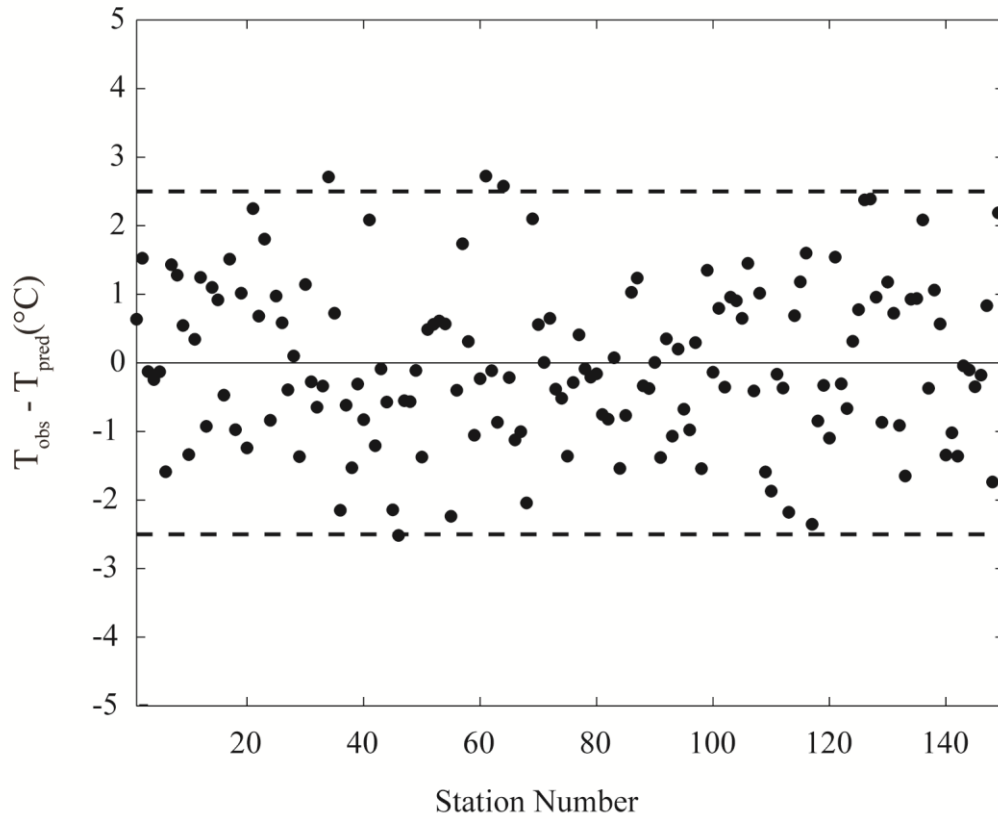


Figure 4. Differences between the observed and predicted SAT for weather stations in Utah. All residuals between observed and predicted mean annual SAT at weather stations are plotted as black dots. Bold dashed lines mark the potential effect of vegetation and microclimates ($\pm 2.5^{\circ}\text{C}$); all points within these bounds represent excellent matching between measured data and the inversion results.

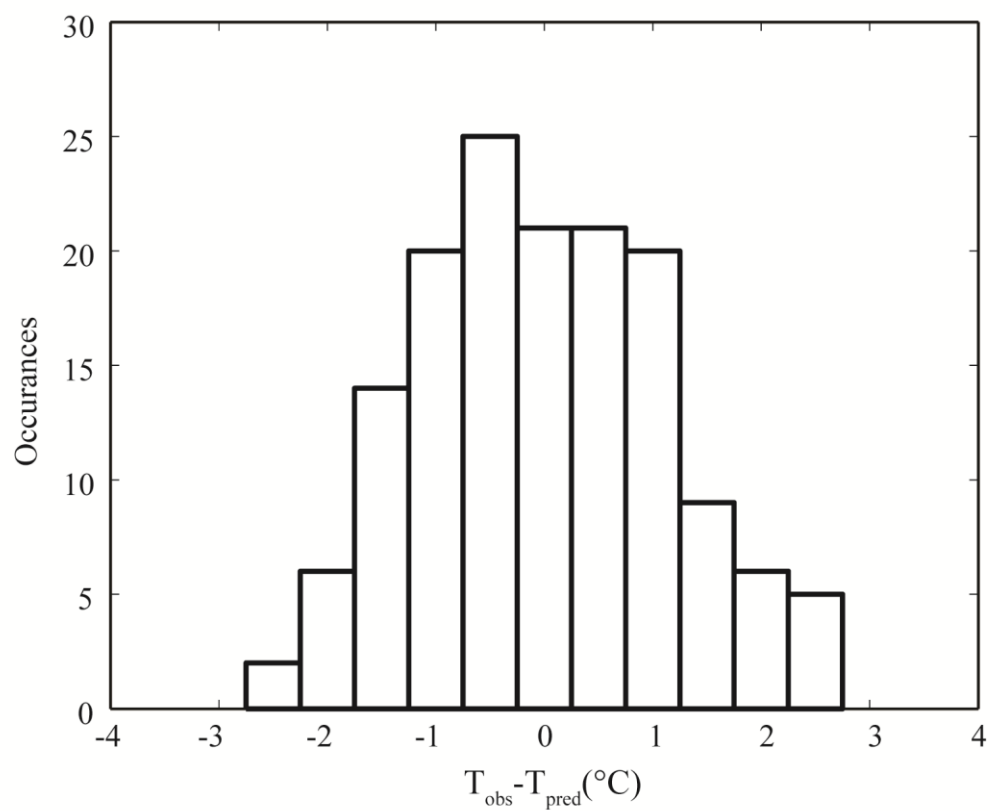


Figure 5. Distribution of differences between observed and predicted SAT. The residuals are normally distributed and the mean is centered about 0 °C.

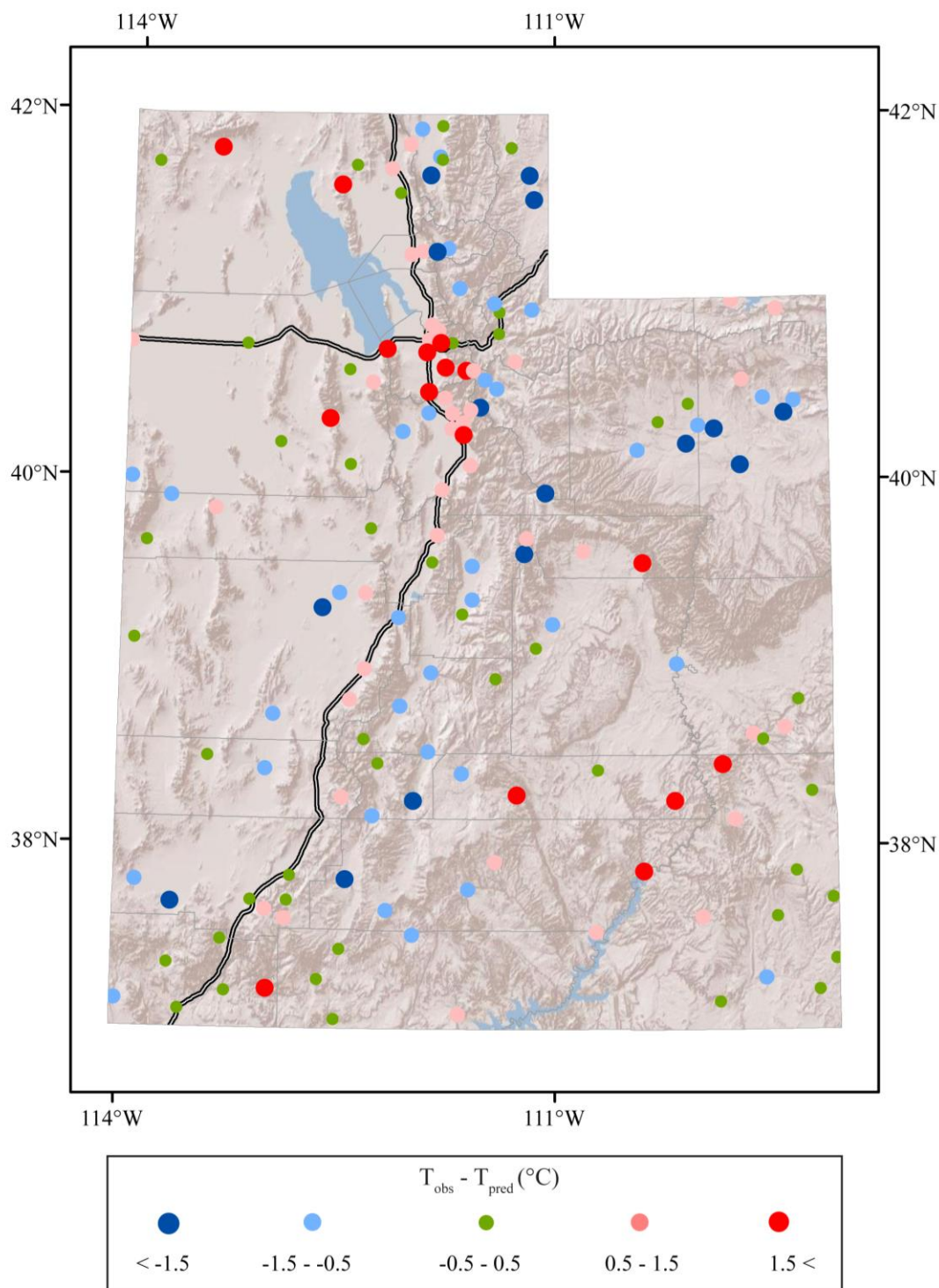


Figure 6. Spatial distribution of differences between observed and predicted SAT. Mean annual temperature residuals at weather stations throughout the state of Utah. Point size corresponds to absolute residual value with warmer colors being positive and cooler colors negative.

investigation, and even these regions fall within the expected scatter for residual temperatures.

Finally, temperature was calculated over the state of Utah using digital elevation models as the input to the calibrated temperature expression. Calculations were made at each grid cell center based on its elevation and northing coordinate, producing a map of surface temperature resolved to 90 meters. A static shift of +3 °C was added to the resulting map to account for the difference between ground and air temperature as observed in Figure 2. The resulting SGT (Figure 7) ranges from 0.3 °C to 21.4 °C through the state with a mean SGT of 11.9 ± 2.3 °C. The highest temperatures, 21 °C, are seen in the low elevations in southwestern Utah's Basin and Range while the lowest temperatures, 1 °C, are found above 2500 m in the Uinta Mountains in the northeast.

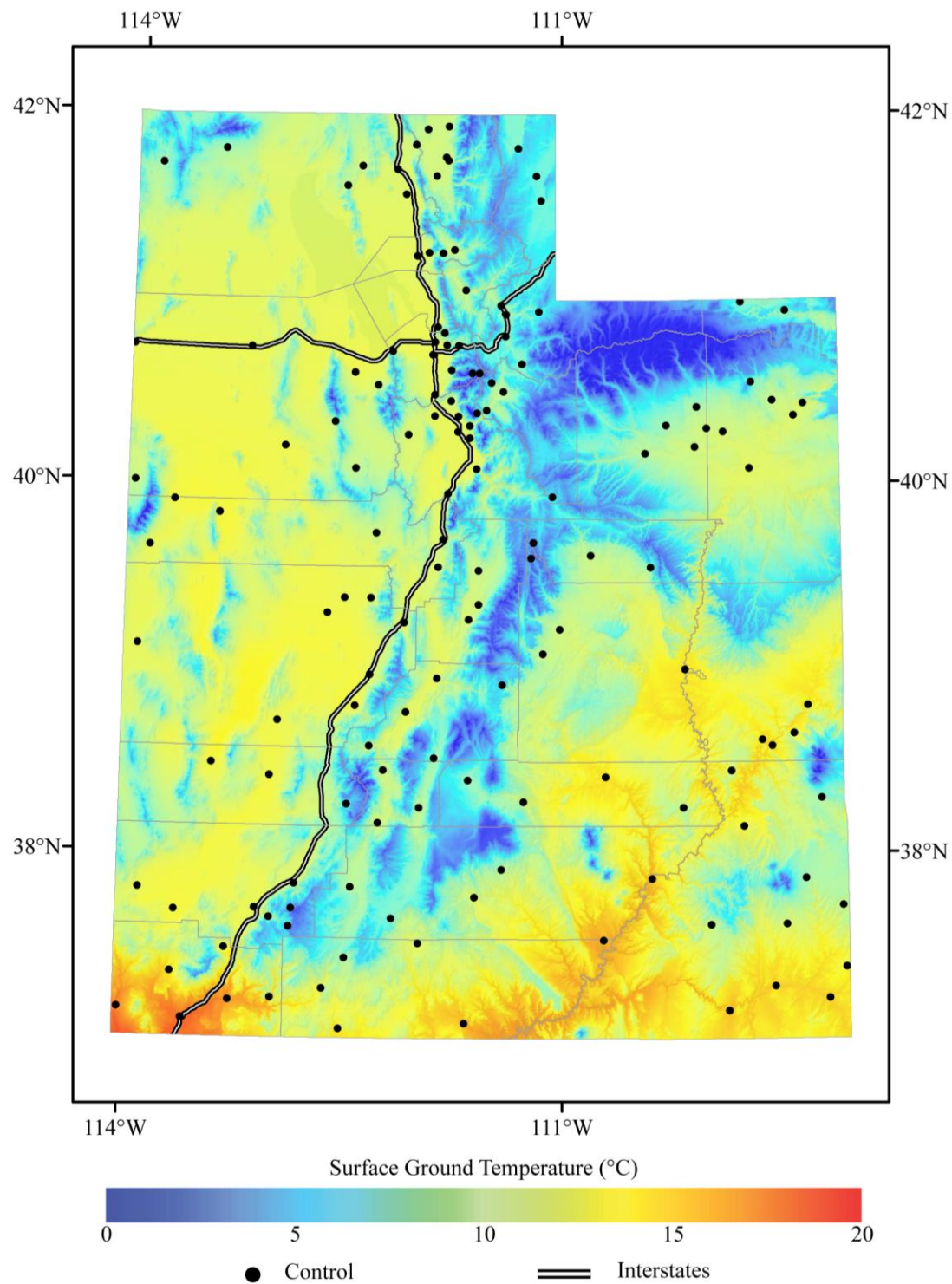


Figure 7. Surface ground temperatures for the state of Utah.

THERMAL CONDUCTIVITY

The calculation of temperature at depth requires an understanding of thermal resistance, the quotient of thickness and thermal conductivity through the stratigraphic section. Fundamental to constructing a thermal resistance profile of the subsurface is the ability to define the conductivity of a given formation. Thermal conductivity can be deduced by measuring rocks of the formations directly or by estimating a value based on a formation's dominant lithology.

Thermal conductivity's primary control is bulk composition consisting of both the matrix mineralogy and pore space. The range of matrix conductivity for common rocks and minerals is well established and observed variations range by more than a factor of eight [Barker, 1996; Beach et al., 1987; Beardsmore, 1996; Drury, 1986; Majorowicz and Jessop, 1981; Raznjevic, 1976; Reiter and Jessop, 1985; Reiter and Tovar, 1982; Roy et al., 1981; Taylor et al., 1986; Touloukin et al., 1970]. A single rock type, particularly sedimentary rocks, can vary by as much as a factor of three, though such large variations are not generally observed within a single formation. Figure 8 shows a compilation of thermal conductivity ranges for common rocks determined from the above sources. Due to the extent to which conductivity values can vary, more precise calculations of temperature at depth can be made by measuring the conductivity specific to the stratigraphic column. This study compiles all available conductivity measurements specific to Utah geology and supplements this thermal conductivity database with new

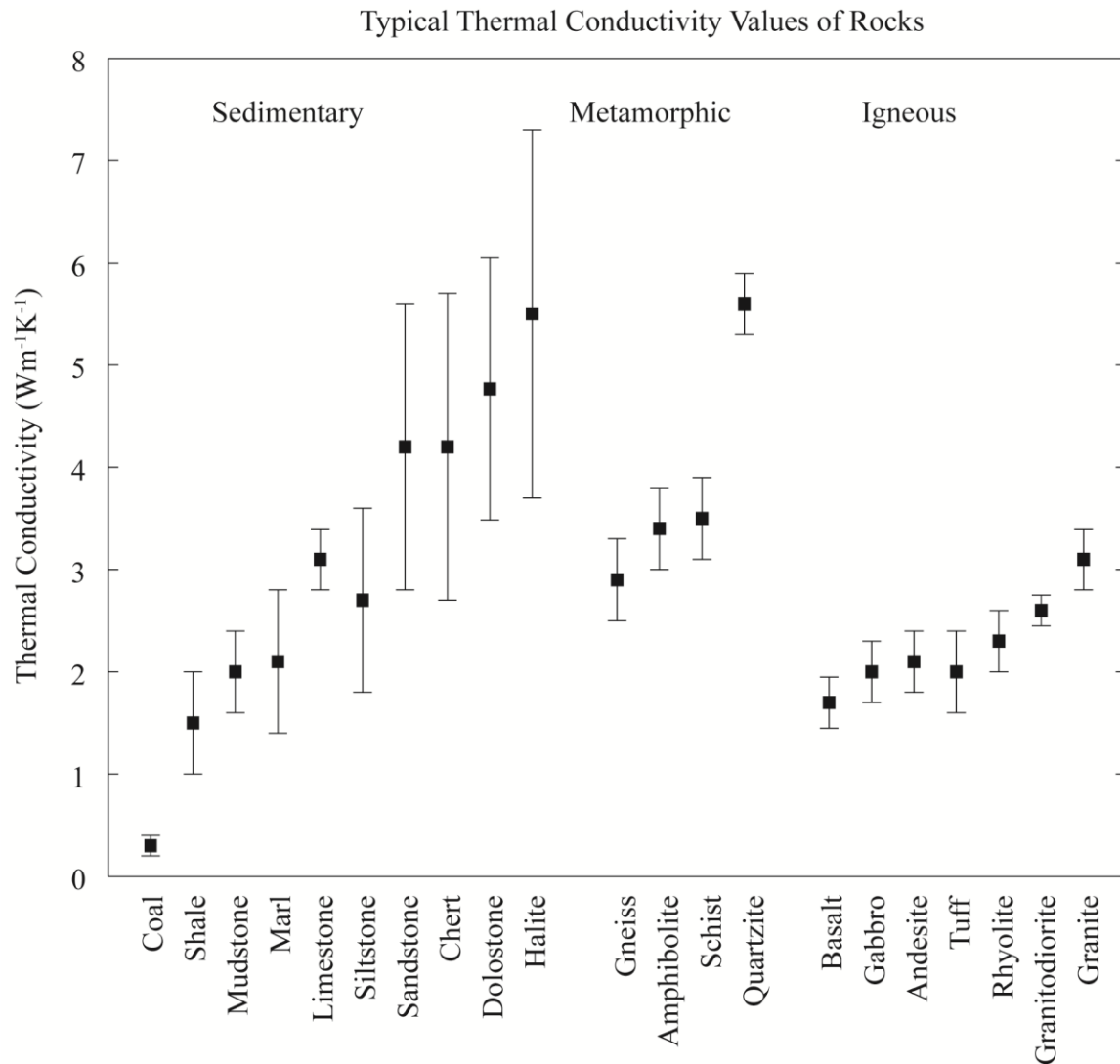


Figure 8. Typical thermal conductivity values of rocks. Range of matrix thermal conductivities observed in common lithologies organized by major rock group and sorted by ascending thermal conductivity. Squares show the mean conductivity and bars indicate one standard deviation. Crystalline rocks show limited variation, while sedimentary rocks vary greatly. Data compiled from Beardsmore and Cull [2001].

measurements of Basin and Range rocks. Previous studies on rocks found in Utah have collected over 1900 samples and measured thermal conductivity in approximately 60 formations in the Basin and Range and Colorado Plateau [Bodell and Chapman, 1982; Chapman et al., 1984; Deming and Chapman, 1988; Henrickson, 2000; Moran, 1991; Powell, 1997]. A complete tabular summary presenting statistics for existing measurements is given in Appendix A.

Thermal conductivity can be measured by either transient or steady state methods. The line-source method is the most common transient technique and involves putting a sample in contact with a heating element. Temperature is measured while constant heat is supplied and a plot of temperature increase against the log of time is generated. The slope of the best fit line is then the thermal conductivity of the sample. This technique is employed in full-space as well as half space methods and is most appropriate when measuring large samples. A common steady state technique is the divided bar method [Sass et al., 1971]. The majority of previous measurements on Utah rock as well as those measured for this study were made by the divided bar technique and a discussion of the method follows.

The setup for measuring conductivity by the divided bar method is shown schematically in Figure 9 and outlined in Sass et al. [1971], Chapman [1976], Bodell [1981] with later updates by Pribnow et al. [1995]. This method compares the one dimensional steady state temperature gradient across a sample of rock, which may be a rock core or a cell containing water and rock chips, to the gradient across a reference disk with known conductivity. Temperature differences through the stack are measured at four

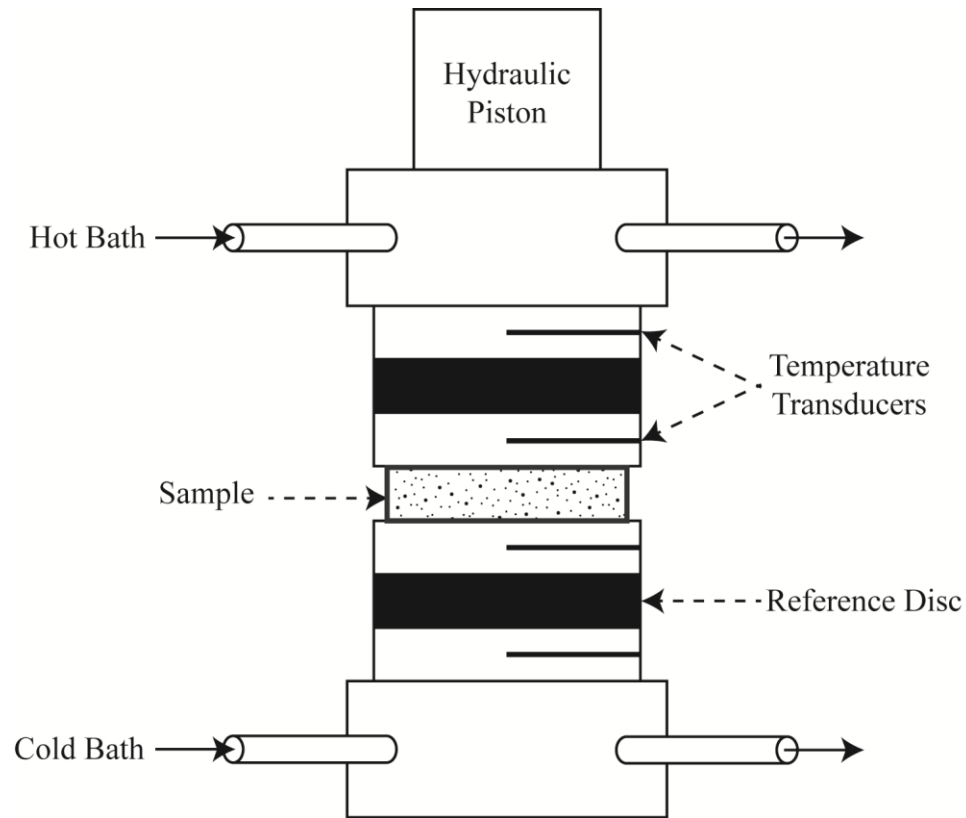


Figure 9. The divided bar configuration. Temperature at the top and base of the divided bar are maintained at fixed temperatures by flowing water from controlled temperature baths. Thermocouples placed in conductive material measure the thermal emf across the reference discs as well as the sample. A piston applies downward pressure holding all surfaces in contact, reducing the thermal contact resistance.

locations bracketing two reference discs and the sample. Assuming that no heat is lost from the system laterally, the heat flow through the sample and reference can be equated:

$$q_{ref} = k_{ref} * \nabla T_{ref}; \quad q_{sample} = k_{sample} * \nabla T_{sample}, \quad (4)$$

$$k_{ref} * \nabla T_{ref} = k_{sample} * \nabla T_{sample}, \quad (5)$$

$$k_{sample} = \frac{k_{ref} * \nabla T_{ref}}{\nabla T_{sample}}, \quad (6)$$

where k_{ref} is the conductivity of the reference, and ∇T_{ref} and ∇T_{sample} are the gradients across the reference and sample respectively. The gradients and conductivity of the references are known, thus the conductivity of the sample can be calculated. The surface area of the sample may not be the same as the surface area of the divided bar where the two are in contact. A correction for the difference in dimensions must be made:

$$k_{diam} = \frac{d_{bar}^2}{d_{outer}^2} * k_{sample}, \quad (7)$$

where d_{bar}^2 and d_{outer}^2 are the diameters of the divided bar and sample respectively. For core samples, k_{diam} is the final diameter corrected whole rock thermal conductivity.

Generally, the availability of drill cuttings is much greater than that of whole rock cores. Because drill cuttings must be contained to measure on the divided bar, they are packed as rock chips into water saturated cells. When measuring cells containing rock chips and water, k_{diam} includes the bulk contents of the cell as well as the cell itself. Additional corrections are required, beyond those applied to core samples, which account for the conductivity of the cell walls:

$$k_{bulk} = k_{diam} - \frac{d_{outer}^2 - d_{inner}^2}{d_{inner}^2} * k_{wall}, \quad (8)$$

which yields the bulk conductivity of the rock chip and water mixture in terms of d_{outer} and d_{inner} , the diameters of the outer and inner cell walls and k_{wall} , the conductivity of the wall material. Finally, the rock chip conductivity can be determined from a volumetric mixing expression with two constituents, rock chips (k_{matrix}), water (k_{water}), and the cell's total pore space (Φ):

$$k_{bulk} = k_{matrix}^{(1-\Phi)} * k_{water}^{\Phi}, \quad (9)$$

which rearranges to:

$$k_{matrix} = k_{water} * \left(\frac{k_{bulk}}{k_{water}} \right)^{\frac{1}{1-\Phi}}. \quad (10)$$

The conductivity of water, k_{water} , is known to be $0.6 \text{ Wm}^{-1}\text{K}^{-1}$ at standard conditions, and so equation (10) provides the thermal conductivity of the rock matrix.

New divided bar conductivity measurements were made on 468 cutting samples from five shallow gradient wells and five deep oil & gas exploration wells. The five gradient holes (PA-1, P-2A, PA-3, PA-5A, and PA-6) are part of a Utah Geological Survey drilling program and are all located in the Black Rock Desert (BRD) in Millard County, Utah. These wells were selected to characterize the thermal conductivity of shallow lakebed sediments found widely throughout the Basin and Range. Five exploration wells were selected to sample the deeper stratigraphic section of the BRD and Great Salt Lake (GSL) regions. Three wells—Gronning 1 (API: 02710423), Pavant Butte 1 (API: 02730027), and Hole-in-Rock 1 (API: 02730019)—are located in BRD and two

wells—State of Utah “E” 1 (API: 01130002) and State of Utah “N” 1 (API: 04530010)—are in the GSL region. Figure 10 illustrates the locations of the ten wells.

The shallow gradient holes encountered hydrated clays and basalt. Approximate whole rock conductivities measured on 197 clay samples varied from $1.01 \text{ Wm}^{-1}\text{K}^{-1}$ to $1.67 \text{ Wm}^{-1}\text{K}^{-1}$ with a mean of $1.30 \text{ Wm}^{-1}\text{K}^{-1}$ and standard deviation $0.15 \text{ Wm}^{-1}\text{K}^{-1}$. Basalts varied between $1.94 \text{ Wm}^{-1}\text{K}^{-1}$ and $2.89 \text{ Wm}^{-1}\text{K}^{-1}$ with a mean $2.26 \text{ Wm}^{-1}\text{K}^{-1}$ and standard deviation $0.29 \text{ Wm}^{-1}\text{K}^{-1}$ for the 9 samples measured.

Conductivity measured in the deep wells varies between $1.8 \text{ Wm}^{-1}\text{K}^{-1}$ and $8.7 \text{ Wm}^{-1}\text{K}^{-1}$. The large range observed reflects the variable composition of the stratigraphic section of interest and demonstrates the significance of characterizing its conductivity. The two wells in GSL encountered Quaternary and Tertiary basin sediments, upper Paleozoic carbonates and Paleozoic metamorphosed basement, most likely the Tintic Quartzite. Measured values of conductivity are $3.32 \pm 0.62 \text{ Wm}^{-1}\text{K}^{-1}$, $3.39 \pm 0.50 \text{ Wm}^{-1}\text{K}^{-1}$, $3.37 \pm 0.36 \text{ Wm}^{-1}\text{K}^{-1}$, and $6.36 \pm 1.54 \text{ Wm}^{-1}\text{K}^{-1}$ for each respectively. The three wells in BRD logged mostly Tertiary basin sediment (mudstones, salt, and sandstone) and basalts which unconformably overlay Paleozoic carbonates and metamorphosed Paleozoic basement, most likely Prospect Mountain Quartzite, as observed by penetrations at Hole-in-the-Rock 1 and Pavant Butte 1. Conductivities measured through the stratigraphic section are $3.42 \pm 0.87 \text{ Wm}^{-1}\text{K}^{-1}$ for the Quaternary section, $2.98 \pm 0.58 \text{ Wm}^{-1}\text{K}^{-1}$ for the Tertiary basin fill, $4.84 \pm 1.43 \text{ Wm}^{-1}\text{K}^{-1}$ in the Paleozoic carbonates, and $4.82 \pm 0.73 \text{ Wm}^{-1}\text{K}^{-1}$ in the Prospect Mountain Quartzite. Table 1 summarizes the measured values by rock unit.

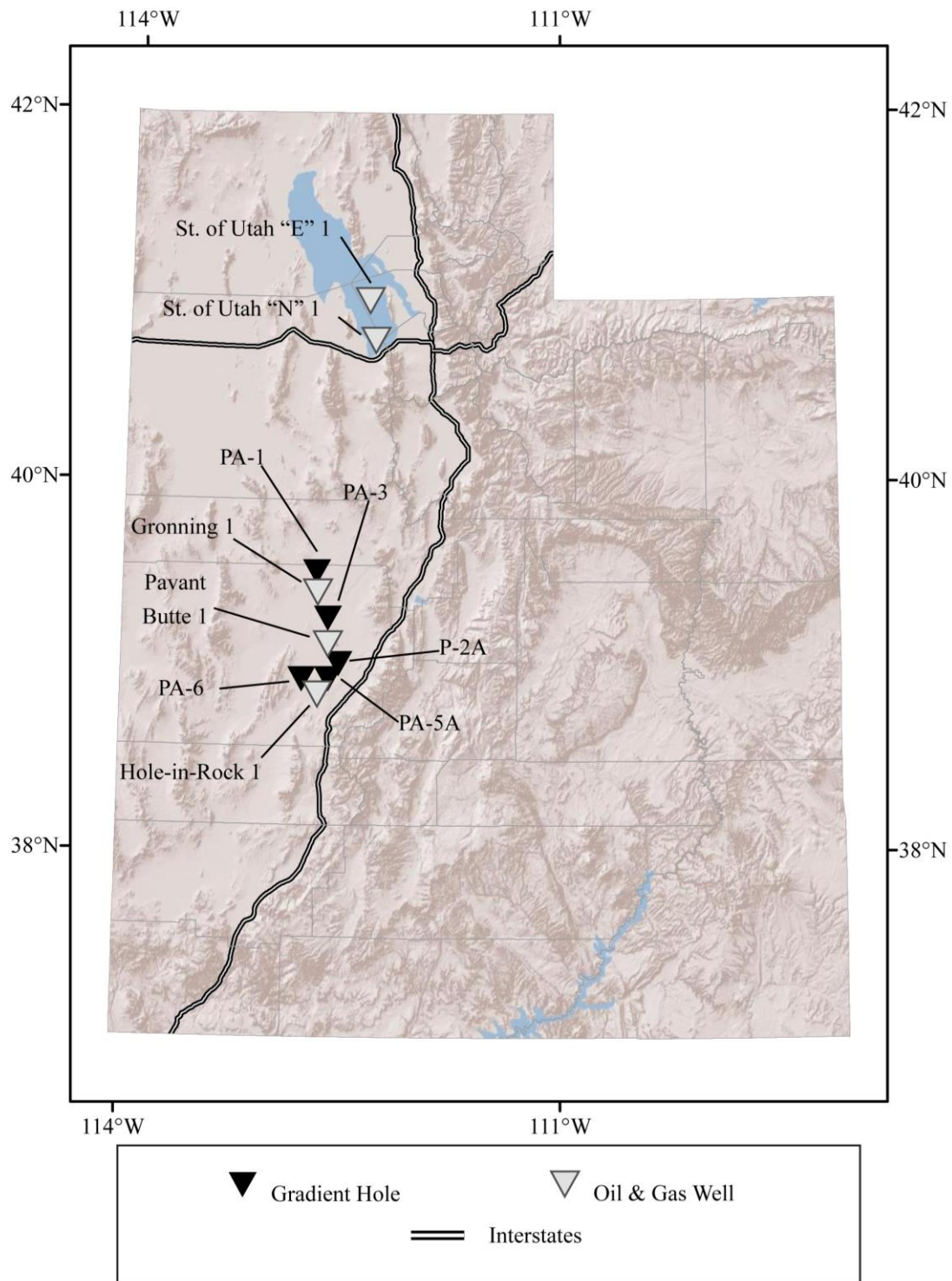


Figure 10. Locations of wells with new thermal conductivity measurements. White triangles indicate samples were taken from exploration wells and black triangles indicate samples were from shallow gradient holes.

Table 1. New thermal conductivity measurements*

Rock Unit	Thermal Conductivity (Wm ⁻¹ K ⁻¹)	Standard Deviation (Wm ⁻¹ K ⁻¹)	n Samples
Quaternary lakebed sediments ¹	1.30	0.15	197
Quaternary basalts ²	2.26	0.29	9
BRD Quaternary valley fill ²	3.42	0.87	24
GSL Quaternary valley fill ²	3.32	0.62	40
BRD Tertiary valley fill ²	2.98	0.58	123
GSL Tertiary valley fill ²	3.39	0.50	10
BRD Paleozoic carbonates ²	4.84	1.43	15
GSL Paleozoic carbonates ²	3.37	0.36	8
Tintic Quartzite ²	6.36	1.54	38
Prospect Mountain Quartzite ²	4.82	0.73	3

* Conductivities measured on the divided bar.

¹Whole rock conductivity

²Matrix conductivity

HEAT FLOW

Surface heat flow provides another boundary condition required in the temperature at depth calculation. As a boundary condition, heat flow is challenging to determine for two reasons: it is susceptible to hydrologic disturbance and its sampling distribution is sparse. This work seeks to address these issues by including only measurements without obvious perturbations from groundwater and by producing a continuous map of heat flow over the entire state of Utah. This task is accomplished by compiling all available heat flow determinations for the state, augmenting the dataset with new measurements in areas with limited coverage, and ultimately using geostatistical methods to interpolate between measurements.

More than 450 measurements are available from previous academic works [Bauer, 1985; Bauer and Chapman, 1986; Bodell, 1981; Bodell and Chapman, 1982; Carrier, 1979; Carrier and Chapman, 1981; Chapman et al., 1981; Clement, 1981; Mase, 1979; Moran, 1991; Powell, 1997; Powell et al., 1988; Wilson, 1980] along with industry data in known geothermal resource areas (KGRAs) [Amax, 98] that assess heat flow using a classic technique. Much of the work using shallow boreholes offers dense coverage but exhibits sampling bias. For instance, many of the previous studies [Clement, 1981; Mase, 1979; Wilson, 1980] carry out work with a specific goal to define or delineate geothermal resources and so have sampled regions with anticipated high heat flow. Particular scrutiny needs to be given to shallow borehole sites before inclusion in a

picture of regional background heat flow. Also, hydrologic disturbance to shallow gradient holes is common where advective transport via ground water flow flushes or concentrates heat. These disturbances perturb heat flow locally and obscure the conductive background temperature field. It is not appropriate to use hydrologically disturbed boreholes in the calculation of temperature at depth. Additionally, the very near surface is affected by seasonal and climatic shifts in temperature; therefore wellbores shallower than 60 m are usually not considered. Studies utilizing heat flows determined from oil and gas wells [Funnell et al., 1996; Henrickson et al., 2001; Keho, 1987] attempt to reduce these hydrologic and climatic effects by acquiring information on temperature at depths below the influence of surface water flow or transitory temperature trends.

Measurements of terrestrial heat flow are made at discrete sites. Previous attempts to map heat flow, interpolating heat flow between measurement sites, include work by Blackwell and Steele [1989] and Blackwell and Richards [2004]. Standard practice for these methods is to apply a common inverse distance weighting interpolation algorithm, such as minimum curvature, and then manually adjust the result to fit the originator's sense for reasonable values and rates of change. These works provide useful estimates of terrestrial heat flow, yet rely heavily on the empiricism of the interpreter and do not provide quantifiable estimates of uncertainty.

Terrestrial heat flow is calculated by combining an estimate of the thermal gradient with thermal conductivity information. The type of temperature data used leads to two broad classifications of heat flow determinations: classic heat flow using a high resolution temperature log in a borehole at thermal equilibrium, and BHT heat flow using

one or two temperatures in oil and gas wells that may be out of thermal equilibrium. Each class of heat flow determination has its strengths.

The first method makes heat flow determinations in shallow gradient holes, taking advantage of a stable temperature regime after disturbances caused by the drilling process have dissipated. Circulation of drilling mud alters the natural temperature down hole. This disturbance is dependent upon how long circulation occurs and the amount of fluid being flushed from the borehole to the formation. Because these holes are shallow and sometimes drilled for observation rather than production, they can be cased and shut in for a sufficient duration that allows a return to in-situ conditions. A demonstration of this gradual return to natural conditions is demonstrated in the P-2A well, (Figure 11) where temperature logs were acquired periodically over 18 months subsequent to drilling. Measurements at different stages of re-equilibration illustrate the magnitude of disturbances caused to the temperature field near the borehole. Comparing three logs acquired immediately after drilling, to those acquired at 1 and 18 months following drilling, shows the field is depressed by 1 °C at total depth and elevated by more than 5 °C in the shallow section. A gradient determined from the un-equilibrated data would underestimate the true gradient by 14 °C/km.

Once equilibrated, some interpretation of the temperature log is required to select an appropriate interval from which to extract the gradient. A linearly increasing temperature with depth is characteristic of a conductive heat transfer regime, through material with a constant conductivity, and is the sought after trend. These trends can be obscured by a number of down hole conditions: changes in thermal conductivity cause changes in thermal gradient; convecting hydrothermal systems can cause temperature-

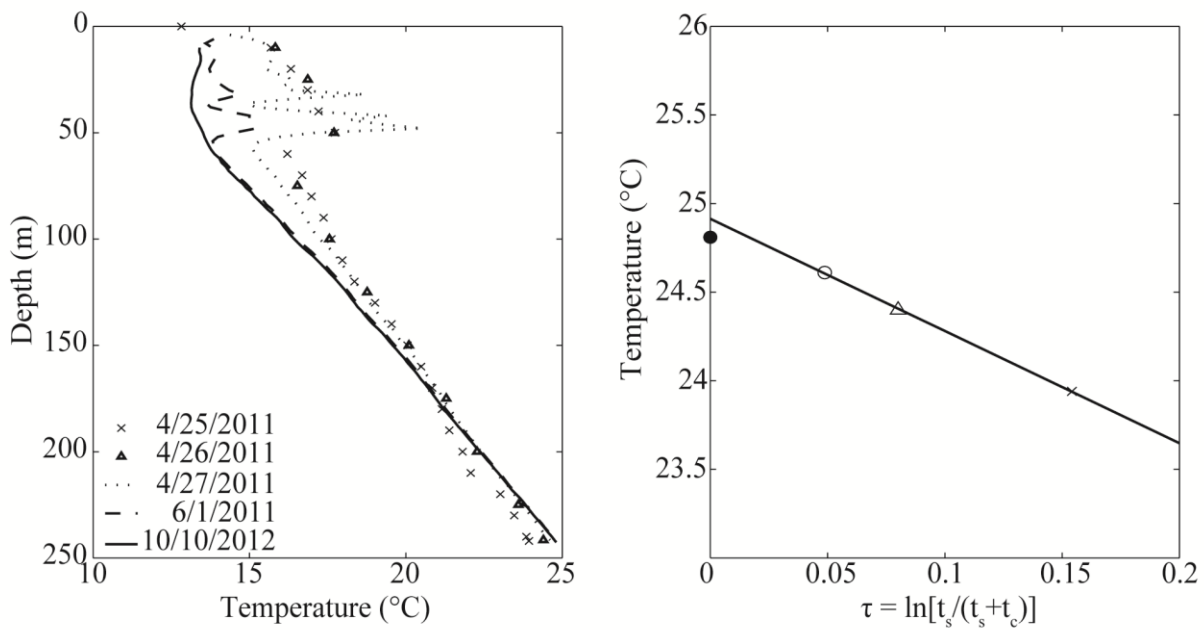


Figure 11. Thermal equilibration of the P-2A well. a) Temperature logs for the P-2A well. b) Horner correction to transient BHTs in the P-2A well performed on measurements taken during the 72 hours subsequent to drilling. Data from Gwynn et al. [2013].

depth profiles to be isothermal; variations in SGT attributed to seasonal or climate change produce transient variations very near the surface. Only sites where a conductive gradient is inferred were included for heat flow calculations in this study. For sites that meet this qualification the product of their gradient and the thermal conductivity gives heat flow:

$$q_0 = k \left(\frac{dT}{dz} \right). \quad (11)$$

The second method uses BHT data from oil and gas wells and the thermal resistance of the penetrated stratigraphic section to determine surface heat flow. A vertical section of thermal resistance is constructed based on the thickness of interpreted formations and measured or estimated conductivity. If there is minimal heat production through this horizontally stratified section of n layers, temperature at depth is given by:

$$T(z) = T_0 + q \sum_{i=1}^n \frac{\Delta z_i}{k_i}, \quad (12)$$

where T_0 is surface temperature, Δz_i is layer thickness, and k_i is the layer conductivity. Heat flow is determined by minimizing the difference between the observed BHT and calculated temperature at depth. A drawback to this method is the uncertainty in BHT records. Unlike gradient holes, temperature records in oil and gas wells are made immediately after drilling when the wellbore is still disturbed, requiring correction from transient to steady state.

A number of methods exist to correct disturbed BHTs, see for example Goutorbe [2007]. The most common correction is the general Horner plot method. This technique plots multiple uncorrected BHTs at a given depth against a unitless parameter τ as shown in Figure 11, where:

$$\tau = -\ln\left(\frac{t_s}{t_s + t_c}\right), \quad (13)$$

given t_s , the shut in time, and t_c the duration of circulation at the depth of interest. A Horner plot groups measured temperature versus τ . The temperature intercept of the linear regression provides undisturbed in-situ temperature, T_∞ , at $t_s \rightarrow \infty$ or $\tau = 0$. Horner corrections have been successfully used to estimate in-situ temperatures in Utah's Uinta Basin [Willett and Chapman, 1988; Keho, 1987] and Sevier Fold and Thrust Belt [Deming and Chapman, 1987]. This solution for undisturbed temperature requires at least a pair of BHTs with shut in times and provides a more confident estimate if there are multiple BHT-time pairs; that however is the exception more often than the rule. A further complication arises because temperature, which is not generally a principle objective for logging engineers and wellsite geologists, is frequently not recorded, misrecorded, or only recorded once despite multiple logging runs.

Because single BHTs at a given depth are most common, several approaches have been suggested to estimate equilibrium temperature from transient BHTs. Polynomial corrections with depth for single transient BHTs have been most widely used since the work of Kehle et al. [1970] and Harrison et al. [1983]. Harrison's work proposed that a static correction be calculated and applied to recorded BHTs:

$$T_{cf}(z) = -16.5 + .018z - 2.3 * 10^{-6}z^2, \quad (14)$$

where T_{cf} is the temperature correction factor (°C) and z is the depth (m) of the recorded BHT.

Later work by Blackwell and Richards [2004] observed bias in the Harrison correction that related to differences in thermal regimes and proposed a variation, which

is referred to as the SMU Correction. This correction applies an additional static shift to the Harrison corrected data as a function of regional gradients:

$$T_{cf_2}(\nabla T) = -0.84\nabla T + 23.98, \quad (15)$$

where ∇T is the regionally observed thermal gradient ($^{\circ}\text{C}/\text{km}$).

Work by Funnell et al. [1996], and later Henrickson et al. [2001], moves away from static corrections. These studies note that the slope of the Horner thermal recovery plot is related to depth and wellbore diameter. Wells are grouped by borehole diameter and Horner slopes from wells with multiple BHT records are plotted against depth. A linear regression places a best fit line through the points of each diameter grouping and coefficients are determined which allows an estimation of the Horner slope. With the regressed thermal recovery slope, m , a single BHT-time pair can be corrected to pre-drilling temperature (T_{∞}):

$$T_{\infty} = BHT + m \left(-\ln \left(\frac{t_s}{t_s + t_c} \right) \right). \quad (16)$$

Because of this method's use in association with the University of Utah, it is termed the Utah Method.

The Harrison, SMU, and Utah methods were evaluated against Horner corrected BHTs. As the Horner method is the most robust and widely used estimate of equilibrated down hole temperatures [Goutorbe, 2007], corrections from Horner plots were selected as the true temperature against which the other methods would be assessed. Eighty-nine wells throughout the Basin and Range had two or more recorded transient BHTs and were used for the comparison. Corrected BHTs were calculated using each method for all

transient BHTs. Differences between corrected temperatures (T_{calc}) and true temperatures (T_{true}) were computed and statistics of these residuals for each method were assessed. The Harrison correction generally over-predicts formation temperature with a mean residual 4 °C above true and a standard deviation of 10 °C. Corrections using the SMU method were much closer to the true formation temperature, under-predicting the true formation temperature on average by 2 °C with a standard deviation of 10 °C. This method shows large sensitivity to the selected regional gradient, shifting the static correction by approximately 80 percent of the difference between inferred regional gradient 34 °Ckm⁻¹ and 26 °Ckm⁻¹. The Utah correction produced steady state BHTs that were closest to the true temperature, over-predicting by 1 °C, but with a slightly larger standard deviation of 11 °C. A comparison of the three corrections is shown graphically in Figure 12. While variation on the order of 10 °C is common [Goutorbe, 2007], inaccuracies in any given single point BHT correction could be as large as 22 °C. For this study, a sufficient spatial coverage of reliable heat flow data was available, and so the more variable single point corrected BHTs were not included for the final heat flow map.

This study builds on the previous 410 heat flow measurements determined to be representative of background, adding 5 sites from the recently drilled Utah Geological Survey drilling program as well as calculating heat flow in 44 oil and gas wells. Shallow gradient wells drilled in BRD ranged from 81 mWm⁻² in PA-3 to 89 mWm⁻² in P2-A with a mean heat flow 84 mWm⁻². In addition to the shallow gradient holes, new heat flows were calculated in 44 oil and gas wells throughout the state, 19 of which are in the Basin and Range. Calculated heat flows of the Basin and Range measurements vary between 41 mWm⁻² and 145 mWm⁻² and have a mean value 89 mWm⁻² which compares favorably

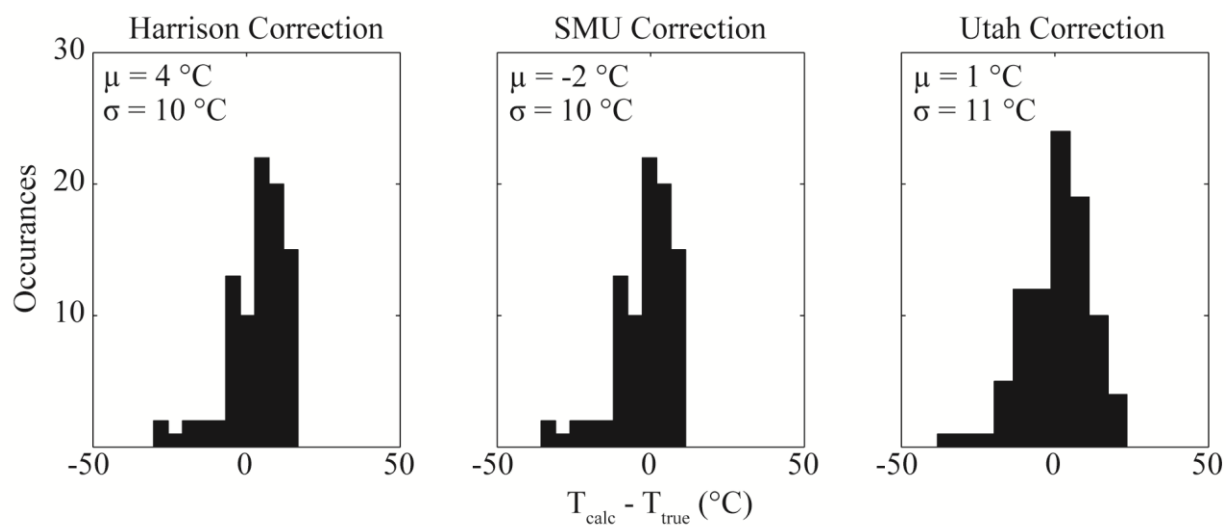


Figure 12. Comparison of three BHT correction methods. Differences calculated between each of the three techniques and Horner corrected temperatures.

with the 90 mWm^{-2} value from Chapman et al. [1979]. A histogram of heat flows for both the Colorado Plateau and Basin and Range provinces can be seen in Figure 13. All heat flow values determined for the study are summarized in Appendix C.

Compiling a heat flow database of discretely sampled heat flows is a step toward the ultimate goal of calculated temperature at depth over a continuous region. The aggregate of previously existing works and new measurements provides adequate spatial coverage for a statewide interpolation; however, realizing a satisfactorily gridded representation of continuous heat flow requires the selection of an appropriate interpolation scheme. As with other geologic interpolation problems, choosing a method that adheres to realistic behavior of the property of interest through space is crucial to producing a credible result.

Two interpolation methods were tested before arriving at a final heat flow map. The first was ordinary kriging and the second was a convergent interpolation algorithm. Generally, interpolation techniques follow variations of the weighted difference scheme. Weighted difference gridding algorithms can be considered in two broad classes: integral and statistical. As described in Smith and Wessel [1990], integral methods attempt to minimize the overall misfit between data and the gridding function. These methods return results over the entire domain, however, they do not give a quantitative sense for how well constrained the result is. Geostatistical methods, on the other hand, assess and leverage the spatial correlability of control data (Figure 14) and minimize the error variance at each point of estimation, while honoring all input data. Through this minimization, a quantitative estimate of how well constrained the interpolation is in

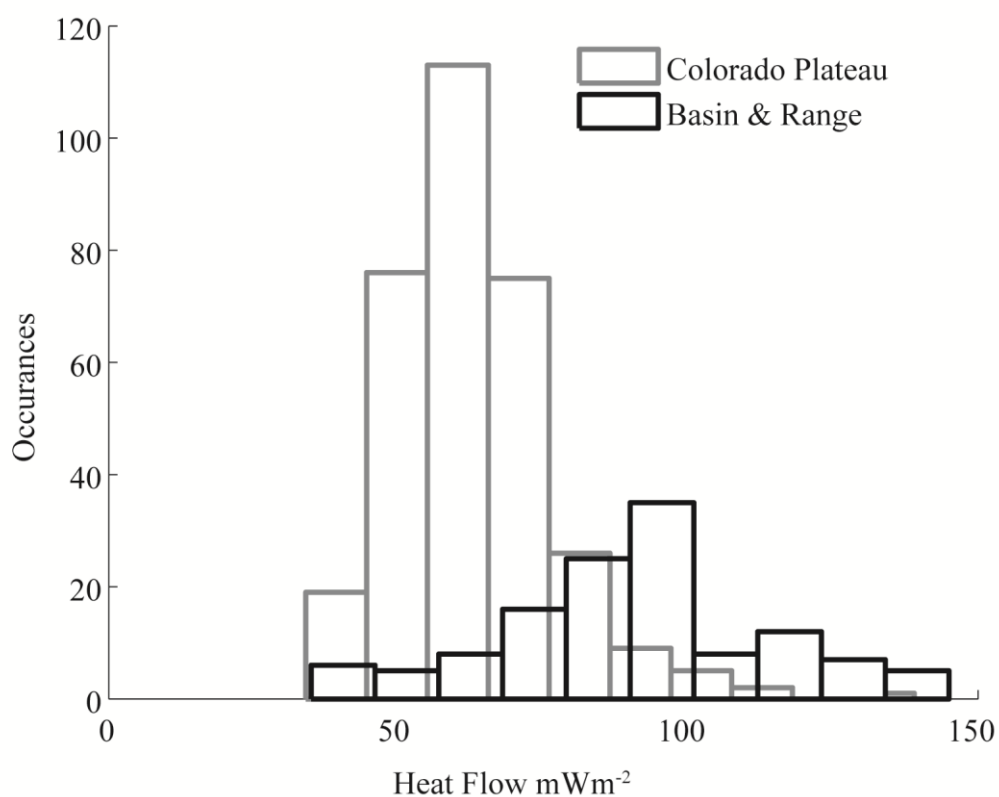


Figure 13. Distribution of heat flow measurements on the Colorado Plateau and Basin and Range. Basin and Range heat flows are distinctly higher than those of the Colorado Plateau, however, showing more spread.

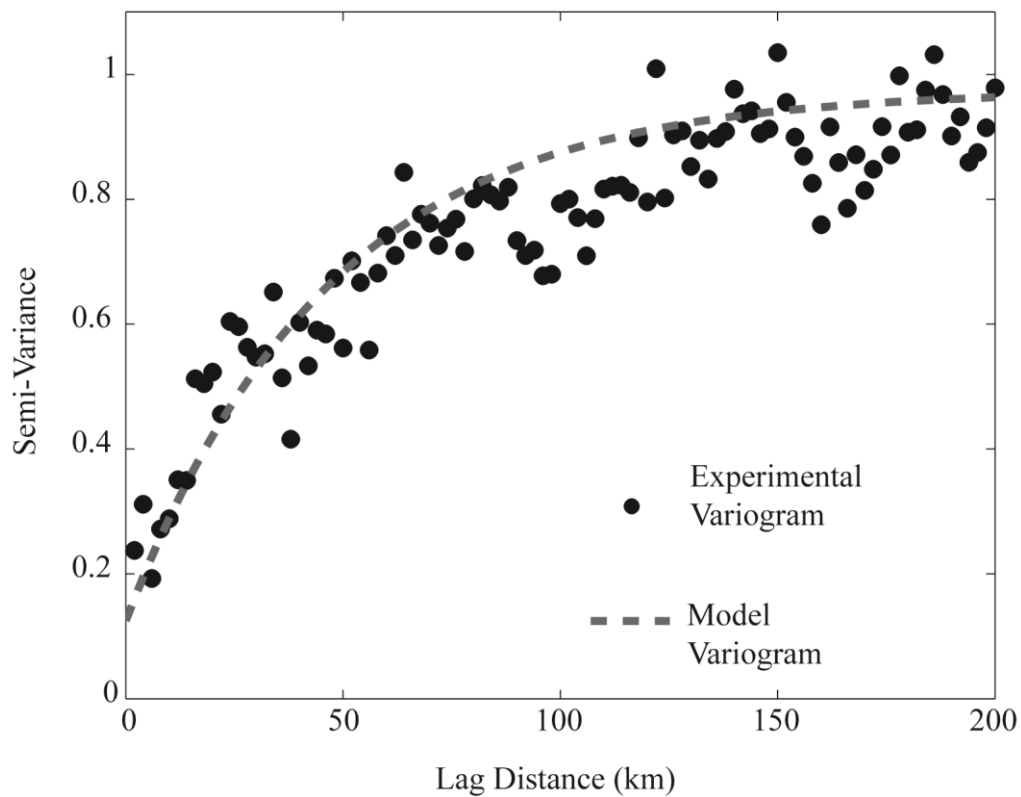


Figure 14. Spatial correlability of heat flow sites across Utah. Normalized omnidirectional variogram shows experimental variogram points fit by a modeled exponential variogram with a small nugget contribution of about 15%, depicted as a dashed line. This graphic illustrates that heat flow sites have the best spatially correlability at distances of less than 50 km.

reference to the variance of the dataset can be made. Geostatistical methods are limited in regions of sparse data, falling back to the local mean of the data. The results of both techniques are shown in Figures 15-16 with the estimate of the kriging variance shown in Figure 17.

The mapped grids show generally lower heat flow on the Colorado Plateau and higher heat flow in the Basin and Range. Distributions of the gridded results were bimodally distributed with peaks corresponding to the two distinct heat flow provinces, Basin and Range and Colorado Plateau. The modes of both grids compared favorably with those of the input data with peaks at 92 mWm^{-2} and 62 mWm^{-2} for the convergent interpolation and 89 mWm^{-2} and 61 mWm^{-2} for the krig, compared to 89 mWm^{-2} and 63 mWm^{-2} of the input data. The total extents of the convergent interpolation were however, greater than those of the input data ranging from 24 mWm^{-2} and 150 mWm^{-2} , as opposed to the input and kriged range from 34 mWm^{-2} to 145 mWm^{-2} .

To preserve the remaining heat flow information from sites not included in the gridding, all data were plotted as discrete values over the continuous background heat flow surface Figure 18. Ultimately, the convergent interpolation appears to be less stable than the ordinary kriging interpolation results and provided no estimate of the interpolation uncertainty; therefore the kriging algorithm was selected to best represent background heat flow and the boundary condition for the calculation of temperature at depth.

Elevated trends are observed in both grids through the GSL region where heat flow ranges from 105 mWm^{-2} to 115 mWm^{-2} and in the southern Basin and Range which

reaches heat flows as high as 145 mWm^{-2} . The trend in the GSL region is both well constrained and laterally extensive while the trend in the southern Basin and Range varies laterally.

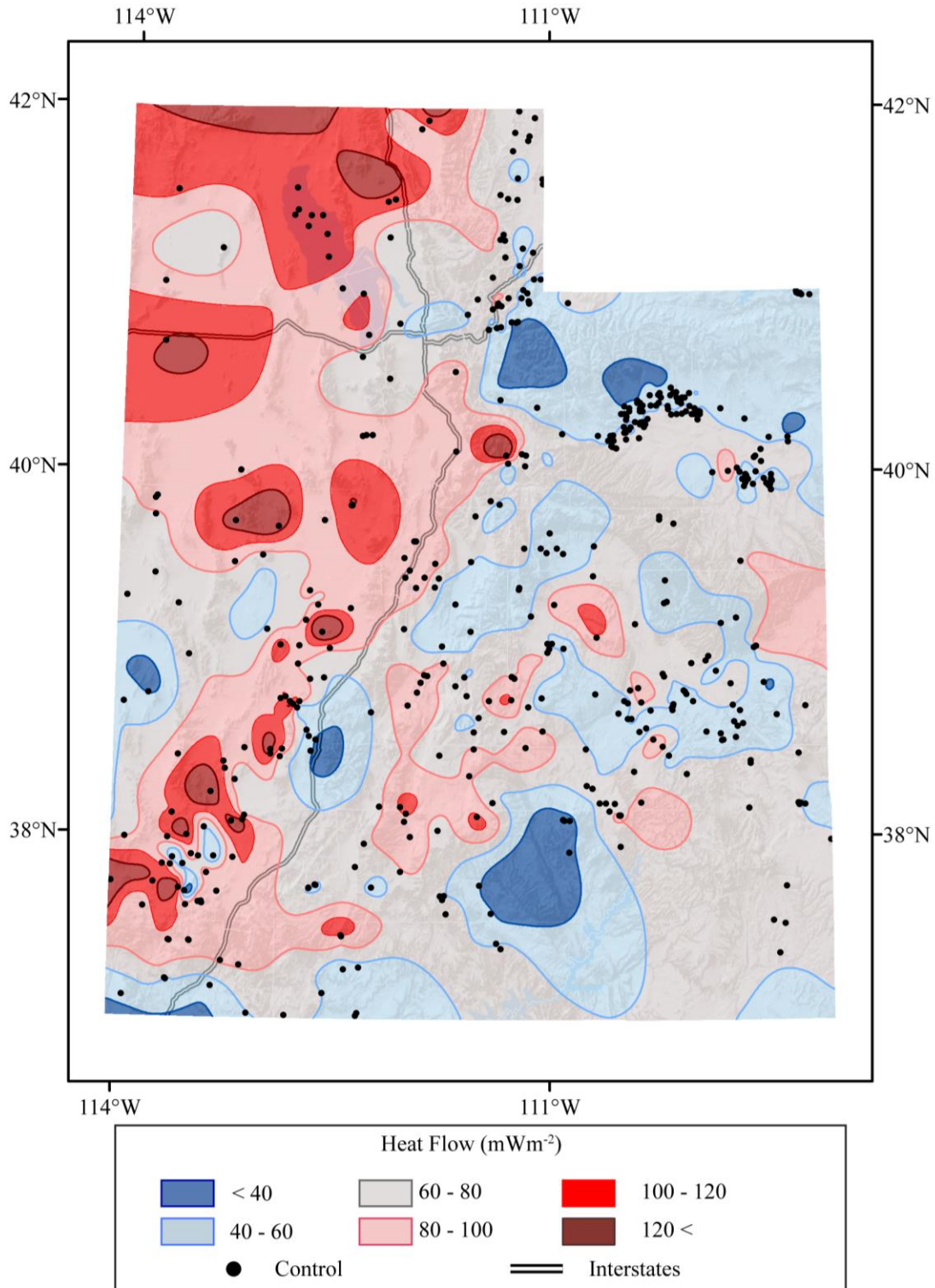


Figure 15. Heat flow for the state of Utah from convergent interpolation scheme. The GSL region shows the broadest range of high heat flow (appearing as a dark to light red swath in the north) while the highest heat flows are recorded in the BRD but are much less laterally continuous.

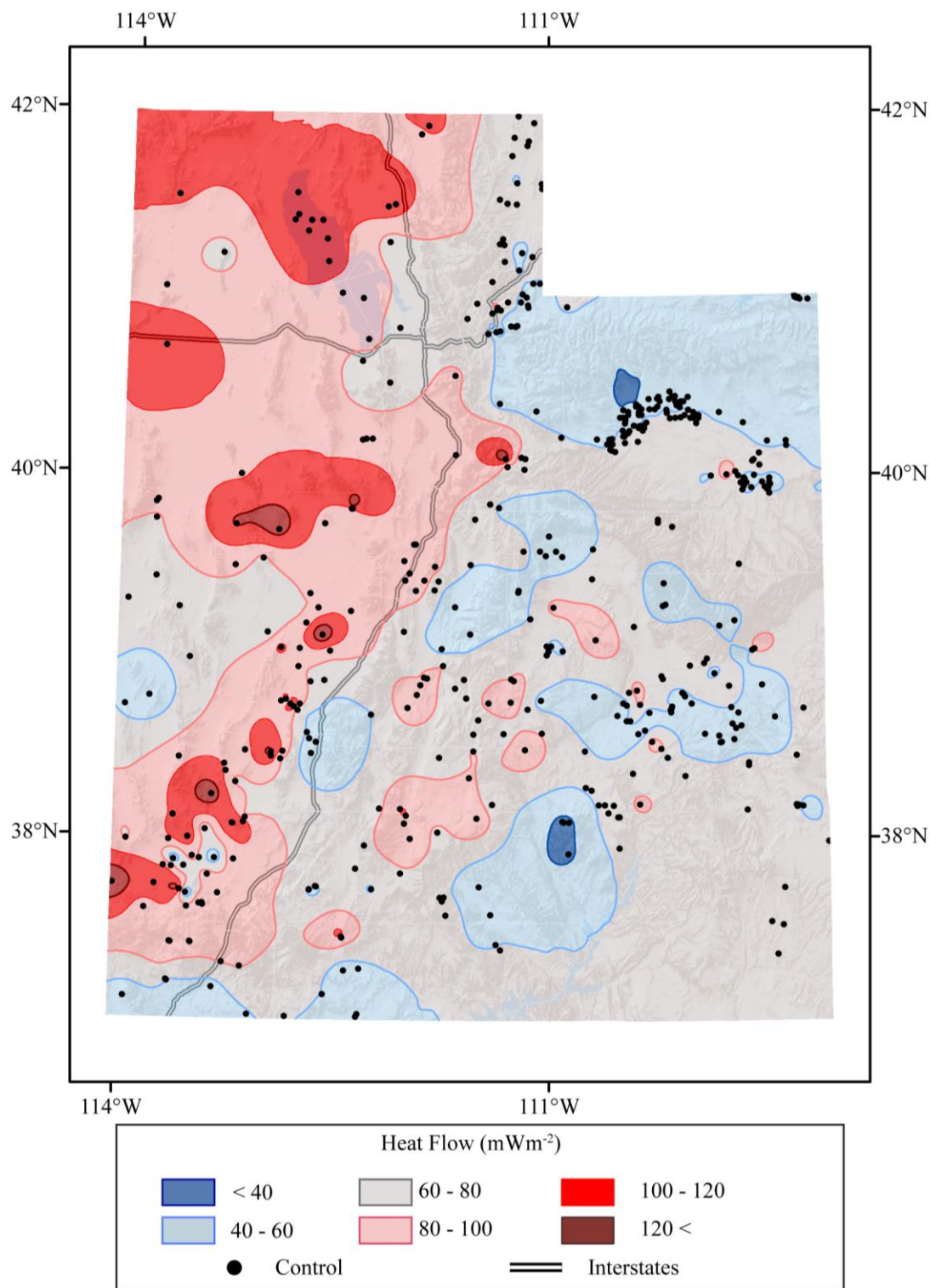


Figure 16. Heat flow for the state of Utah from ordinary kriging scheme. Result of gridding data from Basin and Range and Colorado Plateau that considers spatial correlability of the data. The GSL region shows the broadest range of high heat flow—as in the convergent interpolation.

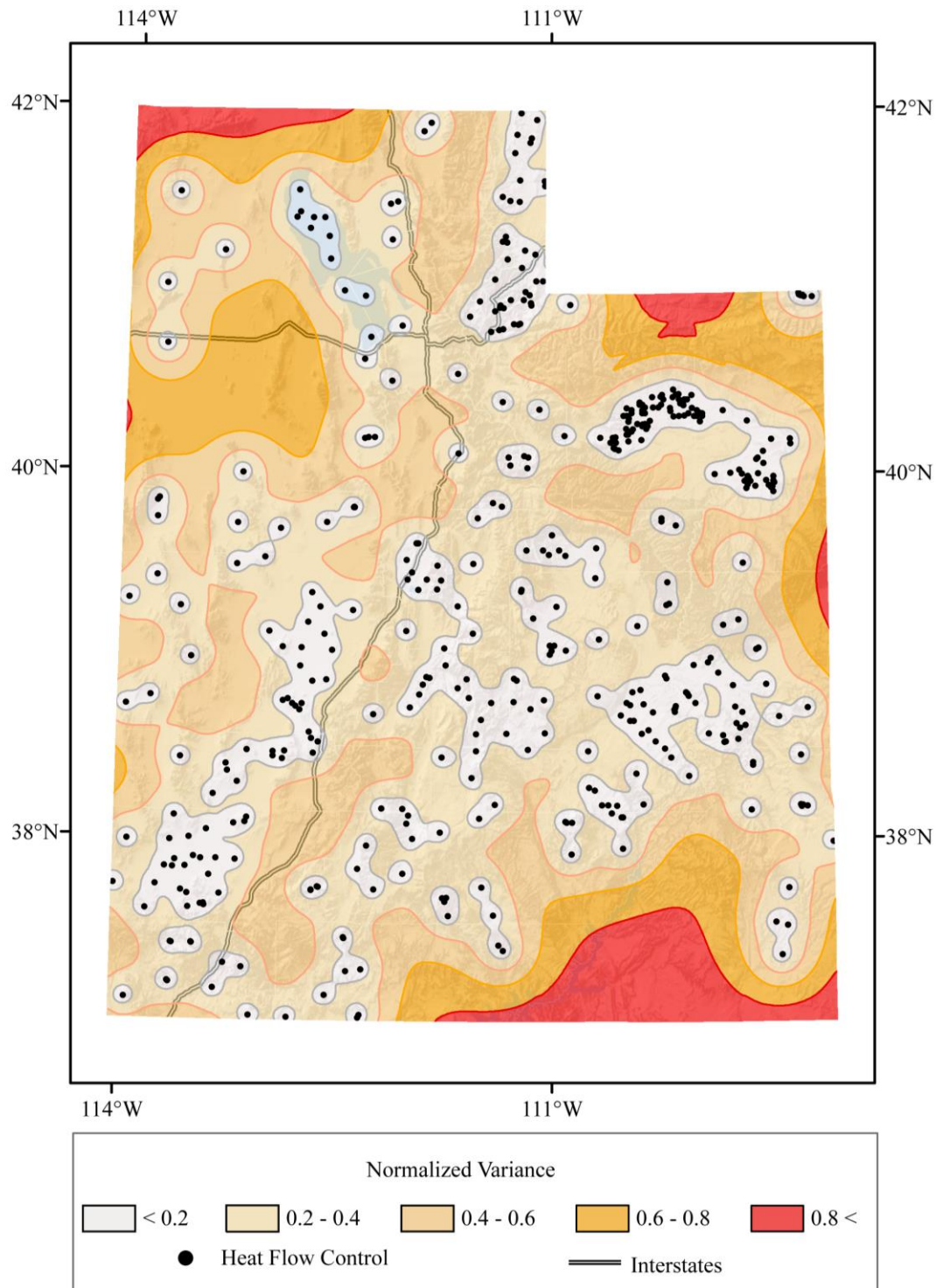


Figure 17. Normalized kriging variance for Utah heat flow. As the kriging algorithm searches beyond the variogram range for control data, the kriging estimate becomes the local mean. Red and orange indicate the highest variance near or beyond the variogram range (150 km). Three regions along the edges of the state appear to be poorly constrained: northwestern Utah, northeastern Utah, and in southeastern Utah.

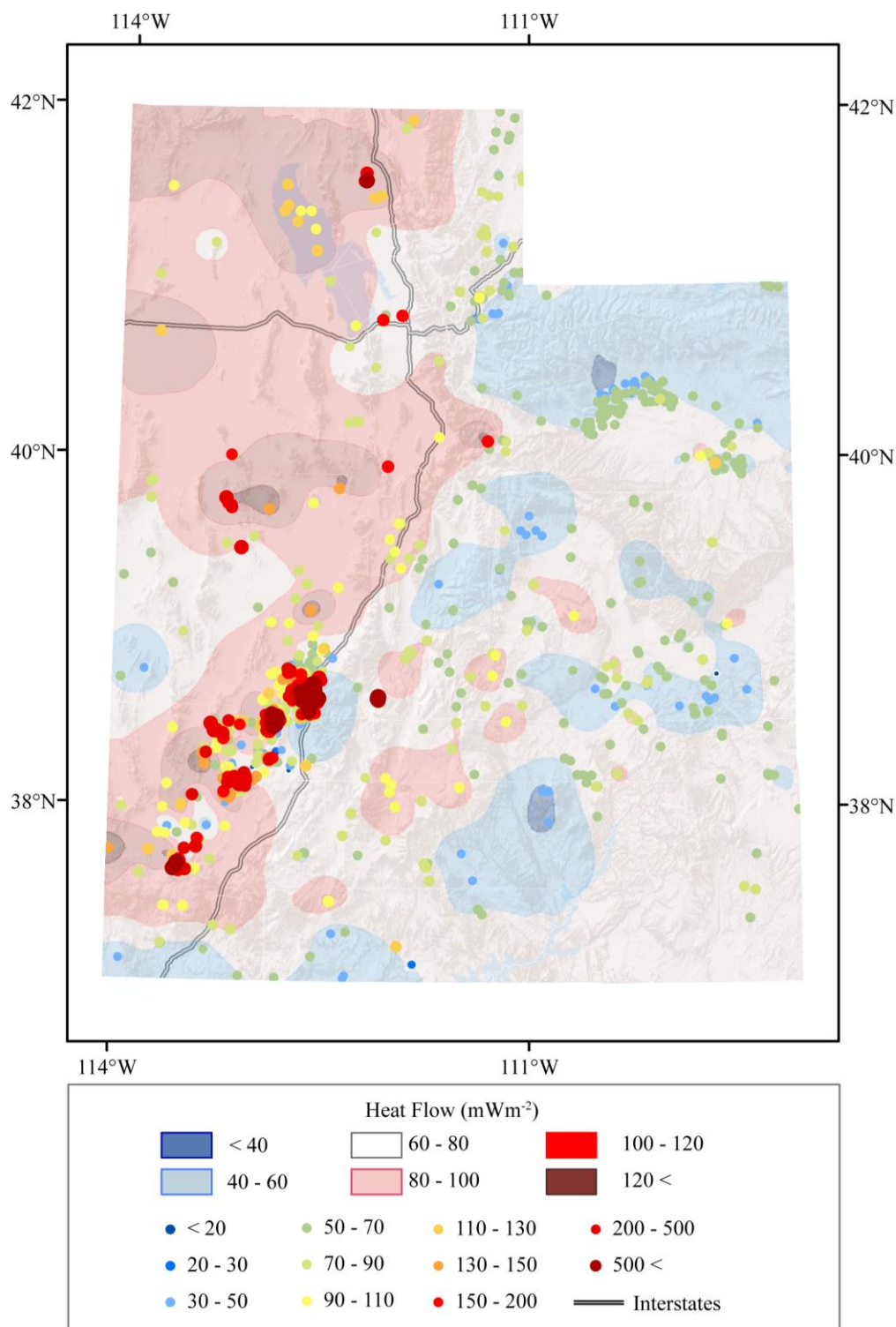


Figure 18. Heat flow measurements in the state of Utah. All of approximately 800 heat flow sites measured throughout the state are displayed, as colored points, over the kriged heat flow map for comparison. High density clusters of heat flow in excess of 0.5 Wm^{-2} surround known geothermal resource areas with active direct use or energy production.

TEMPERATURE FIELDS

The culmination of this work is mapping temperature at depth in the Basin and Range of Utah. Temperature can be conveniently portrayed on 2D cross-sections, illustrated as contoured depth to isotherms, or temperatures at selected depths. As examples of the first of these mapping styles, two cross-sections were constructed along basin axes in regions with elevated mapped heat flow and located to intersect wells with temperature control for model validation. The first was located in the GSL region, where mapped heat flow was consistently greater than 100 mWm^{-2} through broad basins. The second was located in the BRD, where recorded heat flows were highest but more rapid lateral changes were observed.

The temperature fields in each cross-section were modeled numerically by a finite difference scheme, developed in Matlab, using relevant boundary conditions and interior properties. Finite difference schemes have been used previously to solve for temperature fields in both 2D and 3D domains [Beardsmore and Cull, 2001]. The model coded for this study uses a surface boundary held at a specified temperature distribution, a base condition of specified heat flow, lateral boundaries with zero flow, and an interior populated with in-situ thermal conductivity for a number of geologic units.

Regional control on geology was taken from nine surfaces mapped and described as part of a United States Geological Survey (USGS) project to understand regional scale

hydrologic flow in the Basin and Range [Heilweil and Brooks, 2011]. The following nine units, from oldest to youngest, were mapped and are described in Table 2 and Figure 19: Noncarbonate Unit (NC), Lower Carbonate (LC) Unit, Upper Siliciclastic Unit (US), Upper Carbonate Unit (UC), Thrusted Noncarbonate Unit (TNC), Thrusted Lower Carbonate Unit (TLC), Volcanics Unit (VU), Lower Basin-Fill Unit (LBF), Upper Basin-Fill Unit (UBF).

The nine hydrogeologic units mapped represent distinct physical characteristics that impact fluid flow, namely lithologic and hydraulic properties. Because thermal conductivity is dominantly controlled by the rock matrix composition and pore space volume, these units of hydrostratigraphic significance are particularly applicable to the thermal modeling problem. These hydrogeologic unit (HGU) surfaces were used to construct the majority of the model framework.

One additional unit, near surface lake bed clays, which was sampled and well characterized by the five UGS gradient wells, was also included in the model framework. A surface that represents this unit was generated and constrained by surface geological maps and well penetrations.

A grid was constructed in Schlumberger's Petrel 2011.2 as a 16 million cell model with uniform rectangular dimensions (1000x1000x100 meters). Individual cells were assigned index values corresponding to the HGU at each cell center. Storing only indices allows properties associated with a given unit to be assigned during the temperature field calculation, limiting the amount of storage and computational expense required when manipulating the grid.


	Hydrogeologic Unit	Stratigraphic Unit
Q	UBFAU	Basin-fill deposits Basalt
T	LBFAU	Garrett Ranch Group North Horn Fm
	VU	Volcanic rock
Mz	TLCAU	Thrustured rocks of the Sevier Fold and Thrust Belt 
	TNCCU	
P	UCAU	Oquirrh Group
IP		
M	USCU	Manning Canyon Sh.
D	LCAU	Great Blue Fm Humbug Fm
S		Gardison Limestone
		Water Canyon Fm
O		Laketown Dolomite
		Garden City Lime
C		Teutonic Limestone
PC	NCCU	Pioche Formation Tintic Quartzite

Figure 19. Hydrogeologic unit groupings. Modified from Heilweil and Brooks [2011].

Table 2. Hydrogeologic unit descriptions*

HGU	Abbreviation	Age	Description
Upper Basin-Fill Unit	UBF	Quaternary	Mostly unconsolidated basin-fill occurring syndepositionally with Basin and Range extension
Lower Basin-Fill Unit	LBF	Tertiary to Quaternary	Deepest basin fill
Volcanics Unit	VU	Tertiary	Volcanic intrusions and accumulations
Thrust Noncarbonate & Lower Carbonate Units	TNC & TLC	-	Repeat of the two deepest units
Upper Carbonate Unit	UC	Pennsylvanian through Permian	Shallow marine carbonates
Upper Siliciclastic Unit	US	Devonian to Mississippian	Siliclastic sediments shed from Antler Orogeny
Lower Carbonate Unit	LC	Cambrian through Devonian	Carbonates
Noncarbonate Unit	NC	Early Paleozoic and older	Metamorphosed basement

*Hydrogeologic units as described in Heilweil and Brooks, 2011.

Populating the grid interior required determining in-situ thermal conductivity. Lab measurements of thermal conductivity provide the conductivity of rock matrix. A volume of rock in place, however, is composed of both rock matrix and fluid filled pore space. A two component volumetric mixing expression provides a reasonable estimate of thermal conductivity in the subsurface:

$$k_{insitu} = k_{matrix}^{(1-\Phi)} * k_{water}^{\Phi}, \quad (17)$$

where k_{matrix} is the thermal conductivity of the rock matrix, k_{water} is the thermal conductivity of pore fluid which is assumed to be water, and Φ is the total porosity.

Matrix thermal conductivities and their statistics are known where the HGUs intersected each well with measured conductivity. The thermal conductivity of water is known to be $0.6 \text{ Wm}^{-1}\text{K}^{-1}$, and porosity requires further estimation.

Porosity in the geologic section can be highly variable for a number of reasons including sedimentation rate, depositional environment, and chemical cementation; however, it has been observed that despite these processes, decreasing porosity with depth can be approximated to a first order by an exponential function [Bahr et al., 2001]. Porosity in the subsurface is characterized by establishing unique compaction trends for each HGU. Neutron-density cross-plot data were sampled at 30 meter intervals from logs for ten key wells in the GSL and BRD regions. Hydrogeologic unit intersections with each well were plotted (Figure 20) and porosity-depth relationships were grouped by unit. Exponential decay trends were fit through the porosity-depth pairs for each HGU (Figure 21) and assessed for goodness of fit. With matrix conductivity and porosity constrained, in-situ thermal conductivity is calculated and populated for each cell in the model.

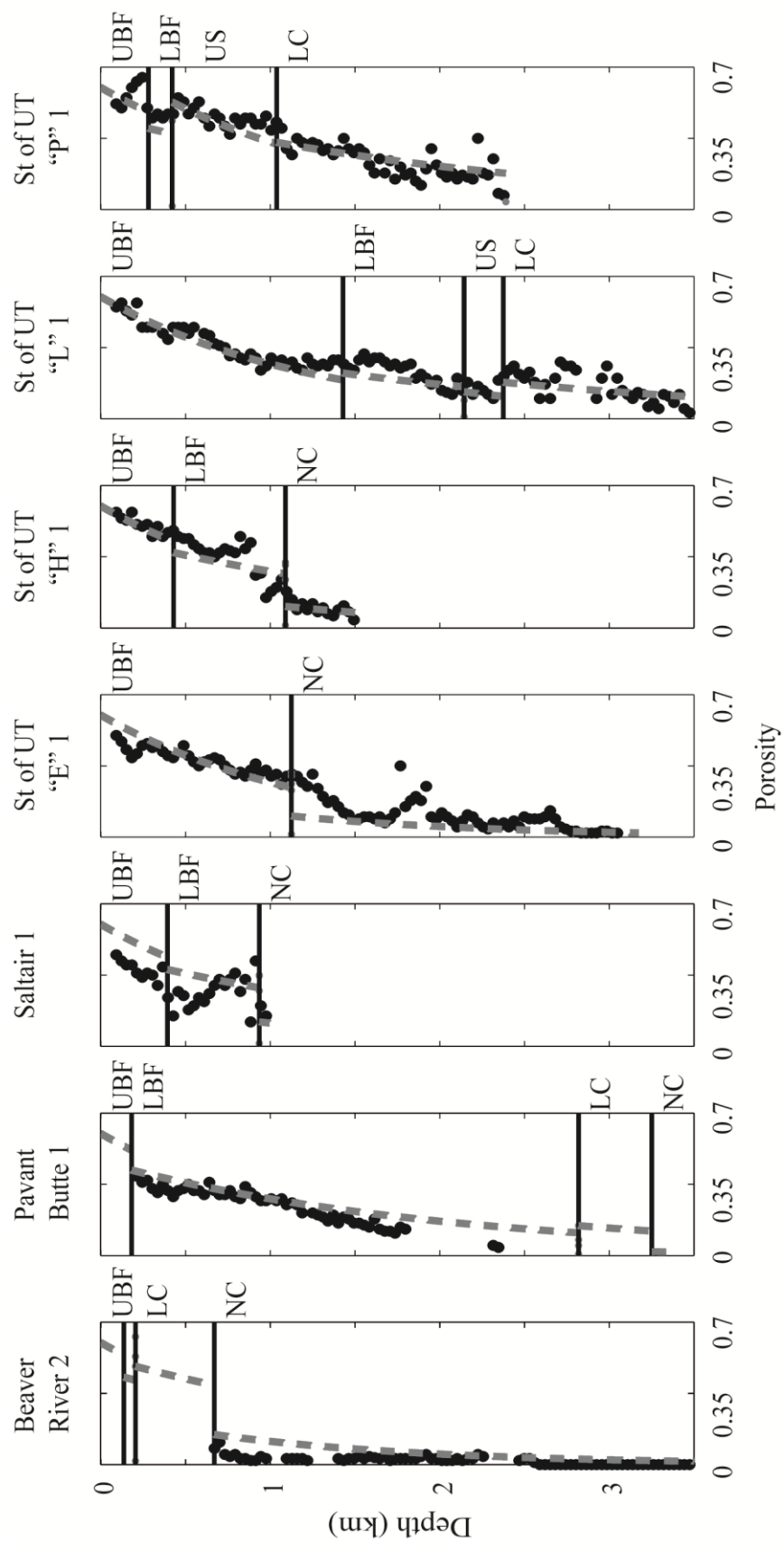


Figure 20. Porosity trends in the GSL and BRD regions. Wells are subdivided into depth sections of hydrostratigraphic units, each having its own porosity trend. Measured porosity is shown as black circles; dashed lines show the general compaction trend for each HGU.

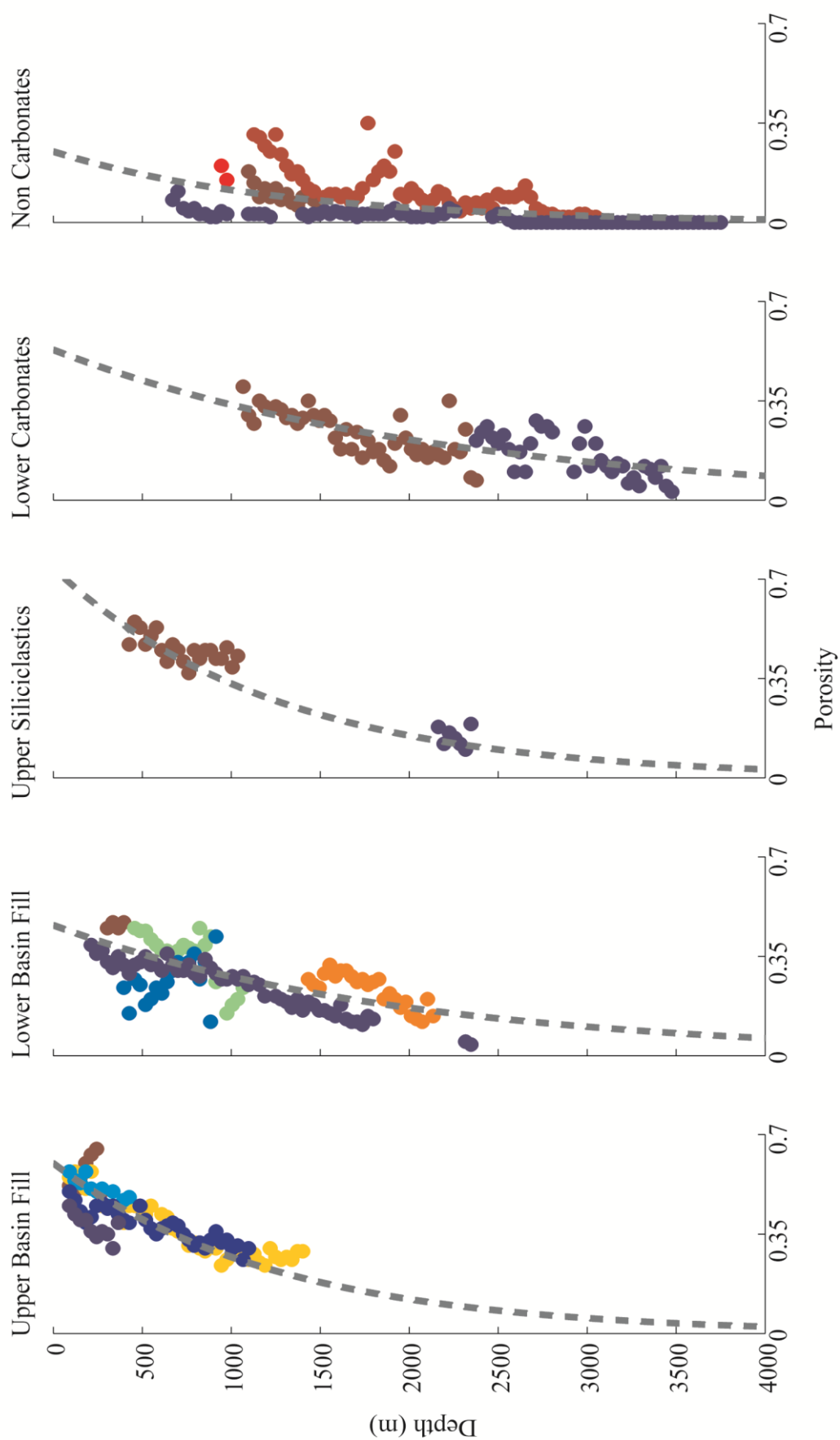


Figure 21. Porosity trends in the GSL and BRD regions for encountered HGUs. Measured porosity is shown in circles and the generalized compaction trend for each HGU is dashed in grey. Colors indicate individual wells tabulated for porosity measurements.

With boundary conditions and internal parameters established, the finite difference model is run to convergence. In a finite difference, or relaxation, model each cell is checked for thermal equilibrium with adjacent cells until its change is less than a specified convergence tolerance. For iterations prior to reaching the convergence criterion, the cells are assigned new values based on the difference between each cell's neighbors and then checked again for convergence to thermal equilibrium. For sufficiently small thermal equilibrium tolerances, many tens of thousands of iterations can be required. To reduce the computational expense, the model is originally seeded with an analytic solution for 1D temperature along each vertical column of the cross-section before proceeding with 2D relaxation. Providing a 1D approximation of the temperature field reduces the required iterations from tens of thousands to hundreds and drops the overall run time from minutes, for a single cross-section, to seconds.

The resulting temperature fields are presented in Figures 22-23. The GSL region cross-section (Figure 22) was located to pass through two oil and gas exploration wells with temperature control—State of Utah “L” 1 (API: 00330010) and Indian Cove State 1 (API: 00330002)—in the center of the basin. Good agreement was found between the modeled temperature field and temperature observations at the wells. Temperatures greater than 150 °C are observed at less than 3 km depth and 200 °C is observed between 3.5 km and 5 km. Absolute percent errors were calculated between the temperature data and the modeled temperature field at coincident locations. The mean of absolute percent errors was 3% indicating that the modeled field overpredicts temperature by a small amount.

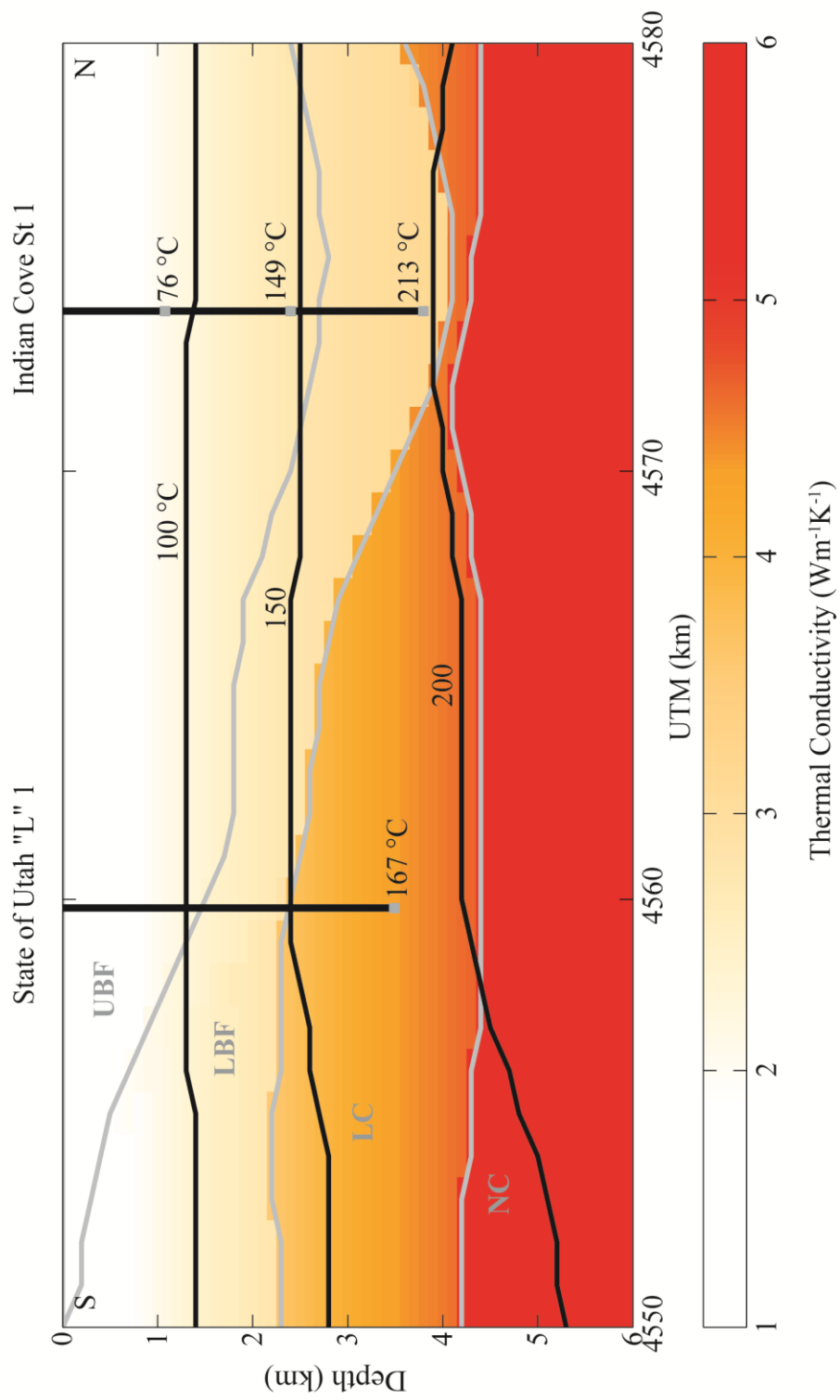
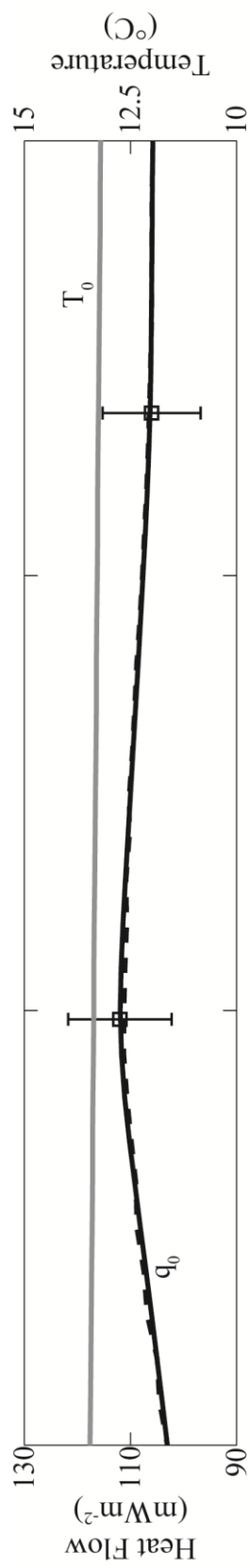


Figure 22. Temperature cross-section in the GSL region. The panel above the cross-section includes mapped (solid black) and model calculated (dashed) heat flows along with surface temperature, T_0 , (solid grey). Hydrogeologic surfaces along the section are shown in light grey and labeled accordingly. A colormap from white to red illustrates changing conductivity throughout the section. The temperature field is shown to 6 km with the 100 °C, 150 °C, and 200 °C isolines in black. Nearby wells with BHT data are projected in to compare observed temperatures to the model.

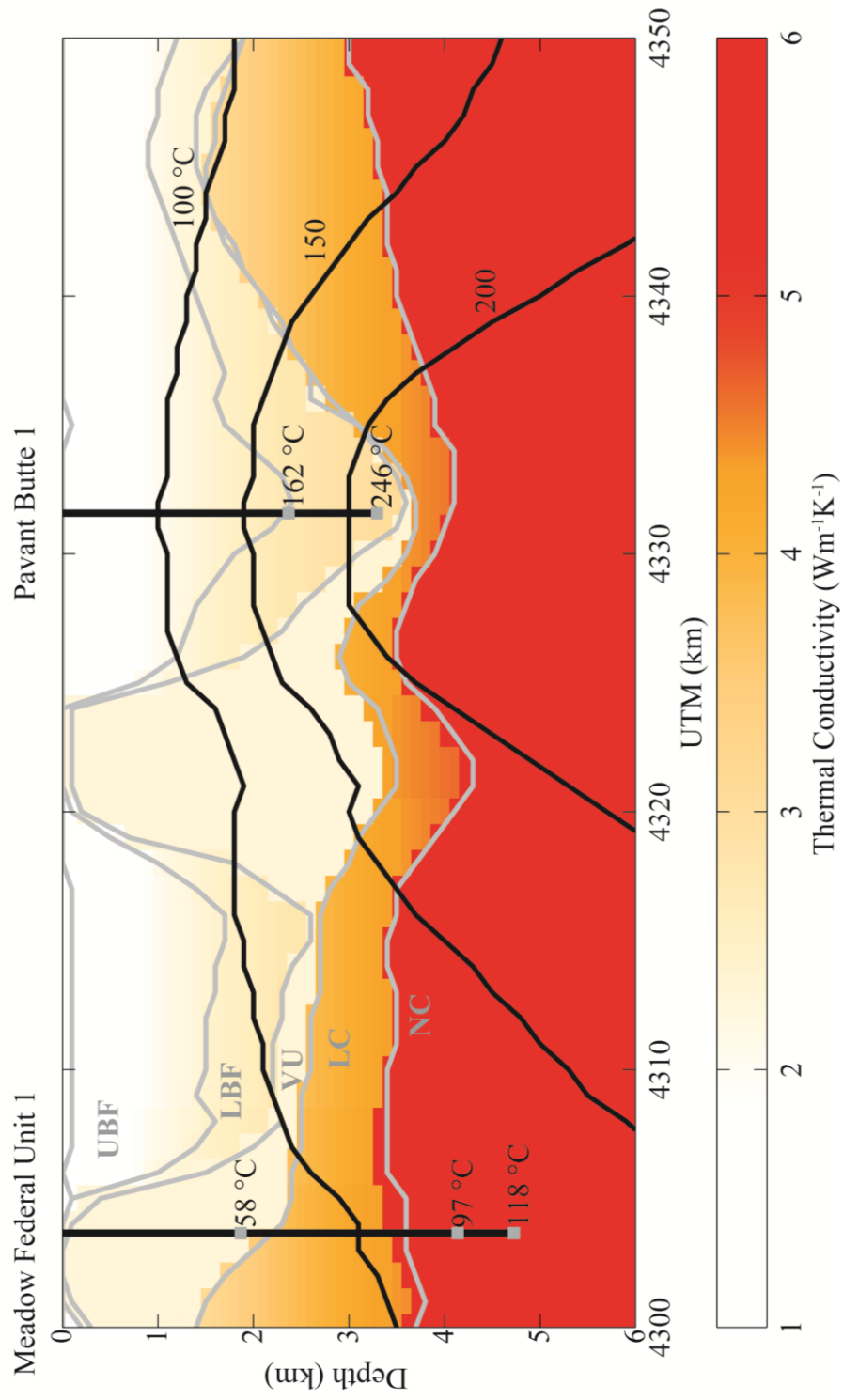
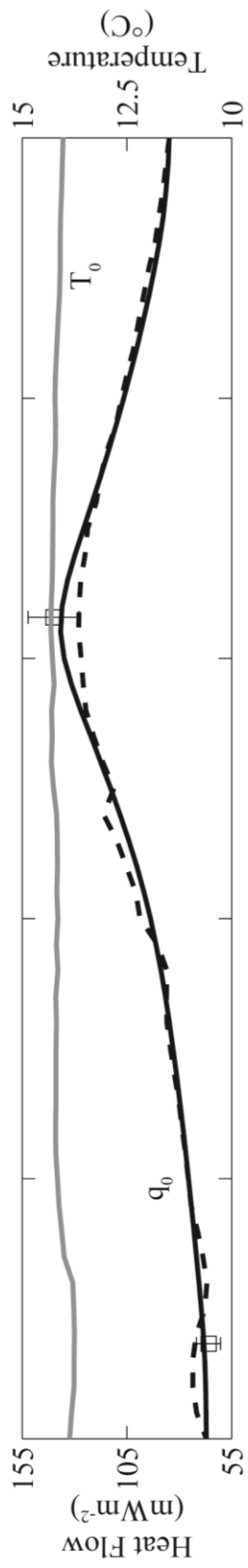


Figure 23. Temperature section in the BRD region. The section is presented as Figure 21 with the addition of the volcanic HGU which was not present in the GSL region.

The BRD region cross-section (Figure 23) was also placed to intersect two key wells—Pavant Butte 1 (API: 02730027) and Meadow Federal 1 (API: 02730028). The BRD region appears to be cooler than GSL above 4 km, generally reaching 150 °C at depths between 3 km and 4.5 km and 200 °C at depths beyond 5 km. An exception occurs in a 5 km radius around Pavant Butte 1 where temperatures reach 150 °C at 2 km and 200 °C at 3 km depth. Temperature control and the modeled temperature field show reasonable agreement, with a 10% mean of absolute percent errors and a maximum mismatch of 31% at the shallow record in Meadow Federal 1. Two explanations exist for the larger observed discrepancy at BRD compared to GSL. The first considers a mismatch between well intersections with the HGUs and the actual depth to formations penetrated during drilling. The second considers geologic factors not accounted for in the model and their impact on the resulting temperature field.

As the HGUs approximately correspond to a specific portion of the stratigraphic section, their accuracy can be assessed at the wells where subsurface control is best. For the two wells on the BRD cross-section, tops are compared to the HGU intersections and the offsets are presented in Table 3. Depth to hydrogeologic units at Pavant Butte 1 are significantly deeper than the observed geology and at Meadow Federal 1, the HGUs replace 1900 meters of Tertiary sediments with volcanics to surface. The study evaluates the impact of these observed offsets in one-dimensional temperature profiles calculated at each well. The 1D profiles used the same boundary conditions as the two-dimensional case. A 1D basecase was established for each well by calculating the temperature field using the HGU intersections. For the Meadow Federal 1, the largest misfit was a 25% or 14 °C overprediction at 1900 meters, the smallest misfit was a 1% or 0.5 °C

Table 3. Stratigraphic control mismatch*

Well	Top Name	Top Depth (m)	HGU Name	HGU Depth (m)	Difference (m)
Pavant Butte 1	Quaternary	0	U. Basin Fill	0	0
	Miocene	640	L. Basin Fill	2800	-2160
	Volcanics		Volcanics	3800	
	Chisholm	2987	L. Carbonates	3900	-913
	Prospect Mountain Quartzite	3234	Noncarbonates	4100	-866
Meadow Fed. 1	Quaternary	0	U. Basin Fill		
	Tertiary	5	L. Basin Fill		
	Volcanics		Volcanics	0	
	Cambrian Carbonates	1780	L. Carbonates	1900	-120
	Prospect Mountain Quartzite	3960	Noncarbonates	3600	360

*Well stratigraphy compared to regionally mapped hydrogeologic unit equivalent.

overprediction at 4700 meters, and the average misfit was 14%. Correcting the stratigraphic section to that observed at the well and recalculating reduced the overprediction to 20% or 12 °C at 1900 meters, 8% or 10 °C at 4700 meters, and the overall misfit to a 5% overprediction. At Pavant Butte 1, the same approach was taken for the original case. The largest misfit was a 14% or 22 °C overprediction at 2400 meters, while the smallest was an 8% or 19 °C underprediction at 3300 meters, and the overall underprediction was 3%. Changing the stratigraphic column to better reflect the rocks encountered during drilling and recalculating the temperature field improves the underprediction nominally to 6% or 16 °C at 2400 meters, but slightly raises the error at 3300 meters to 17% or 28 °C, and the overall error to 4%.

The conductive heat flow model for temperature in the subsurface is relatively simple, making the assumption that a single basal heat source is the only heat input. With this assumption, the model may fail to characterize the temperature field accurately in the presence of young volcanics and cooling intrusions which provide heat input to the model interior. The eastern BRD is known for active volcanism throughout the Cenozoic particularly in the last million years [Hintze and Davis, 2003]. Basalts, as young as 10,000 years, are found immediately adjacent to the Pavant Butte 1 in the Pavant Butte volcanic field. Basaltic cinders and tuffs have also been described within 10 km of the Pavant Butte 1 [Hintze and Davis, 2003]. Temperatures and heat flow in the Pavant Butte 1 are the highest recorded for any oil and gas well in the state of Utah. In the context of the abundant volcanic activity in close proximity, the Pavant Butte 1 may not be representative of a regional heat flow regime with only basal input. Instead, the elevated temperature records and calculated heat flow are likely due to the cooling of nearby

volcanics. Based on these observations the thermal regime at Pavant Butte 1 should be treated as anomalous in the regional context.

SYNTHESIS

The primary objective of this study was to identify high temperatures at accessible depths for potential future geothermal development in the sedimentary basins of Utah's Great Basin Province. The regional resource assessment required the development of new digital infrastructure composed of an integrated thermal database and temperature modeling code. A thermal database was constructed with over 1300 sites containing a variety of thermal data that included the following: 323 wells with corrected BHTs where 44 are newly determined, more than 850 tabulated temperature logs, and 2300 thermal conductivities of which more than 460 were new measurements. A finite difference code was written in Matlab, a broadly accessible and inexpensive platform, designed to model steady state temperature fields through stratified basins using boundary conditions and rock properties derived in previous chapters.

The final temperature sections focus most closely on two areas: the Great Salt Lake region—marked by a broad swath of high heat flow, elevated above the typical Basin and Range values, and close proximity to a population center—and the Black Rock Desert—because it contained the highest recorded heat flows. Temperatures determined in the BRD generally did not exceed 150 °C above depths of 3000 m and misfit between the well control and the calculated temperature field was less than 15% across this region. The observed misfit and rapid lateral changes in heat flow is attributed to the presence of unaccounted for intrusives and volcanics. In the Great Salt Lake region, temperatures

greater than 150 °C have been identified at depths as shallow as 2700 m. Because the GSL cross-section is placed in a broad basin with relatively simple geology, modeled temperatures are predicted with greater confidence than those in the BRD.

To quantitatively assess the amount of thermal potential, heat content was calculated in the fashion of Tester et al. [2006], where temperatures exceed 150 °C, between 3 km and 4 km, in the BRD and GSL regions. Available thermal energy is determined from the general expression:

$$\Delta Q = mc\Delta T, \quad (18)$$

where the temperature drop of a system, ΔT , is multiplied by its mass, m , and specific heat capacity, c . The general equation was reformed in terms relevant to the thermal potential stored in rock for geothermal use. In the case where all thermal energy is extracted from a mass of rock the equation is rewritten as:

$$\Delta Q = V\rho c(T_i - T_f), \quad (19)$$

where ΔT is replaced by the temperature difference between an unexploited reservoir, T_i , and that of a reservoir completely depleted of useful thermal potential, T_f , which is assumed to be 50 °C [Tester et al., 2006]. The mass term is replaced by volume-density, $2.55 \times 10^{12} \text{ m}^3 \cdot \text{kgm}^{-3}$ and the specific heat capacity of rock is approximated to be $10^3 \text{ J}^{-1} \text{ kg}^{-1} \text{ } ^\circ\text{C}$, yielding total geothermal potential.

Along the BRD cross-section, the thermal energy content of rock between 3 km and 4 km ranged from 0.14 EJkm^{-3} to 0.49 EJkm^{-3} , with a mean value 0.31 EJkm^{-3} . For the GSL region cross-section, heat content over the same interval was determined to be between 0.33 EJkm^{-3} and 0.39 EJkm^{-3} with a mean 0.37 EJkm^{-3} . The depth to 150 °C in

the GSL region is generally less than 3 km across the basin and the thermal gradient is relatively constant between 3 km and 4 km. The narrow range of heat content is a reflection of this.

In order for a region to be considered geothermally prospective in this study, temperatures greater than 150 °C must be identified above 4 km depth. The extent of temperatures exceeding 150 °C at or above 4 km was mapped (Figure 24) from cross sections to delineate the lateral extent of geothermal resource in the BRD and GSL regions. The total area in BRD where this criterion was met was approximately 560 km². Temperatures greater than 150 °C at the target depths were generally not found beyond 12 km of the Pavant Butte 1 well and did not occur at all outside of a 20 km radius. The total area in GSL containing 150 °C resource covered approximately 4100 km² that approximately coincide with the bounds of the Great Salt Lake.

Uncertainties in the temperature field were captured quantitatively by evaluating parameter sensitivity on the modeled temperature fields using a Monte Carlo analysis. Five parameters—surface temperature, surface heat flow, thermal conductivity, porosity, and constraining unit thickness—were tested individually to evaluate their impact on the calculated temperature field at nine locations in the project area. The nine locations were selected in basins throughout the state of Utah to compare the uncertainties spatially as well.

One-dimensional temperature fields were calculated using the thermal resistance method, as in equation (12), and holding all but a single parameter constant. Four

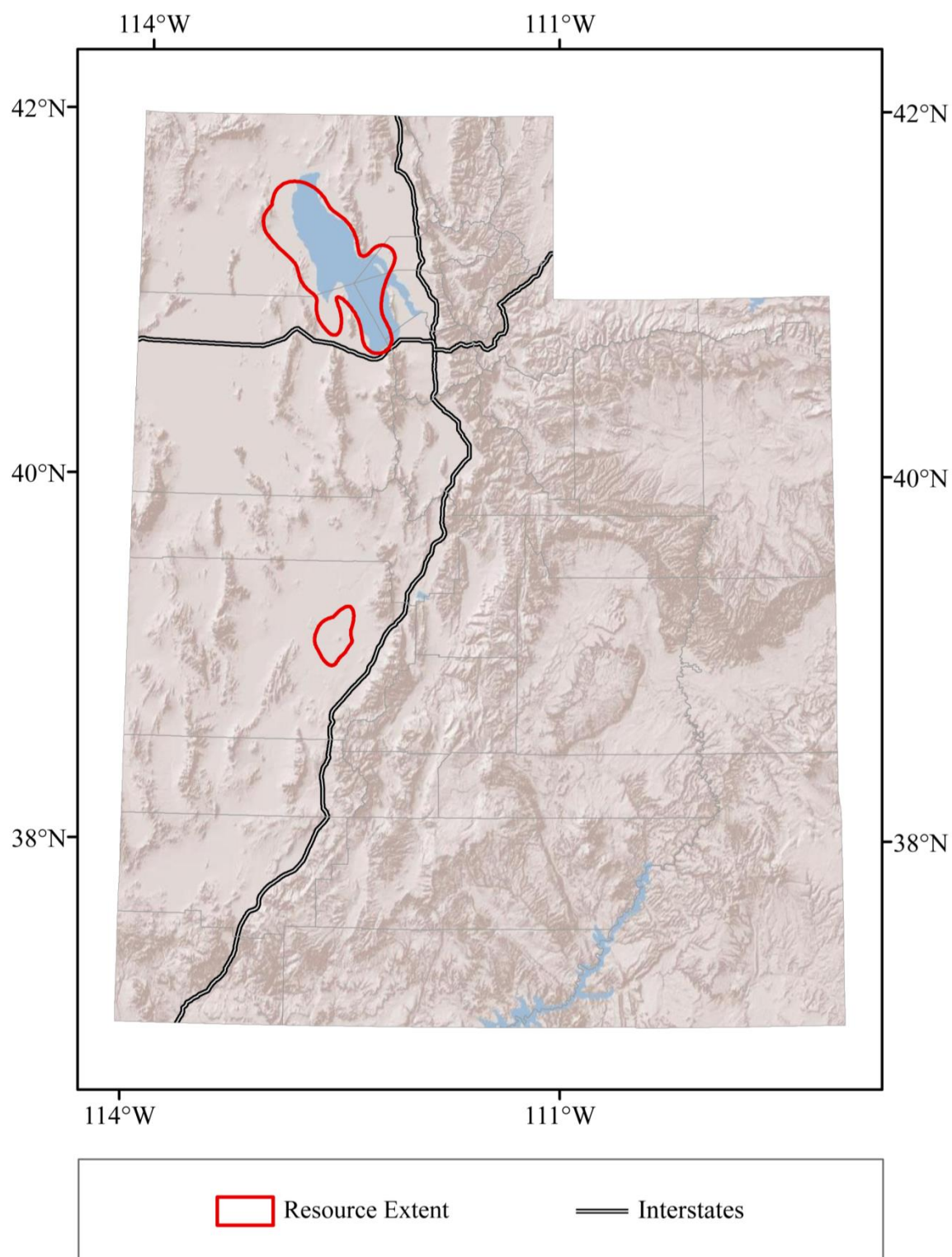


Figure 24. Extent of geothermal resource identified in GSL and BRD regions.

parameters—surface temperature, surface heat flow, thermal conductivity, and porosity—were tested through two standard deviations of their mean. For the fifth parameter, unit thickness, there was not a good quantitative estimate of the potential error, so thickness was varied by $\pm 20\%$ at each location. Each parameter was randomly tested, sampled through 20,000 iterations, and temperatures were recorded at 1 km, 3 km, and 5 km depth.

For interpretation, results of the analysis were displayed graphically in a modification to the tornado plot [Project Management Institute, 2013]. Tornado plots have classically been used to test parameter sensitivities in a deterministic model. The plot highlights minimum and maximum possible deviation from the model baseline, due to perturbations on a single parameter. While identifying the limit of a parameter's possible effect is useful, the traditional tornado plot fails to represent all aspects of parameter sensitivity. For instance, tornado plots do not indicate how perturbations to a parameter affect the shape of the resulting model's probability density function or even where the median outcome occurs relative to the baseline. To remedy the graphical deficiency of a traditional tornado plot, the stacked bars were replaced by normalized probability density functions for each parameter, giving the appearance of a third graphical dimension and providing the ability to represent distributions of modeled outcomes. Additionally, overlaying tornado plots of each parameter at multiple depths for a given location provides a view into how errors propagate to depth.

The error analysis, and resulting tornado plots, provided interesting insights into the impact of the model parameters. These insights were considered and are offered as recommendations to focusing the efforts of future thermal modeling in sedimentary

basins. Two parameters were not particularly influential on temperature at depth—surface temperature and stratigraphic unit thickness. The minimal sensitivity of in-situ temperature to that of the surface is expected since the model treats surface temperature as a static shift and surface temperature is already well constrained. Also, the analysis illustrated that stratigraphic unit thickness did not contribute an appreciable amount of error to the modeled temperature. This is a surprising result as both porosity and thermal conductivity differ throughout the stratigraphic section and each can vary by a large amount. Because no robust estimate of the possible spread of stratigraphic unit thickness was established, it is possible that the sensitivity analysis did not test a broad enough range of thicknesses. Additionally, considering that the shallowest units, UBF and LBF were commonly deeper than 3 km temperature records taken at 1 km and 3 km would be unaffected by a change in thickness that only shifted deeper constraining surfaces. Given a more detailed geologic model, the influence of variations in stratigraphic thickness would be much greater. The model was consistently most sensitive to three parameters: thermal conductivity, porosity, and heat flow. The model became more sensitive to all three parameters at greater depths. This highlights the significance of constraining porosity and thermal conductivity in the shallow stratigraphic section, which is most important to predicting accurately the thermal regime at greater depths of interest. Scrutiny of the distributions of the more sensitive parameters yields useful information as well. Heat flow remains distributed symmetrically about the baseline, whereas porosity and thermal conductivity do not. This asymmetry reveals that overpredicting porosity or underpredicting conductivity will skew the model away from the baseline toward overpredictions. An example of the study's modified tornado plot is shown in Figure 25.

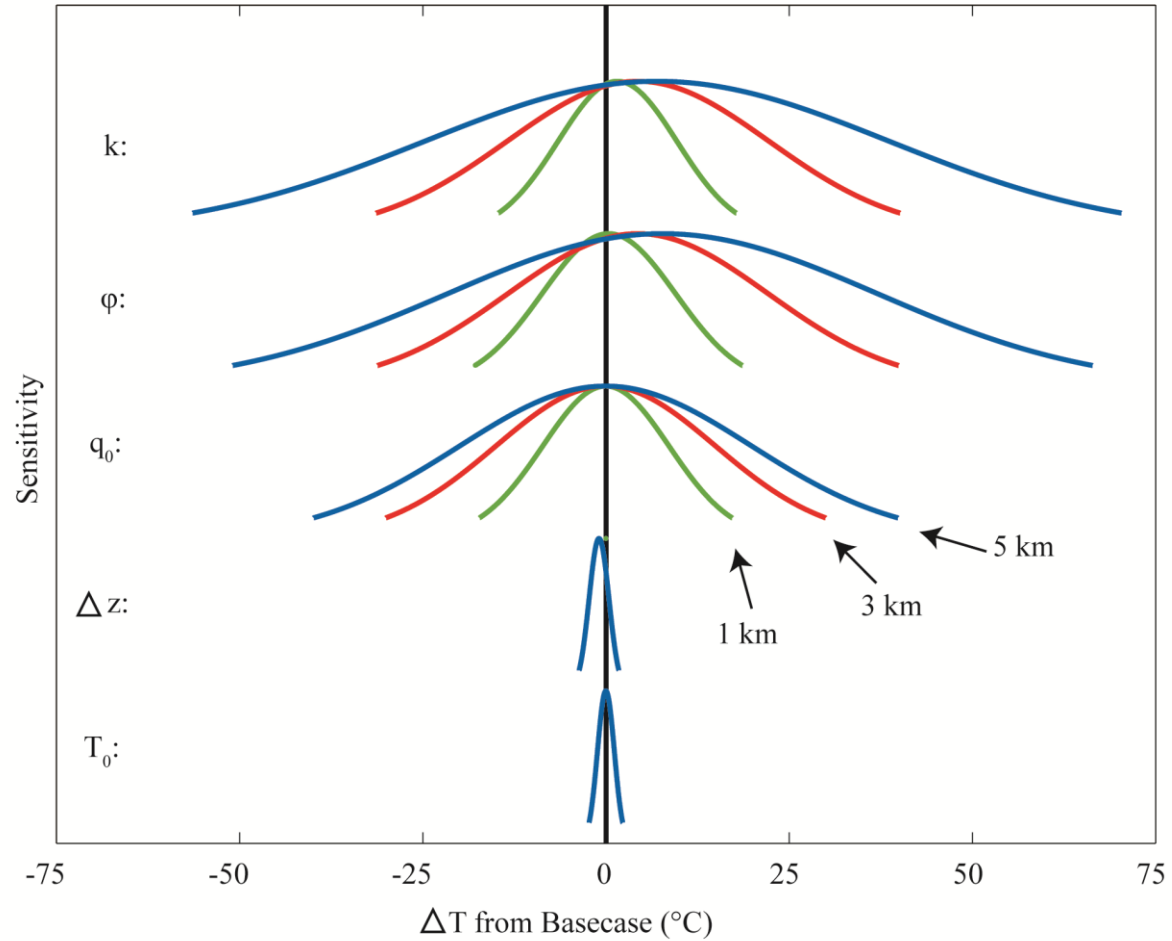


Figure 25. Model sensitivities. The five parameters are assessed at depths of 1 km (green) 3 km (red) and 5 km (blue) for four locations throughout the Basin and Range. The modified tornado plots show sensitivities to each of five parameters varied randomly up to two standard deviations of their mean. The result is a distribution of deviation from the modeled baseline resulting from perturbations to each parameter.

In addition to the sensitivity evaluation, the misfit between the modeled temperature field and BHTs was assessed. One-dimensional temperature fields were calculated at 78 wells in the Basin and Range and compared to their Horner corrected BHTs. Residuals between the calculated field and corrected BHTs revealed that the model overpredicts BHTs by 10 °C and the maximum residual was determined to be 87 °C. The differences are quite large, which likely reflects the noise inherent to the BHT dataset being compounded with model uncertainties. A distribution of all residuals is shown in Figure 26.

The uncertainty analysis provides two takeaway points: first, the most important factors in the calculation of temperature at depth for a conductive regime are thermal conductivity, porosity, and heat flow; second, errors associated with these parameters increase with depth.

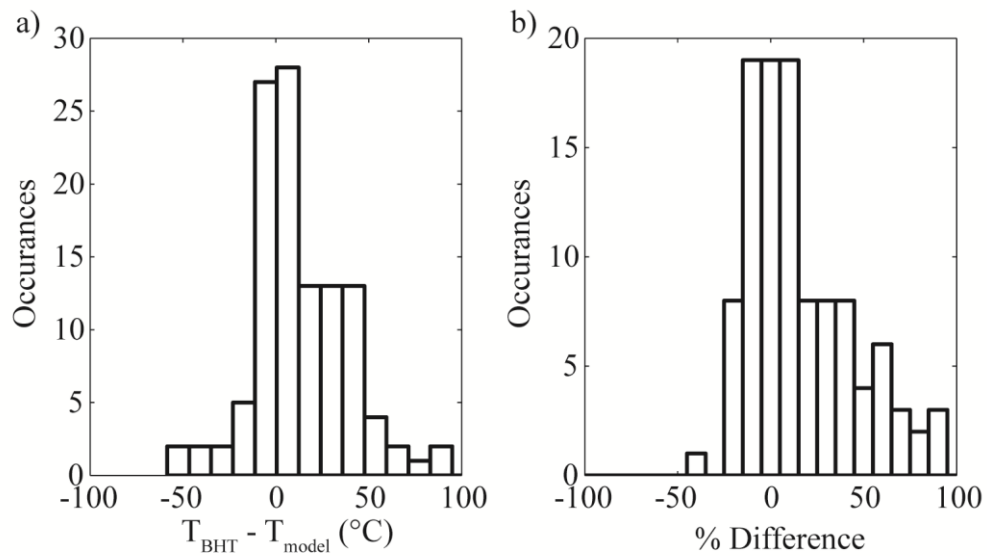


Figure 26. Differences between modeled and observed temperature. The differences were calculated for all wells with corrected BHTs in the Basin and Range. a) Absolute residuals are mean centered about 10 $^{\circ}\text{C}$ skewed toward underpredictions by the model. b) Absolute percent errors between the model and BHTs present a more representative depiction of misfit across all depths.

CONCLUSIONS AND RECOMMENDATIONS

Conclusions

A geothermal resource assessment of the Basin and Range Province in western Utah was carried out to identify resource potential for future exploration and exploitation. The assessment involved several sequential tasks that provide for the following summary observations and conclusions.

1. A rigorous, methodological architecture was developed for calculating regional and local subsurface temperature fields and identifying areas with temperatures above 150 °C at depths shallower than 4 km. The architecture involves assigning surface ground temperature, thermal conductivity, and heat flow throughout the state of Utah and using these data as the basis for calculating temperatures.

2. A surface ground temperature function was developed based on the decrease of temperature with elevation (known as the adiabatic lapse rate), the decrease of temperature with an increase of latitude that results from lessening exposure to solar energy input, and a constant offset between air and ground temperature. Use of weather station data and extrapolation of borehole temperatures yielded the following coefficients for the surface ground temperature function: $-6.42\text{ }^{\circ}\text{Ckm}^{-1}$ for an elevation lapse rate, $-0.0084\text{ }^{\circ}\text{Ckm}^{-1}$ for the latitudinal cooling, and $3\text{ }^{\circ}\text{C}$ to accommodate ground temperatures being warmer than air temperatures.

3. All published thermal conductivity measurements for Utah rock samples were

combined with 468 new measurements to create a comprehensive compilation of more than 2300 thermal conductivity measurements that were applied to characteristic Utah geologic stratigraphic sections. Because thermal conductivity of porous rocks involve thermal conductivity of both matrix and fluid that are combined using an appropriate mixing model and porosity, porosity-depth trends for dominant formations also were determined.

4. A new heat flow map for Utah was created based on approximately 150 classic heat-flow determinations in shallow boreholes with high-precision temperature logs, and 300 oil and gas exploration wells with less precise bottom hole temperatures, but taken at much greater depths. Heat flow for the Basin and Range is 89 mWm^{-2} , 40% higher than the 63 mWm^{-2} value for the Colorado Plateau. A geostatistical kriging algorithm was judged to be best for interpolating the irregularly positioned heat-flow determinations.

5. Calculating temperature with depth, the ultimate goal of this study, required a three-dimensional configuration for thermal conductivity over all regions of interest. We were able to use a recent USGS result giving spatial variation and thicknesses of nine hydrostratigraphic units throughout the study area. When combined with porosity information, the HGU thermal conductivity structure, with surface temperature and heat flow maps, afforded the first opportunity to calculate temperature-depth profiles for any Utah Basin and Range site of interest.

6. Two cross-sections of the resulting temperature fields were chosen to illustrate geothermal potential. The first, in Utah's Black Rock Desert, examined what appeared to be the highest background heat flow ($>130 \text{ mWm}^{-2}$) in the state. In Black Rock Desert, 150°C was encountered at depths generally greater than 3 km and the thermal potential

of rock between 3 km and 4 km for exploitation ranged between 0.14 EJkm^{-3} and 0.49 EJkm^{-3} , with a mean value 0.34 EJkm^{-3} . Total heat contained in the rock between 3 and 4 km depth in the Black Rock Desert thermal anomaly is 190 EJ; if this heat were used for geothermal energy production at a heat sweep efficiency of 10 % and developed over 30 years, the geothermal power potential would be 1,900 MW. For the second thermal anomaly examined, along the axis of the Great Salt Lake, heat flow is generally greater than 105 mWm^{-2} , the depth to 150°C is less than 3 km across the basin, the calculated thermal potential in the 3 km to 4 km depth interval, is between 0.33 EJkm^{-3} and 0.40 EJkm^{-3} with a mean 0.37 EJkm^{-3} . Because of the larger area of the Great Salt Lake thermal anomaly compared to the Black Rock Desert, the total heat energy in rocks between 3 and 4 km depth is 1517 EJ and the corresponding geothermal power potential is 16,000 MW. Proximity to population centers and power transmission and transportation corridors also favor the exploitation of these potential resources.

Recommendations

1. High heat flows reported in the Black Rock Desert are encouraging indicators of the region's geothermal potential; however, more complicated geology and the presence of young cooling volcanics and intrusives appears to be inflating heat flow determinations, ultimately exaggerating modeled estimates of regional scale temperatures through basin sediments. In the Great Salt Lake Region, the combination of elevated heat flow, low conductivity sediments, and depth to basement result in temperatures and thermal potential that flag the region as a priority for geothermal exploration.

2. The most sensitive model parameters should be better constrained. Total rock

pore space and thermal conductivity of the rock matrix have been measured extensively in the Quaternary and Tertiary sections; however, the broadly inclusive stratigraphic groupings of the hydrogeologic units don't allow enough vertical stratification to take full advantage of these detailed thermal conductivity measurements. For regional work, mean values of the HGU thermal conductivity and generalized porosity compaction trends are sufficient to identify the presence of geothermal resource at a basin scale, they are not sufficient, however, to delineate resource to the field scale. A better resolved stratigraphic model should be constructed to provide a more detailed framework for property modeling. Conductivity and porosity were identified to be key parameters for temperature model in a conductive thermal regime and both could be better constrained given a more detailed framework.

3. Rock properties necessary to identify productive reservoirs should be modeled.

When exploring for the presence of geothermal resource, this study gave no consideration to the complications associated with exploiting reservoir fluids, namely flow properties of the rock. Modeled total porosity indicates that significant pore space is present and potentially occupied by high temperature fluids; nevertheless, the question remains, can fluids be moved and can flow be predicted reliably? Again, a more resolved geological model is necessary to evaluate the ability of GSL region basin sediments to host productive reservoirs. This model should assess petrophysical parameters such as effective porosity and permeability.

4. Advective heat transport should be incorporated into the thermal model. For the sake of simplicity, the thermal model used in this study actively avoided thermal data influenced by fluid flow; however, advective heat transport plays a large role in the

thermal state of sedimentary basins. A more inclusive model would incorporate the coupled effect of heat and fluid flow at both the basin and reservoir scales.

5. Elements significant to petroleum systems—such as containers and seals—need to be considered in the context of sedimentary basin geothermal exploitation. The engineering challenge of producing and injecting to petroleum reservoirs in sedimentary basins requires an understanding of reservoir geometries and extent. Presumably, to sustainably produce geothermal reservoirs contained in sedimentary basins the quality and extent of their containment needs to be determined.

6. The thermal regime of two basins in Utah's Basin and Range has been considered using new digital infrastructure, a synthesis of new as well as pre-existing thermal data, and a new paradigm for geothermal exploration. Temperatures between 150 °C and 200 °C, and thermal energy density between 0.33 EJkm^{-3} and 0.39 EJkm^{-3} , at depths of 2.5 km to 4.5 km were identified over broad areas in the Great Salt Lake region. These results provide the impetus for an interdisciplinary project near Utah's Great Salt Lake with the goal to delineate the resource at a field scale, establish the engineering challenges to producing that resource, and assess the potential economic benefit of developing a geothermal exploitation program.

APPENDIX A

Table A1. Existing Thermal Conductivity Measurements of Utah Rock*

Formation	Thermal Conductivity ¹ (W m ⁻² K ⁻²)			n Samples	Lithology	Reference
		σ				
Ankareh	3.23	0.25	15	Sandstone		Deming and Chapman 1988 ²
Aspen	2.56	0.06	17	Shale		Deming and Chapman 1988 ²
Bear River	2.98	0.09	20			Deming and Chapman 1988 ²
Carmel	2.83	0.71	8	Mudstone, Sandstone		Powell 1997 ²
Carmel	2.88	0.58	17	Gypsum-Limestone		Bodell and Chapman 1982 ³
Carmel	2.6	0.38	6	Mudstone		Bodell and Chapman 1982 ³
Carmel	3.37	0.5	7	Siltstone-Sandstone		Bodell and Chapman 1982 ³
Carmel	1.38		1	Gypsum		Bodell and Chapman 1982 ³
Carmel	3.03	0.09	3	Limestone		Bodell and Chapman 1982 ³
Chinle	4.71	1.3	8	Siltstone-Conglomerate		Bodell and Chapman 1982 ³
Chinle	3.44	0.21	2	Siltstone		Bodell and Chapman 1982 ³
Chinle	4.96	0.51	3	Sandstone		Bodell and Chapman 1982 ³
Chinle	7.14	0.41	2	Very Coarse Sandstone		Bodell and Chapman 1982 ³
Chinle	2.47		1	Conglomerate		Bodell and Chapman 1982 ³
Chinle, Shinarump	7.26	0.97	4	Coarse Sandstone		Powell 1997 ²
Claron	3.68	0.2	29	Limestone		Powell 1997 ²
Claron	3.9	0.22	10	Silty Limestone		Powell 1997 ²
Coconino	4.82		1	Sandstone		Powell 1997 ²
Coconino	7.55	0.36	5	Sandstone		Bodell and Chapman 1982 ³

Table A1: Continued

Formation	Thermal		σ	n Samples	Lithology	Reference
	Conductivity ¹ (Wm ⁻² K ⁻²)					
Curtis	4.08		0.51	4	Conglomerate	Bodell and Chapman 1982 ³
Cutler-Rico	3.36		0.5	15	Sandstone-Limestone	Bodell and Chapman 1982 ³
Cutler-Rico	4.02		0.41	6	Silty Sandstone	Bodell and Chapman 1982 ³
Cutler-Rico	3.03		0.41	7	Arkose Sandstone	Bodell and Chapman 1982 ³
Cutler-Rico	3.1		0.22	2	Limestone	Bodell and Chapman 1982 ³
Dakota	6.38			1	Sandstone	Bodell and Chapman 1982 ³
Duchesne	4.80		1.3	51	Sandstone	Chapman et al. 1984 ²
Echo Canyon	6.43		0.65	21	Sandstone-Conglomerate	Deming and Chapman 1988 ²
Elephant Canyon	5.27		0.63	7	Dolomite-Sandstone	Bodell and Chapman 1982 ³
Elephant Canyon	5.39		0.42	4	Dolomite	Bodell and Chapman 1982 ³
Elephant Canyon	5.06		0.81	3	Siltstone-Sandstone	Bodell and Chapman 1982 ³
Entrada	4.77		0.74	2	Sandstone	Powell 1997 ²
Entrada	3.86		0.67	19	Siltstone-Sandstone	Bodell and Chapman 1982 ³
Entrada	3.17		0.43	10	Siltstone	Bodell and Chapman 1982 ³
Entrada	4.58		0.61	9	Sandstone	Bodell and Chapman 1982 ³
Ferron	4.22			1	Sandstone	Bodell and Chapman 1982 ³
Frontier	2.47		0.67	42	Sandstone-Shale	Deming and Chapman 1988 ²
Gannett	3.47		0.19	45	Limestone-Conglomerate	Deming and Chapman 1988 ²
Green River	3.05		0.85	352	Shale	Chapman et al. 1984 ²

Table A1: Continued

Formation	Thermal Conductivity ¹ (Wm ⁻² K ⁻²)		n Samples	Lithology	Reference
	σ				
Guilmette	2.73	0.35	9	Limestone	Henrickson 2000 ⁴
Hermit	2.66	0.13	2	Siltstone	Powell 1997 ²
Hermosa	1.63	0.14	9	Shale	Henrickson 2000 ⁴
Hermosa	4.78	0.08	5	Sandstone	Henrickson 2000 ⁴
Honaker trail	3.25	0.64	10	Mudstone-Sandstone, Limestone	Bodell and Chapman 1982 ³
Honaker trail	2.46	0.32	2	Mudstone	Bodell and Chapman 1982 ³
Honaker trail	3.99	0.2	4	Sandstone	Bodell and Chapman 1982 ³
Honaker trail	2.91	0.09	4	Limestone	Bodell and Chapman 1982 ³
Jordanelle Stock	2.10				Moran 1991 ⁵
Kaibab	3.3	0.31	2	Limestone	Powell 1997 ²
Kayenta	5.55	0.54	14	Silty Sandstone-Sandstone	Bodell and Chapman 1982 ³
Kayenta	4.68	0.3	5	Silty Sandstone	Bodell and Chapman 1982 ³
Kayenta	6	0.29	9	Sandstone	Bodell and Chapman 1982 ³
Kelvin	3.61	0.70	128	Shaley Sandstone	Deming and Chapman 1988 ²
Madison	4.3	0.28	20	Limestone	Deming and Chapman 1988 ²
Mancos	2.48	0.24	24	Shale	Henrickson 2000 ⁴
Mesaverde	2.80	0.5	79	Shaley Sandstone	Chapman et al. 1984 ²
Moenkopi	2.65	0.24	21	Mudstone	Powell 1997 ²
Morrison	2.74		1	Limestone	Bodell and Chapman 1982 ³

Table A1: Continued

Formation	Thermal		σ	n Samples	Lithology	Reference
	Conductivity ¹ (Wm ⁻² K ⁻²)					
Navajo	6.91	0.51	17	Sandstone		Powell 1997 ²
Navajo	5.42	0.72	24	Silty Sandstone-Sandstone		Bodell and Chapman 1982 ³
Navajo	4.16	0.42	5	Silty Sandstone		Bodell and Chapman 1982 ³
Navajo	5.79	0.66	19	Sandstone		Bodell and Chapman 1982 ³
Nugget	6.13	0.22	14	Sandstone		Deming and Chapman 1988 ²
Nugget	3.73	0.66	24	Silty-Sandstone		Deming and Chapman 1988 ²
pC	3.67	0.34	9	Gneiss		Powell 1997 ²
Phosphoria	4.81	0.17	16			Deming and Chapman 1988 ²
Pruess	3.33	0.12	43			Deming and Chapman 1988 ²
Qal	3.00					Moran 1991 ⁵
Qb	1.63	0.1	6	Basalt		Powell 1997 ²
Quat Landslide	2.10					Moran 1991 ⁵
Redwall	4.94	0.18	2	Dolomite		Bodell and Chapman 1982 ³
Sevy	6.53		1	Dolomite		Henrickson 2000 ⁴
Simonson	2.98	0.17	9	Limestone		Henrickson 2000 ⁴
Straight Cliffs	3.32	0.52	3	Sandstone		Powell 1997 ²
Stump-Pruess	3.46	0.61	52			Deming and Chapman 1988 ²
Summerville	4.2		1	Siltstone		Bodell and Chapman 1982 ³
Thaynes	4.05	0.13	20			Deming and Chapman 1988 ²

Table A1: Continued

Formation	Thermal Conductivity ¹ (W m ⁻² K ⁻²)		σ	n Samples	Lithology	Reference
Tm v	2.14	0.06	3		Rhyolite Porphyry	Powell 1997 ²
Tm v	1.87	0.15	6		Trachyte Porphyry	Powell 1997 ²
Tm v	2.02	0.16	9		Andesite Porphyry	Powell 1997 ²
Toroweap	3.88	0.16	3		Silty Limestone	Powell 1997 ²
Tropic, Dakota	2.29		2		Silty Claystone	Powell 1997 ²
Twin Creek	2.68	0.35	82			Deming and Chapman 1988 ²
Uinta	3.22	0.5	199			Chapman et al. 1984 ²
Upper Moenkopi	3.37	0.4	18		Mudstone, Siltstone	Powell 1997 ²
Wasatch	2.58	0.37	171			Chapman et al. 1984 ²
Weber	6.03	0.24	20			Deming and Chapman 1988 ²
Weber	4.53				Quartzite	Moran 1991 ⁵
Wingate	5.24	0.37	17		Sandstone	Bodell and Chapman 1982 ³
Woodside	2.35				Shale	Moran 1991 ⁵
Woodside-Dinwoody	3.42	0.05	20			Deming and Chapman 1988 ²

*Thermal conductivities measured in the University of Utah Thermal Lab on Colorado Plateau and Basin and Range rocks.

¹Conductivities listed for cuttings represent matrix thermal conductivity while values listed for core represent whole rock value.

²Conductivities from cuttings measured on the divided bar.

³Conductivities from core measured on the divided bar.

⁴Conductivities from cuttings measured on the divided bar and whole rock measured by TK-04.

⁵Conductivities from cuttings and core measured on the divided bar.

APPENDIX B

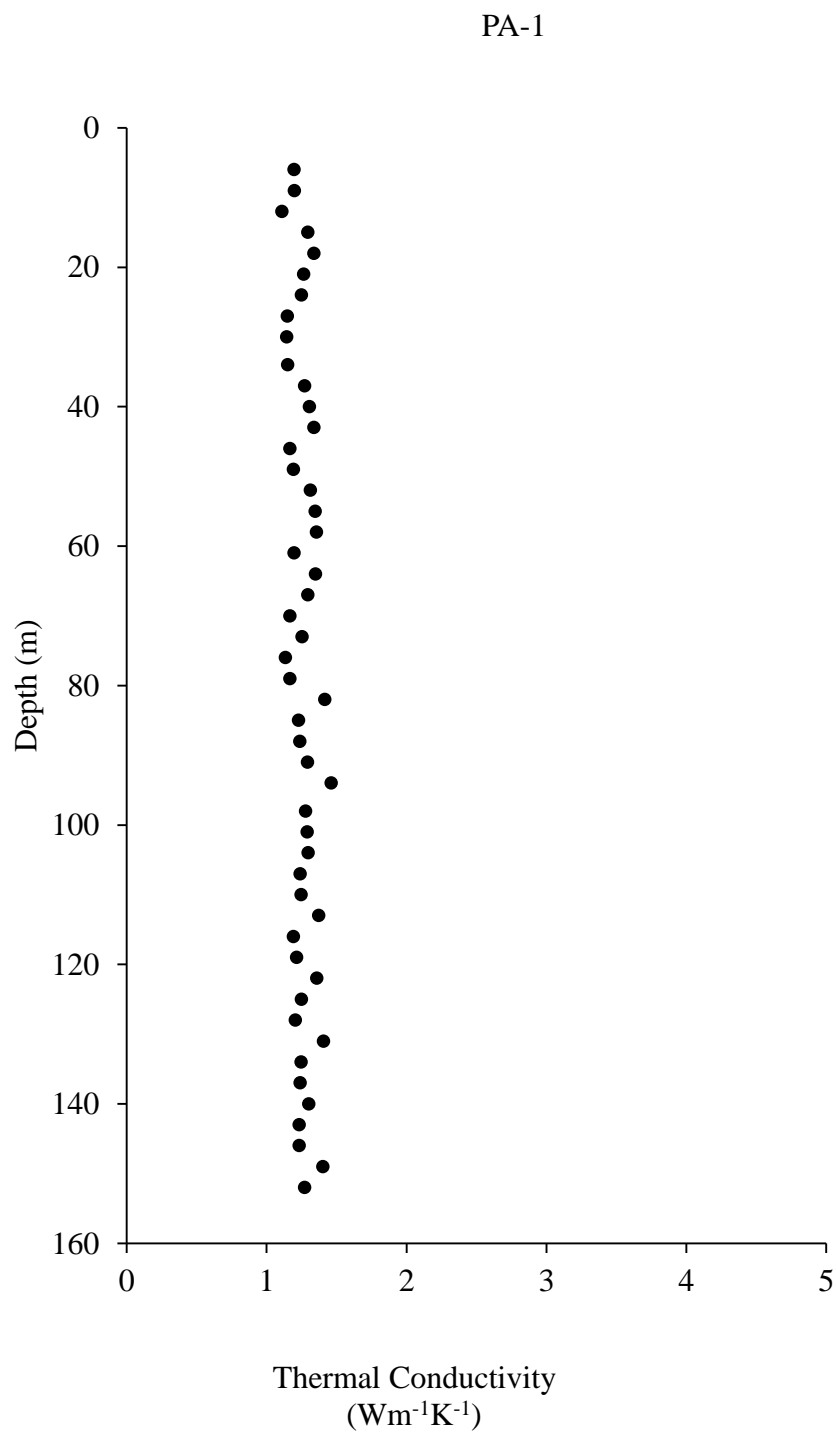


Figure B1. Thermal conductivities from PA-1.

Table B1. Thermal conductivity measurements for PA-1*

Depth (m)	Thermal Conductivity ^w (Wm ⁻¹ K ⁻¹)	Depth (m)	Thermal Conductivity ^w (Wm ⁻¹ K ⁻¹)
6.1	1.20	112.8	1.37
9.1	1.20	115.8	1.19
12.2	1.11	118.9	1.21
15.2	1.29	121.9	1.36
18.3	1.34	125	1.25
21.3	1.27	128	1.21
24.4	1.25	131.1	1.41
27.4	1.15	134.1	1.25
30.5	1.14	137.2	1.24
33.5	1.15	140.2	1.30
36.6	1.27	143.3	1.23
39.6	1.31	146.3	1.23
42.7	1.34	149.4	1.40
45.7	1.17	152.4	1.27
48.8	1.19		
51.8	1.31		
54.9	1.35		
57.9	1.36		
61	1.20		
64	1.35		
67.1	1.30		
70.1	1.17		
73.2	1.25		
76.2	1.13		
79.2	1.17		
82.3	1.42		
85.3	1.23		
88.4	1.24		
91.4	1.29		
94.5	1.46		
97.5	1.28		
100.6	1.29		
103.6	1.30		
106.7	1.24		
109.7	1.25		

*Thermal conductivity measured on divided bar. ^wApproximate whole rock conductivity.

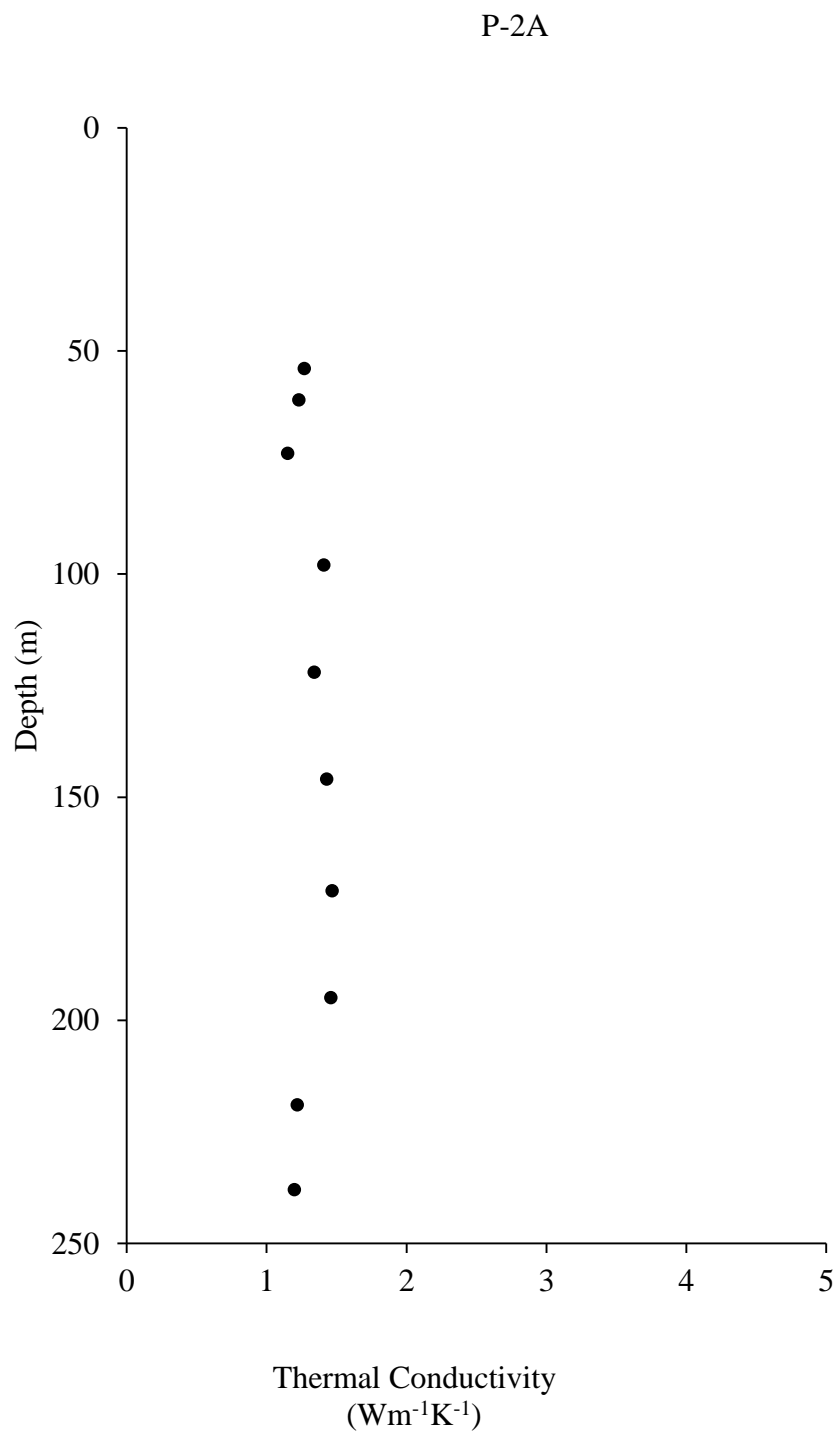


Figure B2. Thermal conductivities from P-2A.

Table B2. Thermal conductivity measurements for P-2A*

Depth (m)	Thermal Conductivity ^w (Wm ⁻¹ K ⁻¹)
54	1.27
61	1.23
73	1.15
98	1.41
122	1.34
146	1.43
171	1.47
195	1.46
219	1.22
238	1.20

*Thermal conductivity measured on divided bar. ^wApproximate whole rock conductivity.

PA-3

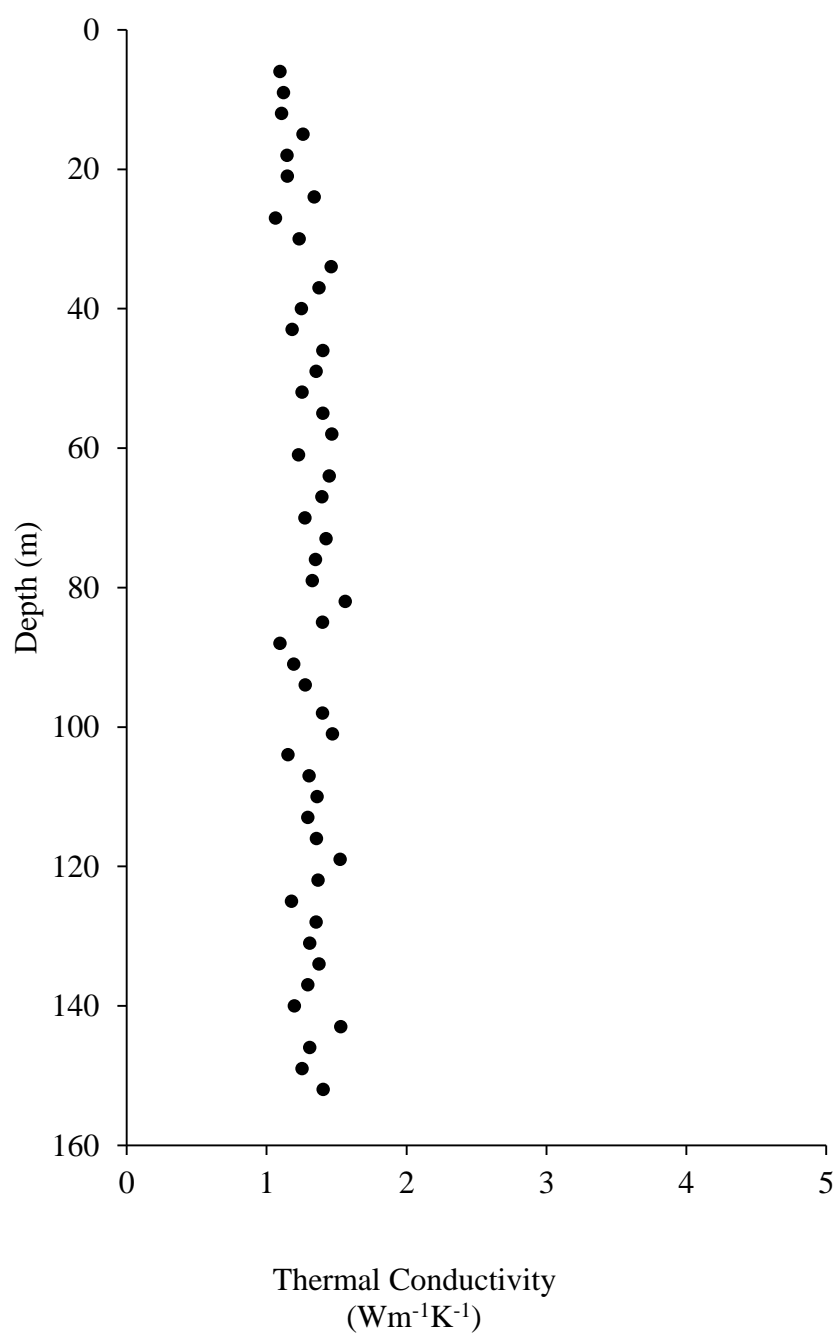


Figure B3. Thermal conductivities from PA-3.

Table B3. Thermal conductivity measurements for PA-3*

Depth (m)	Thermal Conductivity ^w (Wm ⁻¹ K ⁻¹)	Depth (m)	Thermal Conductivity ^w (Wm ⁻¹ K ⁻¹)
6.1	1.10	112.8	1.30
9.1	1.12	115.8	1.36
12.2	1.11	118.9	1.53
15.2	1.26	121.9	1.37
18.3	1.15	125	1.18
21.3	1.15	128	1.35
24.4	1.34	131.1	1.31
27.4	1.06	134.1	1.37
30.5	1.23	137.2	1.30
33.5	1.46	140.2	1.20
36.6	1.37	143.3	1.53
39.6	1.25	146.3	1.31
42.7	1.18	149.4	1.26
45.7	1.40	152.4	1.40
48.8	1.35		
51.8	1.25		
54.9	1.40		
57.9	1.47		
61	1.23		
64	1.45		
67.1	1.40		
70.1	1.27		
73.2	1.42		
76.2	1.35		
79.2	1.33		
82.3	1.56		
85.3	1.40		
88.4	1.10		
91.4	1.19		
94.5	1.28		
97.5	1.40		
100.6	1.47		
103.6	1.15		
106.7	1.30		
109.7	1.36		

*Thermal conductivity measured on divided bar. ^wApproximate whole rock conductivity.

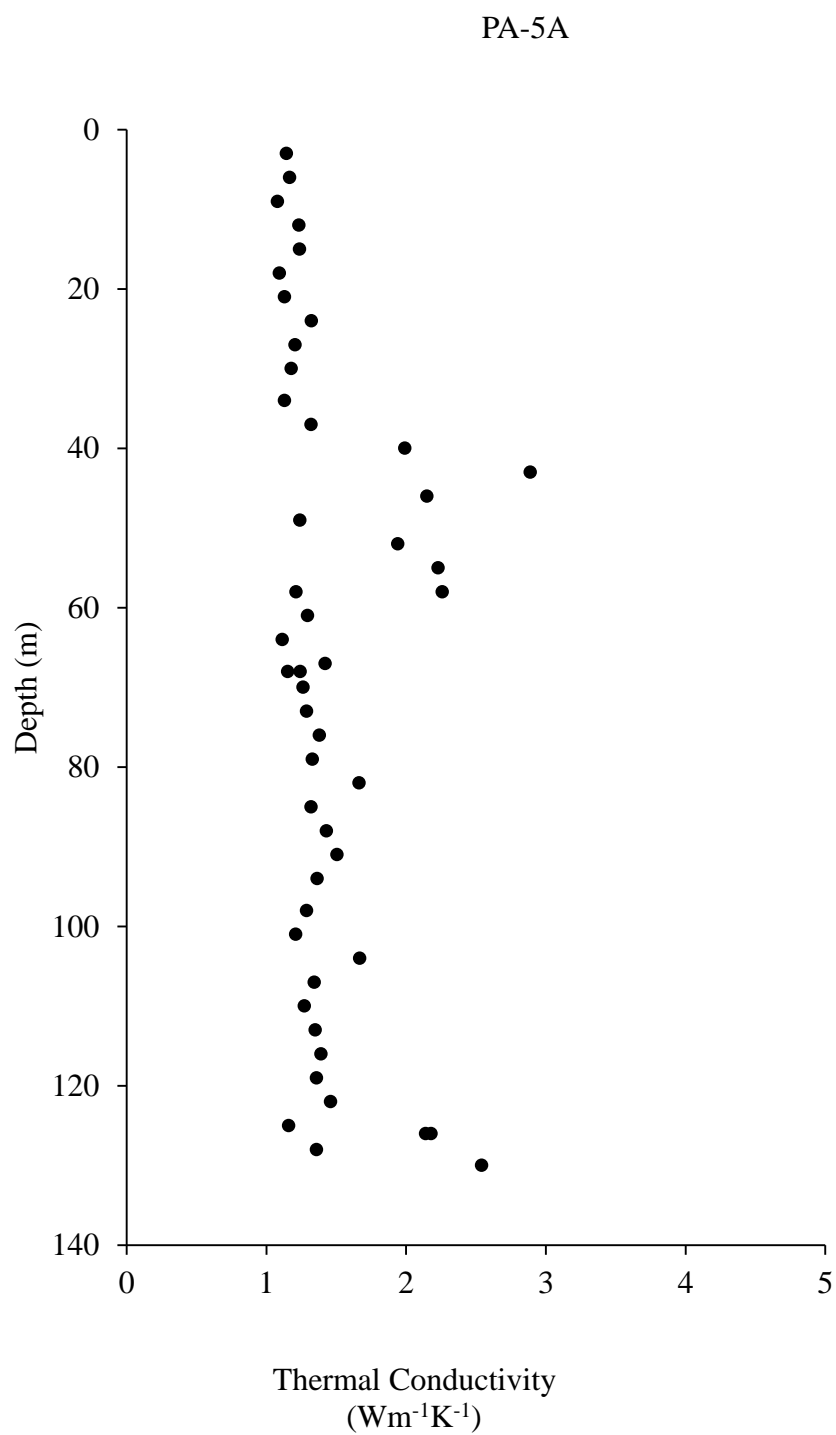


Figure B4. Thermal conductivities from PA-5A.

Table B4. Thermal conductivity measurements for PA-5A*

Depth (m)	Thermal Conductivity (Wm ⁻¹ K ⁻¹)	Depth (m)	Thermal Conductivity (Wm ⁻¹ K ⁻¹)
3	1.14 ^w	100.6	1.21 ^w
6.1	1.17 ^w	103.6	1.67 ^w
9.1	1.08 ^w	106.7	1.34 ^w
12.2	1.23 ^w	109.7	1.27 ^w
15.2	1.24 ^w	112.8	1.35 ^w
18.3	1.09 ^w	115.8	1.39 ^w
21.3	1.13 ^w	118.9	1.36 ^w
24.4	1.32 ^w	121.9	1.46 ^w
27.4	1.21 ^w	125	1.16 ^w
30.5	1.18 ^w	125.6	2.18 ^m
33.5	1.13 ^w	125.6	2.14 ^m
36.6	1.32 ^w	128	1.36 ^w
39.6	1.99 ^m	129.8	2.54 ^m
42.7	2.89 ^m		
45.7	2.15 ^m		
48.8	1.24 ^w		
51.8	1.94 ^m		
54.9	2.23 ^m		
57.9	2.26 ^m		
57.9	1.21 ^w		
61	1.30 ^w		
64	1.11 ^w		
67.1	1.42 ^w		
68	1.24 ^w		
68	1.15 ^w		
70.1	1.26 ^w		
73.2	1.29 ^w		
76.2	1.38 ^w		
79.2	1.33 ^w		
82.3	1.66 ^w		
85.3	1.32 ^w		
88.4	1.43 ^w		
91.4	1.51 ^w		
94.5	1.36 ^w		
97.5	1.29 ^w		

*Thermal conductivity measured on divided bar. ^wApproximate whole rock conductivity.^mMatrix conductivity.

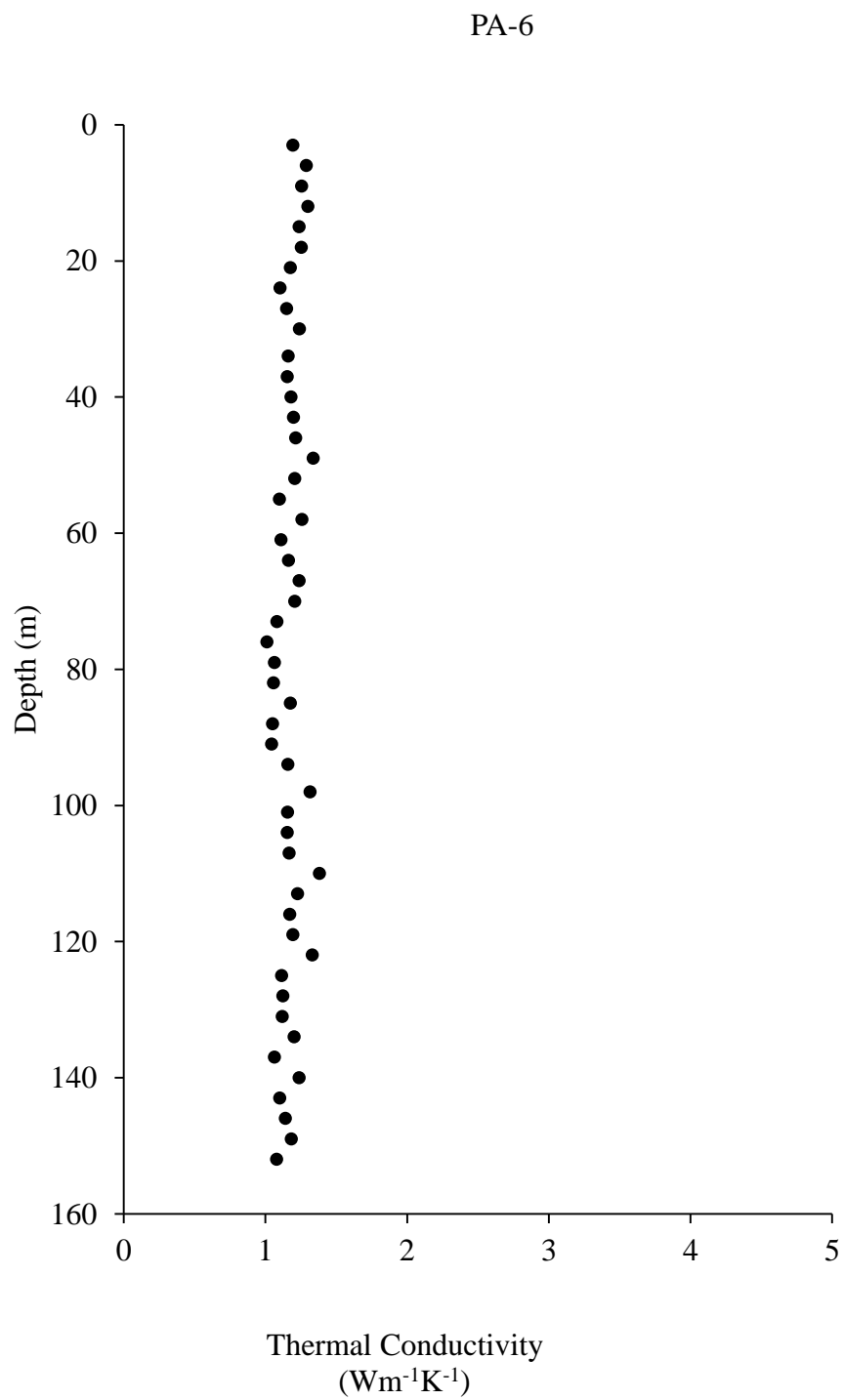


Figure B5. Thermal conductivities from PA-6.

Table B5. Thermal conductivity measurements for PA-6*

Depth (m)	Thermal Conductivity ^w (Wm ⁻¹ K ⁻¹)	Depth (m)	Thermal Conductivity ^w (Wm ⁻¹ K ⁻¹)
3	1.19	109.7	1.38
6.1	1.29	112.8	1.23
9.1	1.26	115.8	1.17
12.2	1.30	118.9	1.20
15.2	1.24	121.9	1.33
18.3	1.25	125	1.11
21.3	1.18	128	1.12
24.4	1.10	131.1	1.12
27.4	1.15	134.1	1.20
30.5	1.24	137.2	1.06
33.5	1.16	140.2	1.24
36.6	1.16	143.3	1.10
39.6	1.18	146.3	1.14
42.7	1.20	149.4	1.18
45.7	1.21	152.4	1.08
48.8	1.34		
51.8	1.21		
54.9	1.10		
57.9	1.26		
61	1.11		
64	1.16		
67.1	1.24		
70.1	1.21		
73.2	1.08		
76.2	1.01		
79.2	1.06		
82.3	1.06		
85.3	1.18		
88.4	1.05		
91.4	1.05		
94.5	1.16		
97.5	1.31		
100.6	1.16		
103.6	1.15		
106.7	1.17		

*Thermal conductivity measured on divided bar. ^wApproximate whole rock conductivity.

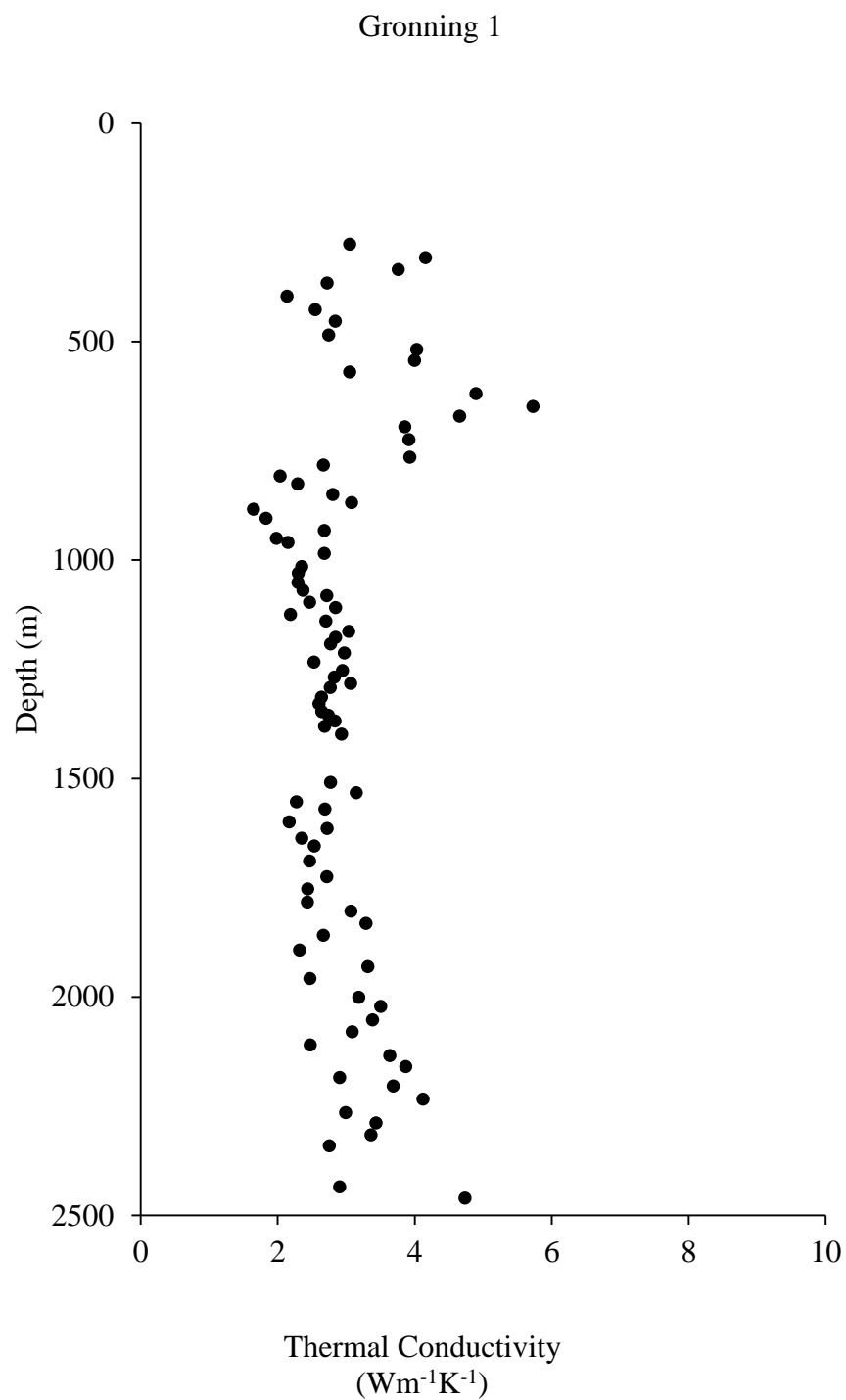


Figure B6. Thermal conductivities from Gronning 1.

Table B6. Thermal conductivity measurements for Gronning 1*

Depth (m)	Thermal Conductivity ^m (Wm ⁻¹ K ⁻¹)	Depth (m)	Thermal Conductivity ^m (Wm ⁻¹ K ⁻¹)	Depth (m)	Thermal Conductivity ^m (Wm ⁻¹ K ⁻¹)
277	3.05	1125	2.19	1958	2.47
308	4.16	1140	2.70	2001	3.18
335	3.76	1164	3.04	2022	3.51
366	2.73	1177	2.85	2053	3.39
396	2.14	1192	2.77	2080	3.09
427	2.55	1213	2.98	2110	2.48
454	2.84	1234	2.53	2135	3.64
485	2.75	1253	2.95	2160	3.87
518	4.03	1268	2.83	2185	2.91
543	4.00	1283	3.07	2204	3.69
570	3.05	1292	2.77	2234	4.12
619	4.90	1314	2.64	2265	2.99
649	5.73	1329	2.60	2289	3.44
671	4.66	1347	2.65	2316	3.37
695	3.86	1356	2.74	2341	2.76
725	3.92	1369	2.84	2435	2.90
765	3.93	1381	2.69	2461	4.73
783	2.67	1399	2.93		
808	2.04	1509	2.77		
826	2.29	1533	3.15		
850	2.81	1554	2.28		
869	3.08	1570	2.69		
884	1.65	1600	2.17		
905	1.83	1615	2.73		
933	2.68	1637	2.35		
951	1.98	1655	2.54		
960	2.15	1689	2.47		
985	2.68	1725	2.72		
1015	2.35	1753	2.44		
1030	2.30	1783	2.44		
1052	2.30	1804	3.07		
1070	2.37	1832	3.29		
1082	2.72	1859	2.67		
1097	2.47	1893	2.32		
1109	2.85	1931	3.32		

*Thermal conductivity measured on divided bar. ^mMatrix conductivity.

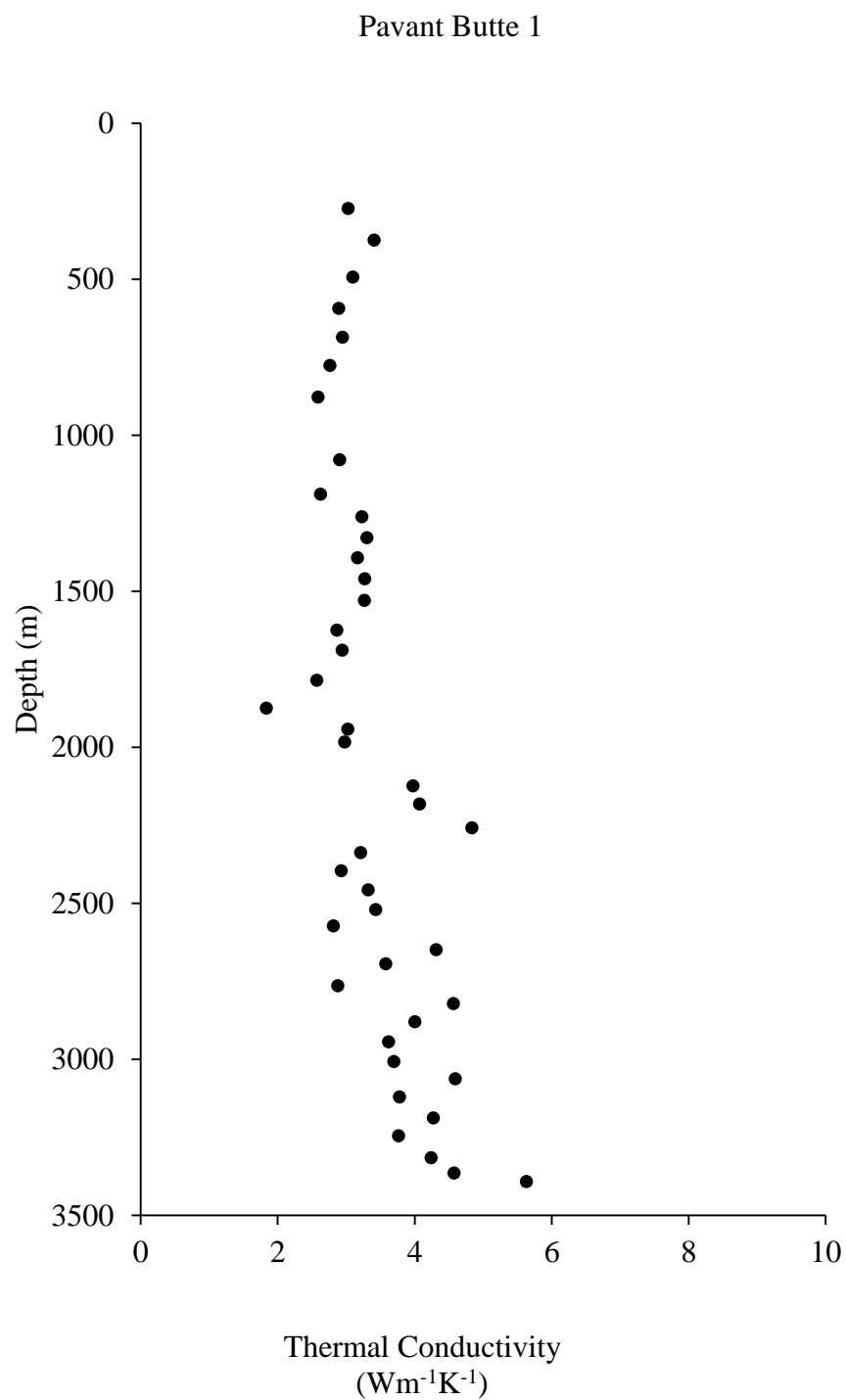


Figure B7. Thermal conductivities from Pavant Butte 1.

Table B7. Thermal conductivity measurements for Pavant Butte 1*

Depth (m)	Thermal Conductivity ^m (Wm ⁻¹ K ⁻¹)	Depth (m)	Thermal Conductivity ^m (Wm ⁻¹ K ⁻¹)
274	3.03	3063	4.59
375	3.41	3121	3.78
494	3.10	3188	4.27
594	2.89	3246	3.77
686	2.95	3316	4.24
777	2.76	3365	4.58
878	2.59	3392	5.63
1079	2.91		
1189	2.63		
1262	3.23		
1329	3.30		
1393	3.17		
1460	3.27		
1530	3.27		
1625	2.87		
1689	2.94		
1786	2.57		
1875	1.84		
1942	3.02		
1984	2.98		
2124	3.98		
2182	4.07		
2259	4.84		
2338	3.21		
2396	2.93		
2457	3.32		
2521	3.43		
2573	2.81		
2649	4.32		
2694	3.58		
2765	2.88		
2822	4.57		
2880	4.00		
2944	3.62		
3008	3.7		

*Thermal conductivity measured on divided bar. ^mMatrix conductivity.

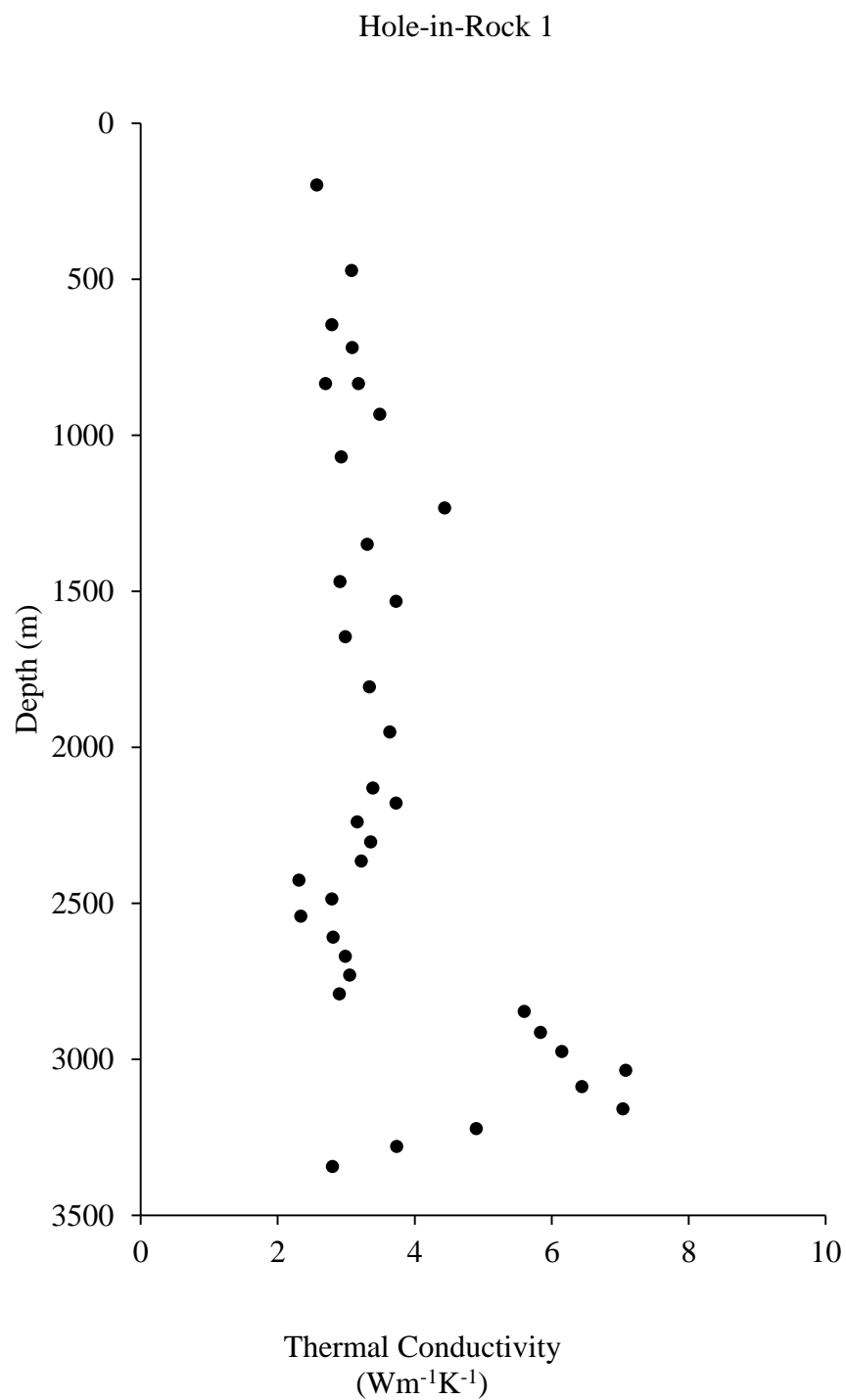


Figure B8. Thermal conductivities from Hole-in-Rock 1.

Table B8. Thermal conductivity measurements for Hole-in-Rock 1*

Depth (m)	Thermal Conductivity ^m (Wm ⁻¹ K ⁻¹)
198	2.57
472	3.08
646	2.79
719	3.09
835	2.70
835	3.18
933	3.49
1070	2.93
1234	4.44
1350	3.31
1469	2.91
1533	3.73
1646	2.99
1807	3.34
1951	3.64
2131	3.39
2179	3.73
2240	3.16
2304	3.36
2365	3.22
2426	2.31
2487	2.79
2542	2.34
2609	2.81
2670	2.99
2731	3.05
2791	2.90
2847	5.60
2914	5.84
2975	6.15
3036	7.08
3088	6.44
3159	7.04
3222	4.90
3280	3.74
3344	2.80

*Thermal conductivity measured on divided bar. ^mMatrix conductivity.

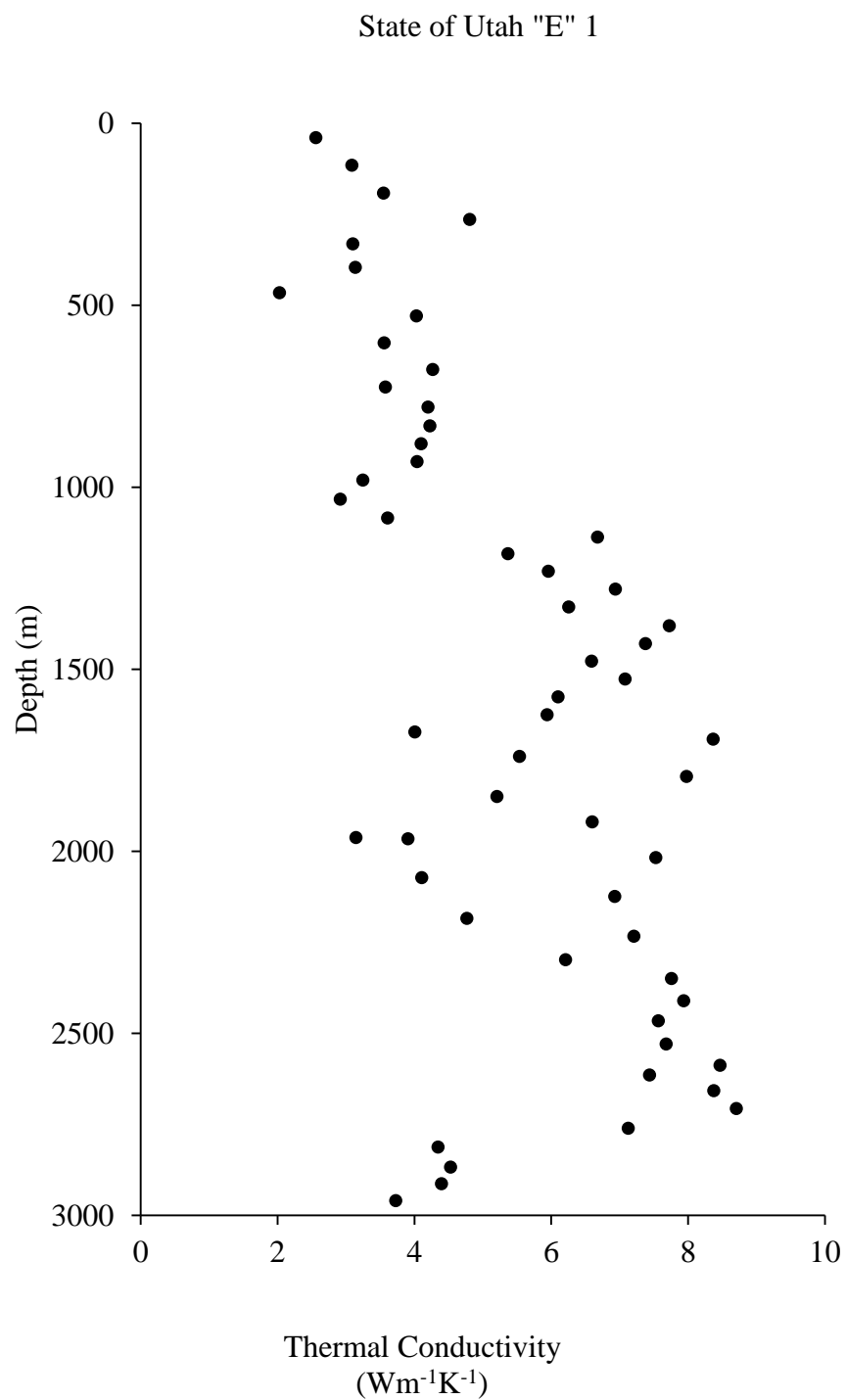


Figure B9. Thermal conductivities from State of Utah “E” 1.

Table B9. Thermal conductivity measurements for State of Utah “E” 1*

Depth (m)	Thermal Conductivity ^m (Wm ⁻¹ K ⁻¹)	Depth (m)	Thermal Conductivity ^m (Wm ⁻¹ K ⁻¹)
40	2.56	1966	3.91
116	3.09	2018	7.53
192	3.55	2073	4.11
265	4.81	2124	6.93
332	3.10	2185	4.77
396	3.14	2234	7.21
466	2.03	2298	6.21
530	4.03	2350	7.76
604	3.56	2411	7.94
677	4.27	2466	7.57
725	3.58	2530	7.68
780	4.20	2588	8.47
832	4.23	2615	7.44
881	4.10	2658	8.38
930	4.04	2707	8.71
981	3.25	2761	7.13
1033	2.92	2813	4.35
1085	3.61	2868	4.53
1137	6.68	2914	4.40
1183	5.37	2960	3.73
1231	5.96		
1280	6.94		
1329	6.26		
1381	7.73		
1430	7.38		
1478	6.59		
1527	7.08		
1576	6.10		
1625	5.94		
1673	4.01		
1692	8.37		
1740	5.54		
1795	7.98		
1850	5.21		
1920	6.60		
1963	3.15		

*Thermal conductivity measured on divided bar. ^mMatrix conductivity.

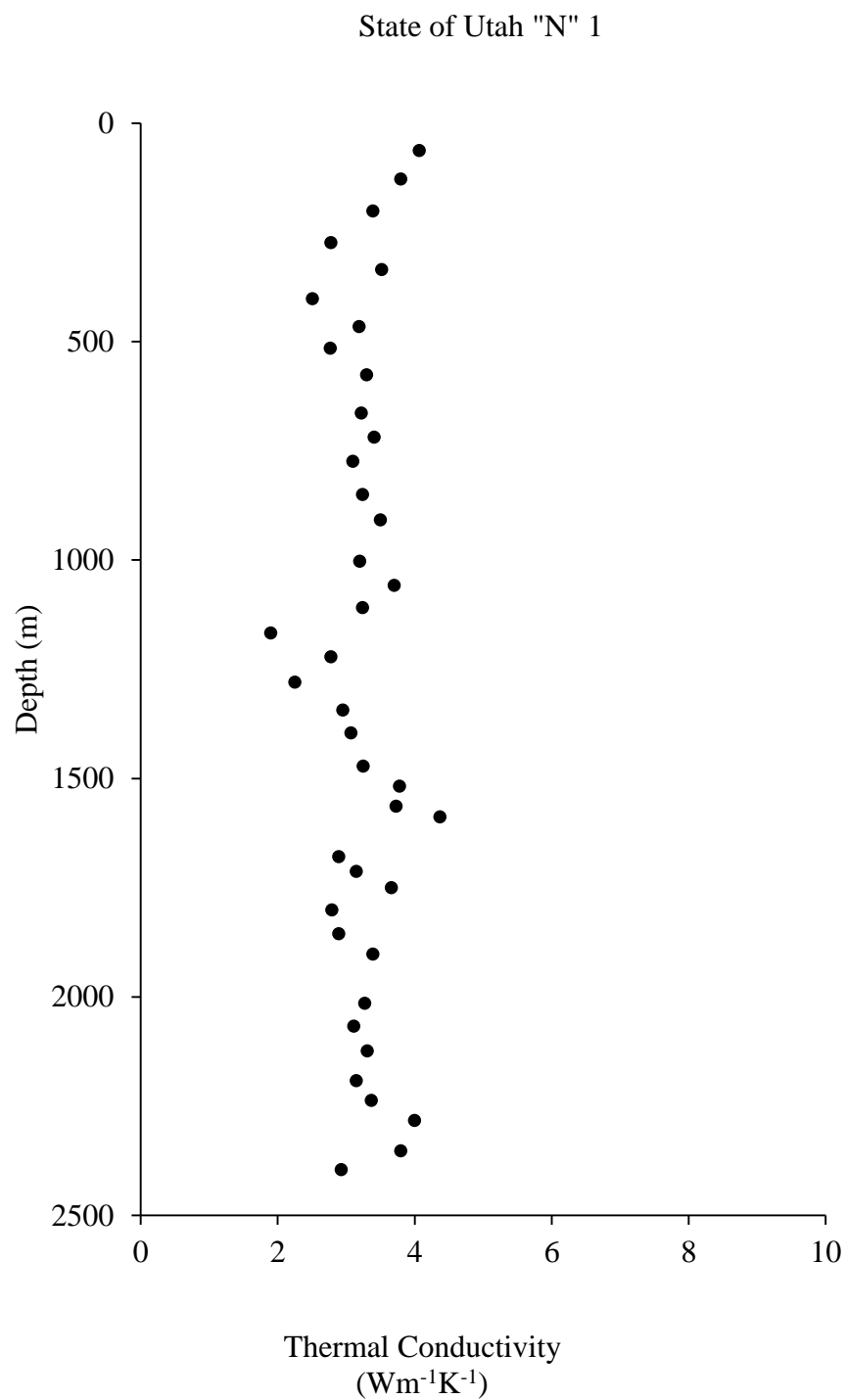


Figure B9. Thermal conductivities from State of Utah “N” 1.

Table B10. Thermal conductivity measurements for State of Utah “N” 1*

Depth (m)	Thermal Conductivity ^m (Wm ⁻¹ K ⁻¹)	Depth (m)	Thermal Conductivity ^m (Wm ⁻¹ K ⁻¹)
63	4.07	2192	3.15
128	3.80	2237	3.37
201	3.39	2283	4.00
274	2.78	2353	3.80
335	3.52	2396	2.93
402	2.51		
466	3.19		
515	2.77		
576	3.30		
664	3.22		
719	3.41		
774	3.10		
850	3.24		
908	3.50		
1003	3.20		
1058	3.70		
1109	3.24		
1167	1.90		
1222	2.78		
1280	2.25		
1344	2.95		
1396	3.07		
1472	3.25		
1518	3.78		
1564	3.73		
1588	4.37		
1679	2.89		
1713	3.15		
1750	3.66		
1801	2.79		
1856	2.89		
1902	3.39		
2015	3.27		
2067	3.11		
2124	3.31		

*Thermal conductivity measured on divided bar. ^mMatrix conductivity.

APPENDIX C

Table C1. Heat flow values generated in this study.

API	Well Name	UTM 12N Easting (m)	UTM 12N Northing (m)	Heat Flow (mWm ⁻²)
00130006	USA 1-25	273507	4257528	92
00330020	State of Utah "R" 1	344964	4585414	119
00530013	Hauser Farms 1-10	422343	4637405	90
01130002	State of Utah "E" 1	386504	4537321	99
01530082	Indian Creek 1	481387	4358277	52
01530175	Indian Creek Unit 021762-3	481039	4357118	48
02730024	Henley 1	378726	4345916	94
02730026	Horse Heaven State 16-21A	280112	4318506	71
02730027	Pavant Butte 1	361374	4331574	145
02730028	Meadow Federal Unit 1	362369	4303663	66
02730035	Sevier Lake Federal 1-29	327825	4333323	63
02730036	Black Rock Federal Unit 1-29	336002	4323849	106
03330035	Champlin 388 Amoco C 1	483556	4564720	44
03530003	Saltair 2	409000	4518913	63
03930006	Moroni 1-A	452032	4373946	61
03930012	Barton 4-2	442334	4348214	49
03930040	Providence Federal 24-4	434292	4322407	62
04130015	Corral Federal 1	462827	4289435	88
04130044	Wolverine Fed. Glenwood 10-1	413207	4286487	90
04130054	Wolverine State 17-10	418900	4294425	94
04130055	Wolverine State 20-3	418903	4294416	97
04130057	Wolverine Federal 20-4	418901	4294420	95
04150002	Crater Peak Federal 13-1	425227	4304508	86
04330024	Weber Coal Company 13-3	468376	4531139	84
04330039	Champlin 387 Amoco A 1	483839	4539338	61
04330052	Champlin 476 Amoco A 1	481482	4554084	58
04330063	UPPR-Gillmore 33-11	480354	4519986	43
04330094	Rockport Reservoir 1	467700	4516385	50
04330119	Champlin 225 B 1	474771	4534593	76
04330124	Texoma-Champlin-Wilde 1-11	470420	4529693	69
04330169	State of Utah "S" 1	482782	4534508	55
04330192	Coalville Gas Storage 8	468353	4529919	91
04330205	Champlin 464 Amoco B 1	470106	4516753	72
04330207	Champlin 550 Amoco A 1	479510	4519577	34
04330208	Champlin 466 B 1	465209	4527690	62
04330236	Moore-Amoco A 1	486167	4537370	42

Table C1: Continued

API	Well Name	UTM 12N Easting (m)	UTM 12N Northing (m)	Heat Flow (mWm ⁻²)
04330256	Richins 1-32-1C	455968	4533554	75
04330263	UPRR 1	476754	4519919	44
04330274	UPRR B 1	462719	4515213	65
04530010	State of Utah "N" 1	389857	4512197	93
05730001	Basin Investment Company 1	403057	4571585	71
-	P-2A	365963	4321704	89
-	PA-2	353958	4356798	83
-	PA-3	358865	4348218	81
-	PA-4	351620	4338792	86
-	PA-6	346622	4312192	82

APPENDIX D

Appendix D contains descriptions of digital deliverables associated with this report. The deliverables consist of the Geographic Information System (GIS) dataset used to generate the project's final heat flow map and the code used to determine temperature in the subsurface. Each is packaged into its own archival file and is included with this report.

The GIS dataset is comprised of three main parts: (1) a rasterized and georeferenced tif image of heat flow across Utah, (2) a point shapefile containing relevant information on the control data used to generate the heat flow map, (3) a complete map with interpolated heat flow and all relevant control as well as culture. The data is all provided in Universal Transverse Mercator (UTM) Zone 12N and is referenced to the North American Datum (NAD) of 1983. Additionally, a 'README' file is included that details key information about file structure and fields.

The archival directory containing code developed in Matlab to determine temperature at depth is comprised of a number of scripts (.m files) and data structures (.mat files). The code is a finite difference scheme discussed in the preceding chapters and requires three inputs: surface temperature, basal heat flow, and in-situ thermal conductivity. The .mat files contain all of the necessary information and gridded framework to apply the code and calculate temperature at depth. A single file 'run.m' will

execute all scripts in the appropriate order and request necessary user input. A

‘README’ included in the archive provides more detailed descriptions of each of the .m and .mat files.

REFERENCES

- Allred, J. (2004), Milgro Greenhouses Newcastle, Utah, *GHC Bulletin*, 25(4), 34–39.
- AMAX Exploration Inc. (1998), Temperature-gradient data for southwestern Utah obtained by Amax during the late 1970s and early 1980s, Energy and Geoscience Institute unpublished data.
- Bahr, D. B., E. W. H. Hutton, J. P. M. Syvitski, and L. F. Pratson (2001), Exponential approximations to compacted sediment porosity profiles, *Computers & Geosciences*, 27(6), 691–700, doi:10.1016/S0098-3004(00)00140-0.
- Barker, C. (1996), *Thermal modeling of petroleum generation: theory and applications*, Elsevier.
- Bartlett, M. G., D. S. Chapman, and R. N. Harris (2004), Snow and the ground temperature record of climate change, *Journal of Geophysical Research*, 109(F4), F04008, doi:10.1029/2004JF000224.
- Bartlett, M. G., D. S. Chapman, and R. N. Harris (2005), Snow effect on North American ground temperatures, 1950–2002, *Journal of Geophysical Research*, 110(F3), F03008, doi:10.1029/2005JF000293.
- Bauer, M. S. (1985), Heat Flow at the Upper Stillwater Dam Site, Uinta Mountains, Utah, 94 pp., University of Utah.
- Bauer, M. S., and D. S. Chapman (1986), Thermal regime at the Upper Stillwater dam site, Uinta mountains, Utah: Implications for terrain, microclimate and structural corrections in heat flow studies, *Tectonophysics*, 128(1-2), 1–20, doi:10.1016/0040-1951(86)90305-7.
- Beach, R. D. W., F. W. Jones, and J. A. Majorowicz (1987), Heat flow and heat generation estimates for the Churchill Basement of the western Canadian Basin in Alberta, Canada, *Geothermics*, 16(1), 1–16, doi:10.1016/0375-6505(87)90075-7.
- Beardsmore, G. R. (1996), *The Thermal History of the Browse Basin and Its Implications for Petroleum Exploration*, Monash University.

- Beardsmore, G. R., and J. P. Cull (2001), *Crustal Heat Flow: A Guide to Measurement and Modeling*, Cambridge University Press, Cambridge.
- Blackett, R. E. (2007), *Temperature-Depth Monitoring in the Newcastle Geothermal System: Utah Geological Survey Report of Investigation 258*, Salt Lake City.
- Blackwell, D. D., and M. Richards (2004), Geothermal Map of North America,
- Blackwell, D. D., and J. L. Steele (1989), *Thermal History of Sedimentary Basins*, edited by N. D. Naeser and T. H. McCulloh, Springer New York, New York, NY.
- Bodell, J. M. (1981), Heat Flow in the North-Central Colorado Plateau, 134 pp., University of Utah.
- Bodell, J. M., and D. S. Chapman (1982), Heat flow in the north-central Colorado Plateau, *Journal of Geophysical Research*, 87(B4), 2869, doi:10.1029/JB087iB04p02869.
- Bullard, E. C. (1947), The Time Necessary for a Bore Hole to Attain Temperature Equilibrium, *Geophysical Journal International*, 5, 127–130, doi:10.1111/j.1365-246X.1947.tb00348.x.
- Cao, S., and C. Hermanrudl (1988), Formation temperature estimation by inversion of borehole measurements, *Geophysics*, 53(7), 979–988.
- Carrier, D. L. (1979), Gravity and Heat Flow Studies at Twin Peaks: An Era of Late Tertiary Silicic Volcanism in Millard County, Utah, 120 pp., University of Utah.
- Carrier, D. L., and D. S. Chapman (1981), Gravity and thermal models for the Twin Peaks Silicic Volcanic Center, southwestern Utah, *Journal of Geophysical Research*, 86(B11), 10287, doi:10.1029/JB086iB11p10287.
- Chapman, D. S. (1976), Heat flow and heat production in Zambia, 94 pp., University of Michigan.
- Chapman, D. S. (1979), *Regional Heat Flow and Geochemical Studies in Southwest Utah: Final Report*, Salt Lake City.
- Chapman, D. S., M. D. Clement, and C. W. Mase (1981), Thermal regime of the Escalante Desert, Utah, with an analysis of the Newcastle Geothermal System, *Journal of Geophysical Research*, 86(B12), 11735, doi:10.1029/JB086iB12p11735.
- Chapman, D. S., T. H. Keho, M. S. Bauer, and M. D. Picard (1984), Heat flow in the Uinta Basin determined from bottom hole temperature (BHT) data, *Geophysics*, 49(4), 453–466, doi:10.1190/1.1441680.

- Chiasson, A. (2004), Electric Power Generation in the Roosevelt Hot Springs Area - The Blundell Geothermal Power Plant, *GHC Bulletin*, 5(4), 16–20.
- Chisholm, T. J. (1990), Climate Change Inferred from Borehole Temperatures: An Example from Western Utah, 94 pp., University of Utah.
- Clement, M. D. (1981), Heat Flow and Geothermal Assessment of the Escalante Desert, Part of the Oligocene to Miocene Volcanic Belt in Southwestern Utah, 118 pp., University of Utah.
- Clement, M. D., and D. S. Chapman (1981), *Heat Flow and Geothermal Assessment of the Escalante Desert, Southwestern Utah, With Emphasis on the Newcastle KGRA*.
- Deming, D., and D. S. Chapman (1988), Inversion of bottom-hole temperature data: The Pineview field, Utah-Wyoming thrust belt, *Geophysics*, 53(5), 707, doi:10.1190/1.1442504.
- Drury, M. J. (1986), *Thermal conductivity, thermal diffusivity, density and porosity of crystalline rocks*, Ottawa.
- Funnell, R., D. Chapman, R. Allis, and P. Armstrong (1996), Thermal state of the Taranaki Basin, New Zealand, *Journal of Geophysical Research*, 101(B11), 25197–25215, doi:10.1029/96JB01341.
- Goutorbe, B., F. Lucazeau, and A. Bonneville (2007), Comparison of several BHT correction methods: a case study on an Australian data set, *Geophysical Journal International*, 170(2), 913–922, doi:10.1111/j.1365-246X.2007.03403.x.
- Gwynn, M., B. Blackett, R. Allis, and C. Hardwick (2013), New Geothermal Resource Delineated Beneath Black Rock Desert, Utah, in *Thirty-Eighth Workshop on Geothermal Reservoir Engineering*, pp. 1511–1519, Stanford, California.
- Harrison, W. E., and K. V. Luza (1983), *Geothermal Resource Assessment of Oklahoma*, Norman, Oklahoma.
- Heilweil, V., and L. Brooks (2011), Conceptual model of the Great Basin carbonate and alluvial aquifer system, *U.S. Geological Survey Scientific Investigations Report 2010-5193*, 191.
- Henrickson, A. (2000), New Heat Flow Determinations from Oil and Gas wells in the Colorado Plateau and Basin and Range of Utah, 70 pp., University of Utah.
- Hintze, L., and F. Davis (2003), *Geology of Millard County, Utah*, Utah Geological Survey.

- Issler, D. R., and C. Beaumont (1986), Estimates of terrestrial heat flow in offshore eastern Canada: Discussion, *Canadian Journal of Earth Sciences*, 23(12), 2083–2085, doi:10.1139/e86-195.
- Kehle, R. O., R. J. Schoepfel, and R. K. Deford (1970), The AAPG geothermal survey of North America, *Geothermics*, 2, 358–367, doi:10.1016/0375-6505(70)90034-9.
- Keho, T. H. (1987), Heat Flow in the Uinta Basin Determined from Bottom Hole Temperature (BHT) Data, 99 pp., University of Utah.
- Majorowicz, J. A., and A. M. Jessop (1981), Regional heat flow patterns in the Western Canadian Sedimentary Basin, *Tectonophysics*, 74(3-4), 209–238, doi:10.1016/0040-1951(81)90191-8.
- Masbruch, M. D., D. S. Chapman, and D. K. Solomon (2012), Air, ground, and groundwater recharge temperatures in an alpine setting, Brighton Basin, Utah, *Water Resources Research*, 48(10), W10530, doi:10.1029/2012WR012100.
- Mase, C. W. (1979), Geophysical study of the Monroe-Red Hill geothermal system, 108 pp., University of Utah.
- Moran, K. J. (1991), Shallow Thermal Regime at the Jordanelle Dam Site, Central Rocky Mountains, Utah, 141 pp., University of Utah.
- Powell, W. G. (1997), Thermal State of the Lithosphere in the Colorado Plateau-Basin and Range Transition Zone, Utah, 232 pp., University of Utah.
- Powell, W. G., D. S. Chapman, N. Balling, and A. Beck (1988), Continental Heat-Flow Density, in *Handbook of Terrestrial Heat-Flow Density Determination*, edited by R. Haenel, L. Rybach, and L. Stegena, p. 504, Kluwer Academic Publishers, Norwell, Ma.
- Pribnow, D. F. C., and J. H. Sass (1995), Determination of thermal conductivity for deep boreholes, *Journal of Geophysical Research*, 100(B6), 9981, doi:10.1029/95JB00960.
- Project Management Institute (2013), *A Guide to the Project Management Body of Knowledge: PMBOK(R) Guide*, 5th ed., Project Management Institute.
- Ražnjević, K. (1995), *Handbook of Thermodynamic Tables*, Begell House. [online]
- Reiter, M., and A. M. Jessop (1985), Estimates of terrestrial heat flow in offshore eastern Canada, *Canadian Journal of Earth Sciences*, 22(10), 1503–1517, doi:10.1139/e85-156.

- Reiter, M., and R. J. C. Tovar (1982), Estimates of terrestrial heat flow in northern Chihuahua, Mexico, based upon petroleum bottom-hole temperatures, *Geological Society of America Bulletin*, 93(7), 613, doi:10.1130/0016-7606(1982)93<613:EOTHFI>2.0.CO;2.
- Roy, R. F., A. E. Beck, and Y. S. Touloukian (1981), Thermophysical properties of rocks, in *Physical Properties of Rocks and Minerals*, edited by Y. S. Touloukian, W. R. Judd, and R. F. Roy, pp. 409–502, McGraw-Hill, New York.
- Sass, J. H., A. H. Lachenbruch, R. J. Munroe, G. W. Greene, and T. H. Moses (1971), Heat flow in the western United States, *Journal of Geophysical Research*, 76(26), 6376–6413, doi:10.1029/JB076i026p06376.
- Smith, W. H. F., and P. Wessel (1990), Griding with continuous curvature splines in tension, *Geophysics*, 55(3), 293–305, doi:10.1190/1.1442837.
- Taylor, A., A. Judge, and V. Allen (1986), Terrestrial heat flow from project CESAR, Alpha Ridge, Arctic Ocean, *Journal of Geodynamics*, 6(1-4), 137–176, doi:10.1016/0264-3707(86)90037-2.
- Tester, W. J. et al. (2006), *The Future of Geothermal Energy The Future of Geothermal Energy - Impact of Enhanced Geothermal Systems (EGS) on the United States in the 21st Century*.
- Touloukian, Y. S., R. W. Powell, and C. Y. Ho (1970), *Thermophysical Properties of Matter, vol. 2, Thermal Conductivity, Non-Metallic Solids*, IFI/Plenum, Washington and New York.
- Western Regional Climate Center, [online] Available from: <http://www.wrcc.dri.edu> (Accessed 1 December 2011)
- Willett, S. D. (1988), Spatial Variation of Temperature and Thermal History of the Uinta Basin, 121 pp., University of Utah.
- Wilson, W. R. (1980), Thermal Studies in a Geothermal Area, 145 pp., University of Utah.
- Zhdanov, M. S. (2002), *Geophysical Inverse Theory and Regularization Problems*, 1st ed., Elsevier.